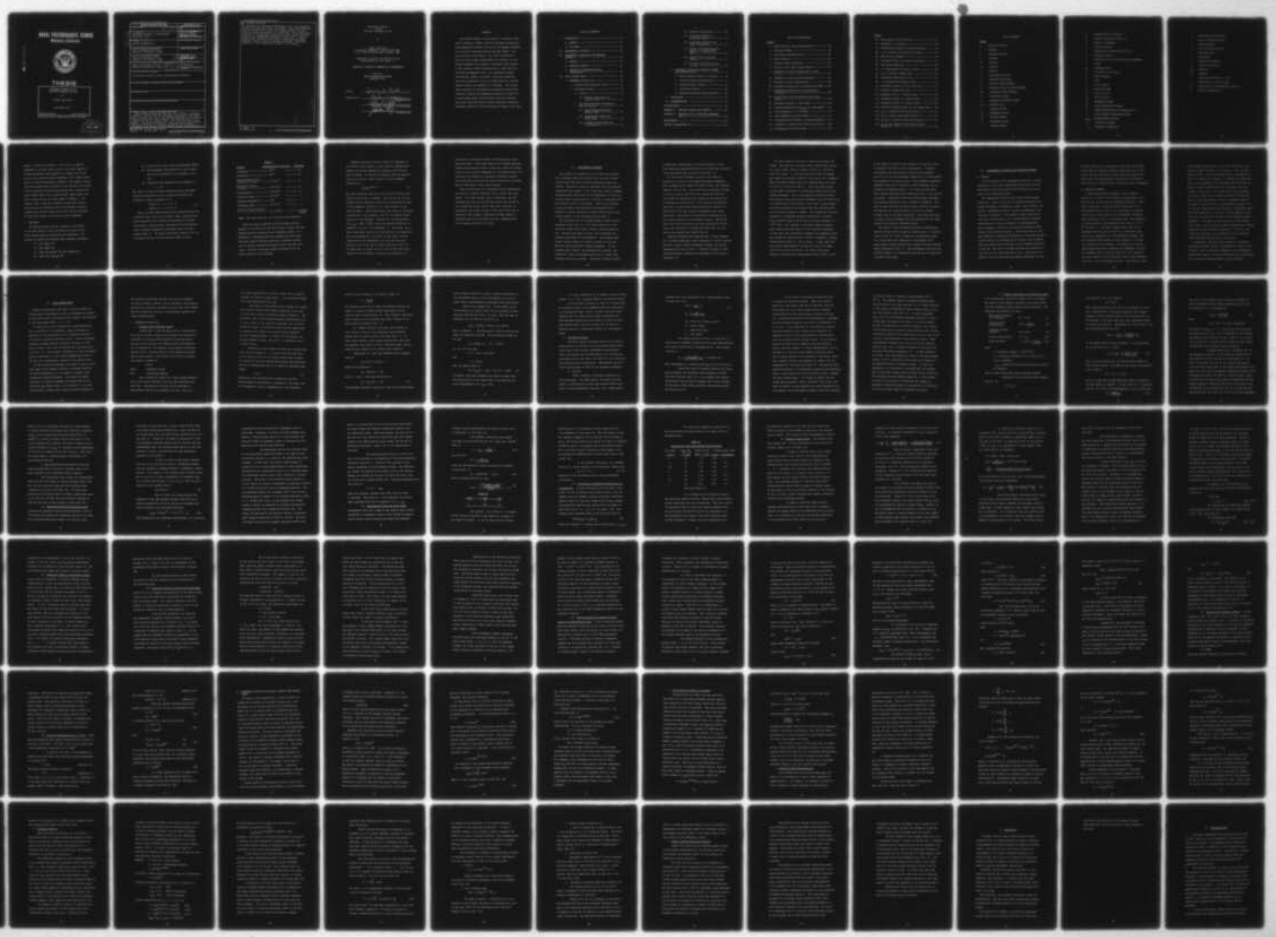
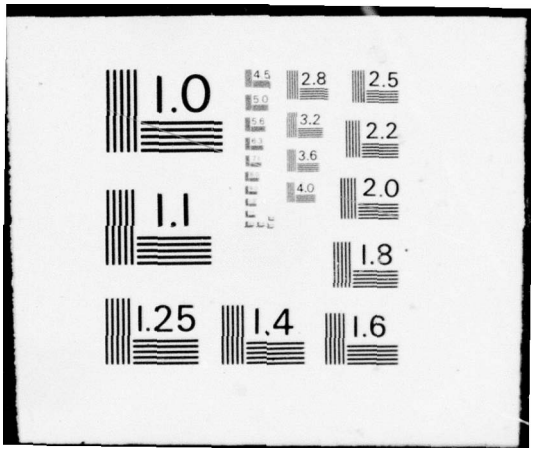
AD-A032 301 NAVAL POSTGRADUATE SCHOOL MONTEREY CALIF F/G 20/5
GASDYNAMIC EFFECTS ON AN ELECTRIC DISCHARGE IN AIR.(U)
SEP 76 J L BARTO

UNCLASSIFIED NL

1 OF 2
ADA032301




1.0
1.1
1.25
1.4
1.6
1.8
2.0
2.2
2.5
2.8
3.2
3.6
4.0
4.5
5.0

AD A032301

NAVAL POSTGRADUATE SCHOOL
Monterey, California



THESIS

GASDYNAMIC EFFECTS ON AN
ELECTRIC DISCHARGE IN AIR

by

Jonney Lynn Barto

September 1976

Thesis Advisor: Oscar Biblarz

Approved for public release; distribution unlimited.

DDC
RECEIVED
NOV 22 1976
A

SECURITY CLASSIFICATION OF THIS PAGE (When Data Entered)

REPORT DOCUMENTATION PAGE		READ INSTRUCTIONS BEFORE COMPLETING FORM
1. REPORT NUMBER	2. GOVT ACCESSION NO.	3. RECIPIENT'S CATALOG NUMBER (9)
4. TITLE (and Subtitle) (6) Gasdynamic Effects on an Electric Discharge in Air.		5. TYPE OF REPORT & PERIOD COVERED Master's Thesis; September 1976
		6. PERFORMING ORG. REPORT NUMBER
7. AUTHOR(s) (10) Jonney Lynn Barto		8. CONTRACT OR GRANT NUMBER(s)
9. PERFORMING ORGANIZATION NAME AND ADDRESS Naval Postgraduate School Monterey, California 93940		10. PROGRAM ELEMENT, PROJECT, TASK AREA & WORK UNIT NUMBERS
11. CONTROLLING OFFICE NAME AND ADDRESS Naval Postgraduate School Monterey, California 93940 (11)		12. REPORT DATE September 1976
		13. NUMBER OF PAGES 146
14. MONITORING AGENCY NAME & ADDRESS (if different from Controlling Office) Naval Postgraduate School Monterey, California 93940 (12) 145 p.		15. SECURITY CLASS. (of this report) Unclassified
		15a. DECLASSIFICATION/DOWNGRADING SCHEDULE

16. DISTRIBUTION STATEMENT (of this Report)

Approved for public release; distribution unlimited.

17. DISTRIBUTION STATEMENT (of the abstract entered in Block 20, if different from Report)

18. SUPPLEMENTARY NOTES

19. KEY WORDS (Continue on reverse side if necessary and identify by block number)

20. ABSTRACT (Continue on reverse side if necessary and identify by block number)

The overall purpose of this work is to develop a subsonic, turbulent, diffuse electric discharge operating at near atmospheric pressure for use as the pumping mechanism in an Electric Discharge Convection Laser (EDCL). The work was done in two phases. The first consisted of a data collection phase during which the variation of discharge parameters was studied to determine their effects on the current-voltage characteristics

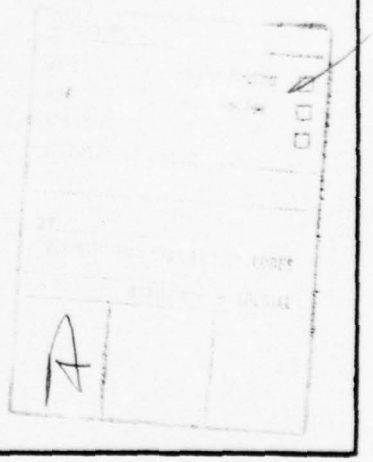
DD FORM 1 JAN 73 1473 (Page 1) EDITION OF 1 NOV 65 IS OBSOLETE S/N 0102-014-6601

SECURITY CLASSIFICATION OF THIS PAGE (When Data Entered)

251450

20. Abstract (Cont'd)

of the multi-pin electrode arrangements used. The parameters studied included gap length, flow speed, turbulence intensity, electrode orientation, rate of voltage increase, and gas density through the addition of a diffuser. The second phase consisted of developing an interactive model which correctly reflects the dependences observed in phase one. A space-charge model resulted which correctly explains most major observed trends in gross discharge properties. Discharge stability is also discussed in terms of the model.



Gasdynamic Effects
on an
Electric Discharge in Air

by

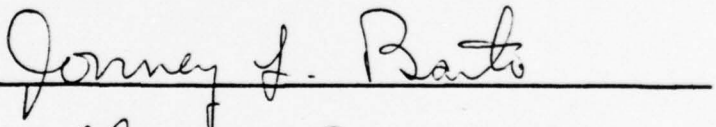
Jonney Lynn Barto
Lieutenant Commander, United States Navy
B. S., United States Naval Academy, 1965

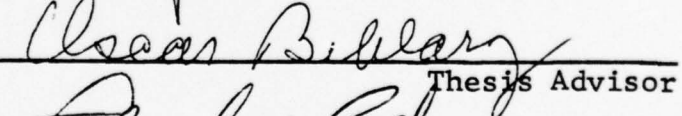
Submitted in partial fulfillment of the
requirements for the degree of

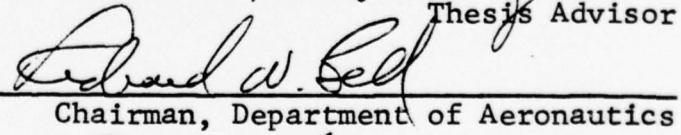
MASTER OF SCIENCE IN AERONAUTICAL ENGINEERING

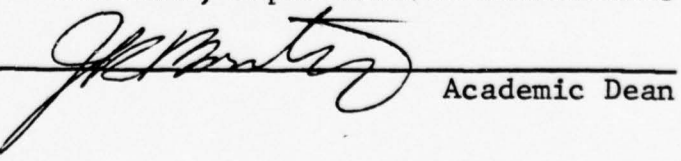
from the

NAVAL POSTGRADUATE SCHOOL
September 1976

Author 

Approved by: 
Thesis Advisor


Chairman, Department of Aeronautics


Academic Dean

ABSTRACT

The overall purpose of this work is to develop a subsonic, turbulent, diffuse electric discharge operating at near atmospheric pressure for use as the pumping mechanism in an Electric Discharge Convection Laser (EDCL). The work was done in two phases. The first consisted of a data collection phase during which the variation of discharge parameters was studied to determine their effects on the current-voltage characteristics of the multi-pin electrode arrangements used. The parameters studied included gap length, flow speed, turbulence intensity, electrode orientation, rate of voltage increase, and gas density through the addition of a diffuser. The second phase consisted of developing an interactive model which correctly reflects the dependences observed in phase one. A space-charge model resulted which correctly explains most major observed trends in gross discharge properties. Discharge stability is also discussed in terms of the model.

TABLE OF CONTENTS

I. INTRODUCTION ---------- 12

A. GENERAL ---------- 12

B. THE MODEL ---------- 14

II. EXPERIMENTAL APPARATUS ---------- 19

III. EXPERIMENTAL OBJECTIVES AND MODELING APPROACH ---------- 23

A. GENERAL ---------- 23

B. MODELING APPROACH ---------- 24

C. PREVIEW OF EXPERIMENTAL/MODEL CORRELATIONS ---------- 26

IV. SPACE CHARGE MODEL ---------- 28

A. BREAKDOWN VOLTAGE (V_b) ---------- 29

1. Uniform Field (parallel plate) -------- 29

2. Non-Uniform Fields ---------- 33

a. No-Flow ---------- 33

(1) Spatial Development of Virtual Anode ---------- 37

b. Gas Convection/Flow Orientation Effects Analysis ---------- 41

(1) Space-Charge-Convection-Effects Model ---------- 42

(2) Experimental Inputs and Basic Model ---------- 45

(3) Maximum Voltage Ratio Due to Convection ---------- 47

(4) Minimum Voltage Ratio -------- 49

(5) Turbulence Effects on Breakdown Voltage ---------- 56

(6) Cross-Flow Stability and Field Interactions ---------- 57

(7) Effects of Charged Particle Density on Recombination Times ---------- 60

(8) Reverse Flow Convection Effects ---------- 67

(9) Analytic Considerations in I = f(U) ---------- 70

B. GASDYNAMIC EFFECTS ON DISCHARGE CURRENT (NON-UNIFORM FIELDS) ---------- 72

1. Pure Convection Effects on Current ---- 76

2. Current-Voltage Characteristics ------- 77

3. Diffuser/Density Effects ---------- 82

4. Turbulence Effects ---------- 84

5. Maximum Current/Discharge Stability --- 90

V. CONCLUSIONS ---------- 93

VI. RECOMMENDATIONS ---------- 95

ILLUSTRATIONS ---------- 98

APPENDIX A VARIABLE VOLTAGE RATE RESULTS ---------- 129

APPENDIX B EMPIRICAL FIT TO PUBLISHED BREAKDOWN DATA ---------- 132

BIBLIOGRAPHY ---------- 143

INITIAL DISTRIBUTION LIST ---------- 145

LIST OF ILLUSTRATIONS

Figure

1. Sample Electric Field Distributions ---------- 98

2. Electrode Design ---------- 99

3. Turbulence Generating Grids ---------- 100

4. Power Supplies ---------- 101

5. Variable Speed Transmission ---------- 102

6. Parallel Plate Space Charge Effects ---------- 103

7. Comparison of Space Charge Model to Data for E_b ---------- 104

8. Breakdown Voltage Density Dependence ---------- 105

9. Schematic of Flow Orientations ---------- 106

10. Breakdown Voltage Data in Ordinary Flow Mode -- 107

11. Breakdown Voltage Data in Reverse/Cross-Flow Modes ---------- 108

12. Point-Plane Field Distribution with Space Charge ---------- 109

13. Breakdown Voltage vs. Gap Length ---------- 110

14. Predicted/Observed $V_b/V_{bo})_{max}$ vs. Gap Length -- 111

15. Slip Parameter at E = 20 kV/cm ---------- 112

16. Slip Parameter at Anode Surface, E = E_p ------- 113

17. Development and "Blowout" of Anode Extension -- 114

18. Schematic of Observed Pin Tip Glow Patterns --- 115

19. Photographs of the Discharge ---------- 116

Figure

20. Photographs of the Discharge ---------- 117

21. Schematic of Cross-Flow ---------- 118

22. Recombination Lengths in Cross-Flow Mode ------ 119

23. V_b vs. Velocity as Predicted by Model --------- 120

24. Reverse Flow Schematic ---------- 121

25. Avalanche Travel for Various Conditions ------- 122

26. The Current Equation ---------- 123

27. I-V Characteristic Velocity Shift ---------- 124

28. V_b vs. Velocity Summary Plot ---------- 125

29. Ionization Efficiency of Air ---------- 126

30. I-V Characteristic Density Shift ---------- 127

31. Breakdown Current vs. Mass Flow Rate ---------- 128

A-1 Variable Voltage Rate Data ---------- 131

B-1 Breakdown Power vs. Density Ratio ---------- 135

B-2 Breakdown Voltage vs. Density Ratio ---------- 136

B-3 Breakdown Current vs. Density Ratio ---------- 137

B-4 Multi-Pin Specific Power vs. Gap Length Data -- 138

B-5 V_b vs. Velocity Data with Screen # 9 ---------- 139

B-6 I_b vs. Velocity Data with Screen # 9 ---------- 140

B-7 P_b/cm vs. Velocity Curves with Screen # 9 ----- 141

B-8 I_b vs. Gap Length at Various Velocities/ Screen # 9 ---------- 142

LIST OF SYMBOLS

Symbol	
A	Stoletow Constant
a	Constant
B	Stoletow Constant
C	Constant
C1	Constant
C2	Constant
c	Constant
d	Gap Length (actual)
d'	Effective Gap Length
E	Electric Field Strength
E'	Effective Electric Field Strength
E_i'	Ionization Field Strength
e	Electronic Charge
f	Frequency of Current Pulses
f( )	Function of ( )
I	Current (total)
I_b	Breakdown Current
I_o	No-Flow Current
i	Avalanche Current
j	Current Density

k	Charged Particle Mobility
M	Corona Initiation Voltage = V_c
N	Number of Avalanches
n	Particle Density
o	Subscript for No-Flow or STP Value
P	Pressure (total)
p	Amplitude of Fluctuating Pressure Component
P	Power
P_b	Breakdown Power
R	Tip Radius of Pin Anode
S	Slip Parameter
t	Time
U	Flow Velocity
V	Applied Voltage
$\bar{v}$	Total Velocity
$\bar{v}_d$	Drift Velocity
V_b	Breakdown Voltage
V_c	Corona Initiation Voltage
X	Anode Extension due to Convection ($U\tau$)
x	Axial Distance from Anode Surface
x_{rec}	Recombination Distance
x_i	Ionization Distance
α_i	Ionization Coefficient

α_r	Recombination Coefficient
γ	Rate of Voltage Increase
δ	Anode Extension
δ_o	No-Flow Anode Extension
λ	Mean Free Path
ρ	Gas Density
ρ_o	Standard Gas Density
ω	Turbulent Frequency
$\sum$	Summation
$\int$	Integral
η	Ionization Efficiency ($\alpha i/E$)
τ	Characteristic Time Interval
$\triangleq$	Proportional to/Approximately Equal to
$\overset{o}{=}$	Order of Magnitude of

I. INTRODUCTION

A. GENERAL

This work is the continuation of an ongoing project at the Naval Postgraduate School (NPS) where the feasibility of constructing a high-energy, high pressure, continuous-wave Electric Discharge Convection Laser (EDCL) is being investigated.

Laser systems of this type currently under investigation are limited in power output by the amount of electrical power which can be coupled into the laser (Ref. 1). Since laser gain is directly proportional to the population inversion created by electrical pumping, the importance of optimum conditions in the discharge region can readily be seen.

Previous work on this project at NPS vividly demonstrated the importance of flow conditioning on discharge performance. Power increases in excess of 250 times the normal no-flow conditions were demonstrated by flowing air rapidly through the discharge region with proper conditioning by turbulence generating screens (Ref. 2).

A brief general look at the physical situation prevailing in the discharge section will be presented here

to review the state of the art and to aid in interpretation of observed electrical characteristics. The basic geometric design of the electrodes is a common one often used in electric discharge work, the positive point-to-plane. This design results in an electric field distribution in the absence of space charge which is proportional to 1/x, where x is the distance from the point. This inverse field dependence is common to many non-uniform field electrode geometries including the hyperboloidal point-to-plane, concentric cylinders, wire-to-plane, sphere-to-plane, and many others, so the analysis presented here can be applied to a number of technically interesting cases.

The field inverse dependence on distance from an electrode results in the division of the electrode gap into distinct regions of very high field where x is small, and very low field when x is relatively large. The smaller the radius of the electrode involved, the more pronounced the division. Figure (1) illustrates this effect for two geometries.

As a result of the above, as voltage is increased across the gap, ionization will begin in the high field region, confining the discharge activity to the immediate vicinity of the pin where free electrons are able to gain enough

energy to ionize by collision. Just prior to complete breakdown of the gap, there exists a very small region of intense ionization which appears as a bright glow at the pin tip (in a point-to-plane discharge), and a space charge region of larger proportions, caused by less intense ionization and electrostatic repulsion of the positive ions formed in the ionization region by the positive pin. Beyond this space charge region lies a quasi-neutral region which consists of most of the low field region of Figure 1. The cathode, while lying well outside the high field region, does not play an important role in the dynamic processes taking place near the anode, and so will not be discussed in this work, except in its role at final breakdown.

B. THE MODEL

The analysis which follows is based on the ability of the flow field to alter the shape and extent of the space charge region by convection and turbulence. The problem is complex and involves many variables including:

(1) tip radius (R)

(2) gap length (d)

(3) mean gas density ($\bar{\rho}$) and composition

(4) mean flow velocity ($\bar{U}$)

(5) electric/flow field coupling mechanisms ($\bar{E}$,$\bar{U}$,k)

(6) time dependent fluctuations of 3 and 4 above due to the introduction of turbulence, U(t), ρ(t)

(7) ionization and charged particle dynamics (α , α , λ , e, n)

The result is that the easily measurable gross discharge electrical properties such as voltage and current are functions of these variables, i.e.;

$$I=f_1(R,\ d,\rho\ ,\ U,\ E,\ k,\ t)$$
$$V=f_2(R,\ d,\rho\ ,\ U,\ E,\ k,\ t) \qquad (1)$$

There are many characteristic times associated with the variables cited, such as gas transit times, characteristic times associated with turbulent fluctuations of density and velocity, characteristic ionization and recombination times, streamer propagation and growth times, and many others (Table I). The times cited above, however, will be of primary interest in the discussion which follows.

TABLE I

Process	Characteristic Time (Sec)	Reference
Ionization	10^{-12}	10
Excitation	10^{-12}	10
Energy Transfer from Electrons to Atoms	10^{-5}-10^{-6}	10
Maxwellian Distrib. of Atoms	10^{-8}-10^{-10}	10
Recombination	10^{-5}-10^{-6}	13
Current Pulsing	10^{-4}-10^{-5}	4
Streamer Propagation	10^{-8}	4
Turbulence Freq	10^{-1}-10^{-5}	3
Rate of Voltage Increase (V/γ)	0-2.5(10^{-4})	(present work)

(NOTE: The times from Ref. 10 are for an arc discharge.)

Since the model presented in the following sections depends on the ability of the flow field to couple with the charged particles produced in the discharge region, it is important to understand how this coupling may take place. The three types of charged particles of primary interest are, of course, positive and negative ions, and free electrons. The bulk of the gas remains un-ionized over the major portion of the discharge.

Charged particles in the gas under the influence of an electric field acquire a drift velocity ($\bar{V}_d = k\bar{E}$) which depends on the gas composition, pressure, and electric field strength. If the gas is flowing, then the particle velocity (in vector form) relative to the stationary electrodes is:

$$\bar{v}_{total} = k\bar{E} + \bar{U} \qquad (2)$$

The sign convention used here will be that $\bar{E}$, $\bar{U}$ and x are positive from anode to cathode. The k in Eq. (2) is the charged particle mobility, which can be expressed in terms of the parameters listed as $k \doteq e\,\lambda/m\bar{v}$, where m is the particle mass, λ (the particle mean free path) is inversely proportional to gas pressure, and $\bar{v}$ is the random thermal velocity of the particle. Equation (2) can be rewritten as $\bar{v}_{total} = k\bar{E}(1 + \bar{U}/k\bar{E})$, where the quantity $\bar{U}/k\bar{E}$ will be referred to as the "slip parameter, S." Electrons, due to their small mass, have a very high mobility, and generally, the slip parameter for electrons is very small, and gas convection is not significant; but ions are much more massive, so k is low and ion drift velocities can be of the same order of magnitude as $\bar{U}$, even in the high field regions of the discharge, resulting in significant ion

relocation by convection within the characteristic times mentioned above. Since high densities of charged particles produce electrostatic fields of their own, which can easily reach the same order of magnitude as the applied field, the electrons are affected by convection indirectly through the alteration of the electric field structure by the movement of high density ionic space charges.

Visual observations of a discharge vividly demonstrate the ability of highly turbulent flow to affect the space charge. With high velocity and no turbulence, the glow extending from the tips of the pins toward the cathode is very bright and steady, while, when high turbulence is introduced, the bright portion of the glow can be seen to radically "whip" around, indicating the high degree of influence that the fluctuating velocity components have on the charges present in the flow.

II. EXPERIMENTAL APPARATUS

The primary test apparatus used in this work consists of a plexiglass wind tunnel with a test section in which various electrodes and turbulence generating grids were mounted. Electrode spacing is adjustable and the electrode orientation with respect to the flow field could be changed, permitting much flexibility in the examination of flow and electric field interactions for a variety of conditions and with several levels of turbulence. Later in the testing, a new wind tunnel was added which was equipped with a diffuser to permit operation at higher flow velocities and reduced density in the discharge section (Ref. 3).

The electrodes are of a design common to many electric-discharge lasers (Fig. 2). The anode consists of a pin rack with three rows of pins, eleven to thirteen pins per row. The pins were made of steel, with horizontal and vertical separation of one centimeter. The cathodes used varied, because there was a need to search for the most effective and structurally sound arrangement. All the cathodes used, however, were geometrically similar, and simulated a plane with minimum solid area to reduce flow blockage as much as possible. Structural integrity became

an important consideration as testing progressed, since flow velocities exceeded 180 meters per second and turbulence levels introduced were relatively high (Ref. 3).

All tests were performed in an air flow which was supplied by a Carrier three-stage Centrifugal Compressor with a maximum inlet capacity of 4000 ft^3/min, and a maximum pressure ratio of two. Flow velocity was regulated through a series of valves, and flow total temperature was kept below 100^oF by passing the air through an air cooler prior to reaching the test section. Flow velocity was measured with pitot or pitot-static tubes which were mounted in or downstream of the test section, depending on the tunnel being used. Turbulence was introduced by mounting one or more grids upstream of the discharge section. Some grids which were used in previous work were retested for verification and validation of systems operation (Ref. 3), and several new designs were tested (Fig. 3).

Turbulence spectra were measured with a Thermo Systems, Inc. hot-wire anemometer, which consisted of a 1051-2 monitor and power supply, 1054A-30 anemometer module, and locally manufactured hot-wire probes. A detailed account of turbulence measurement equipment and techniques can be found in Reference (3).

Two power supplies were used to power the electric discharge. The first was a Sorensen Model 1030-20 High Voltage D.C. power supply, which is rated at 30 kV D.C. and 20 ma with a 2% ripple. It was soon discovered that the maximum gap length was severely limited by this supply, so a Sorensen BETA Model High Voltage Supply was obtained which was rated at 60 kV D.C. and 50 ma (Fig. 4). With this power supply it was hoped to increase the maximum gap length which could undergo breakdown. Due to uncorrectible internal problems, the maximum voltage and current obtainable was 34 kV and 19 ma, so reliable tests were limited to less than 4 cm gap length. Both power supplies were equipped with trip controls which work on either voltage or current. The voltage was initially measured by a Sensitive Research electrostatic voltmeter with a maximum range of 40 kV and an internal impedance of 5.10^{15} ohms. The readings of the power supply voltmeters were compared and were found to be in excellent agreement, so they were used exclusively throughout the remaining tests. The current was measured with a variety of ammeters, ranging from microamp scales to a 200 ma scale. A meter panel was set up with three ammeters in parallel, one 0-1 ma range, one 0-50 ma, and one 0-200 ma. The meters were wired through a multi-position "Make-before-break" switch so that

as the range of one meter was exceeded, the next one could be switched in without circuit interruption. A Simpson volt-ammeter was also wired in series with the ammeter panel for use in the microampere range and as a check against the readings of the panel meters. This redundancy permitted immediate detection of erroneous current readings, and replacement of defective meters. All wiring was done with high voltage leads which were fabricated prior to the initial test phase. Connections were made through highly polished brass spheres which were about 1½ inches in diameter. The high voltage side from the power supply outlet to the anode was immersed in a high dielectric oil bath to prevent voltage leaks at the ball connection. Great care was taken to ensure that all equipment was well grounded at all times, through the laboratory grounding system.

One series of tests performed required increasing the applied voltage across the gap at various rates. A constant-speed 24 volt D.C. motor, powered by an adjustable output D.C. Power Supply was connected to the Sorensen 30 kV power supply voltage control shaft through a Metron Variable-Speed transmission (Fig. 5). This arrangement permitted the applied voltage to be increased across the gap at rates from 0-20,000 volts/second.

III. EXPERIMENTAL OBJECTIVES AND MODELING APPROACH

A. GENERAL

A brief preview of the experimental work and an overall perspective of the model development should serve to help keep sight of the "big picture" while sorting out the details of the individual pieces.

The experimental work has been divided into two main categories. First, tests were run varying individual discharge parameters, including gap length, flow velocity, gas density, turbulence intensity, cathode configuration, and electrode orientation. The purpose of these tests was to establish a data base for use in analyzing the individual contributions of various parameters to discharge power, and to attempt to formulate an interactive physical model based on the observed relations. The second phase of testing consisted of observing the effects of increasing applied voltage across the discharge gap at various rates to determine what effect this would have on the breakdown properties of the gap. The rate of voltage increase was constant for each run, but it varied from run to run. These tests also added to the data base which was being established, but the

specific purpose was to determine if any type of resonance effect might be detected between a particular rate of increase, and the turbulence spectra which were being introduced since the characteristic time scales of turbulence and the rates of increase were of the same order of magnitude.

B. MODELING APPROACH

A space-charge model development, which begins in Section IV, is based on the dynamic processes which occur when the gap is very near its breakdown potential. Under these conditions, a positive point-to-plane gap in an electronegative gas such as air, experiences a pulsating current due to the formation of pre-breakdown streamers whose magnitudes vary in a statistical way. The frequency of these pulses has been measured on the order of 10^4 to 10^5 Hz (Ref. 4). The model proposed here looks at the discharge from the point of view of an individual event, such as the propagation of a pre-breakdown streamer, and the situation that prevails in the discharge at the time and location of its occurence. For example, in a steady, non-flowing point-plane discharge near breakdown potential, the streamers which cyclically form, all "see" generally the same "picture" (field structure, space charge distribution, etc.) as the preceding ones did. Much activity takes

place between these events, but at each period the situation at a given location is very similar. Now, if something is done to alter the picture that the streamers see, such as a reduction of density, or flowing gas through the gap, or the introduction of turbulence, the "picture" presented to each streamer may be very different from the steady, no-flow case. The change in the local situation can be the result of two separate classes of influencing factors, one steady-state, such as a permanent change in gas density; and the other, a time-dependent change, such as with the introduction of convection or turbulence, where the total change seen by the next streamer depends on how much time the effect has to work on the discharge between streamers. The change in this picture over the original case, then, is what the model assumes determines the changes observed in gross discharge properties. Of course, both classes of influence can be operative at once, and then their individual effects must be sorted out.

To summarize, the model was developed by isolating a particular influence factor, determining its effect on the "picture" seen by successive streamers, then attempting to combine the results of all such influences in an interactive way to explain observed changes in gross discharge

characteristics. The ultimate goal of this study is to develop a method of approach for optimizing the discharge for use as a pumping mechanism for the EDCL.

C. PREVIEW OF EXPERIMENTAL/MODEL CORRELATIONS

The first part of Section IV introduces the basic space-charge model and illustrates how a reduction in density by addition of a diffuser (Ref. 3) alters the picture presented to succeeding streamers. Successful development of a simple relation for the density dependence of gap breakdown voltage in a non-uniform field evolves from fitting existing data to an equation form resulting from the space-charge model. This lends credibility to the basic concept.

The next part shows an analysis of the influence of convection on the discharge with various orientations of electric and flow fields. With the aid of the space-charge model again, the change in "picture" seen by successive streamers is determined, and various maxima and minima for breakdown voltages are calculated for variations of velocity and orientation. Again the results obtained agree with experimentally observed values, lending further credibility to the proposed model concept. Various instabilities and observed visual characteristics are also discussed in terms

of the model, with general qualitative agreement between model predictions and observations.

In the second half of the development, velocity, density, and turbulence effects on discharge current and the interrelation between the current and voltage are discussed. A current equation evolves from the space-charge model which properly accounts for most major observed trends in discharge current due to convection, turbulence, and density reduction in various flow orientations. Some stability conditions are mentioned which are particularly relevant to the discussion, but no attempt is made to give a detailed account of stability effects.

The four basic discharge conditions used for comparison of the space-charge model predictions are the following:

(1) No diffuser, no turbulence

(2) No diffuser, with turbulence

(3) Diffuser on, no turbulence

(4) Diffuser on, with turbulence

Test results appear to bear out the predicted trends for each of the above cases. Detailed design data on the discharge apparatus, including diffuser and turbulence generators are given in Reference (3).

IV. SPACE CHARGE MODEL

Numerous studies have been done on various aspects of flowing gaseous discharges in order to determine the effects of convection and/or turbulence on the strength and stability of such discharges (Refs. 2, 3, 5, 6).

As pointed out in the Introduction, understanding the basic processes in a non-uniform, flowing discharge is essential to the improvement of the ultimate potential of the Electric Discharge Convection Laser. Present discharge stability problems restrict practical operation of this type of laser to the realm of 100-200 torr operating pressure (Ref. 5). This pressure limitation, or more accurately, density limitation, in turn limits maximum power input to the gas, and, consequently, restricts laser power output.

In the following discussion, an attempt is made to shed some light on the complex problem of discharge stability and power enhancement in a non-uniform, subsonic, near-atmospheric flowing discharge. Using some well-known principles of gaseous breakdown in uniform fields and a few basic gas dynamic ideas, it is possible to, at least qualitatively, explain many diverse observed phenomena of

the particular discharge sections used in this research. The basic concepts, however, may be extended to any geometry and any flow condition, provided of course that these differences are taken into account in interpreting observed discharge characteristics.

A. BREAKDOWN VOLTAGE (V_b)

1. Uniform Field (parallel plate)

Cobine (Ref. 7) and von Engle (Ref. 8) both analyze the effects of space charge on the current and voltage distributions in the gap between parallel plate electrodes. The case of the positive ion emitting anode from Reference (8) is suitable for the purposes of the present discussion. Consider first a uniform electric field between the plates with no space charge. The electric field will be constant from anode to cathode at:

$$E=V/d$$

where V=applied voltage

and d=electrode spacing.

Now, consider the effect of a space charge modification of the field structure, with the anode emitting positive ions. Assuming that the bulk of the discharge is electrically neutral as is normally the case, there will

be a small region near the anode in which the ion density exceeds the neutral charge density. A net positive charge will then characterize this area.

The effect of the positive space charge is to lower the electric field in this region, resulting in the type of field and voltage distributions shown in Figure 6. The modified E and V curves assume constant charge density out to $X=X_{sc}$, which is not physically possible, but it illustrates the point. It should be noted from the figure that an intense space charge can actually cause a positive initial voltage gradient. At point P in the figure, the voltage gradient is zero, and point P is referred to as a "virtual" anode.

Referring to the distance at which the virtual anode lies from the origin as δ, it can be seen that the value of the electric field in the neutral region must increase to account for the same voltage drop between the electrodes. One way of interpreting this is to define an equivalent gap length

$$d'=d-\delta \qquad (3)$$

Noting also that the effective voltage drop from the virtual anode to the cathode is increased by the amount ΔV, it is possible to write an expression for the effective

electric field strength in the neutral region as:

$$E' = \frac{V + \Delta V}{d'}$$

The important point here is that the apparent physical gap length is reduced by space charge modification of the electric field structure (Ref. 9). This "virtual" electrode effect applies to any electrode near which charges of the same polarity accumulate (Ref. 7).

In a normal parallel plate gap, the situation is very similar to the one just described, since positive charge tends to build up around the anode (Ref. 4). If this charge reaches a high enough concentration just prior to breakdown, the result will be a "virtual" anode, and the effective gap length d' will reflect this reduction.

Neglecting ΔV, then, the breakdown field strength would be

$$E_b \doteq V_b/d' = V_b/(d-\delta)$$

which can be written as

$$E_b = (V_b/d)/(1- \delta/d)$$

and for $\delta/d \ll 1$, this can be written as:

$$E_b \doteq (V_b/d)(1 + \delta/d) \qquad (4)$$

This equation provides a basis for a test of the space-charge

model concept which will be used to describe processes in the non-uniform field, so it is worthwhile to see if it gives results approximately in agreement with observations.

Since it was assumed that δ/d was small, E_b can be evaluated at as large a value of d as possible to minimize the contribution of the δ/d term. From the data of Reference (4), at d=20 cm, V_b=510 kV, so

$$E_b)_\infty \doteq V_b/d)_\infty \doteq 510/20 = 25.5 \text{ kV/cm}$$

Now, to estimate δ, the data point at d=10 cm can be used, where the measured V_b=265 kV. The hypothesis is that for any gap,

$$E_b = V_b/d)_\infty \ (1 + \ \delta/d \ = 265/10$$

so, for the 10 cm gap,

$$(1 + \ \delta/10) = 26.5/25.5$$

and

$$\delta \doteq .39 \text{ cm}$$

Now, the final result is:

$$E_b \doteq E_{b\infty}(1 + \delta/d) = 25.5 \ (1 + .39/d) \qquad (5)$$

In reality, the anode extension can never be larger than the physical gap, so the upper limit of E_b based on this crude approximation, is $2\ E_{b\infty} \doteq 51$kV.

It is also noted that in the absence of space charge effects (i.e. $\delta = 0$), E_b=const which is the required result.

It can be seen in Figure (7) that at 2 cm and above, the computed values of the breakdown field are quite close to the measured values; closer, in fact, than the values computed from the other models listed in Reference (4). This agreement demonstrates the possible utility of such a space-charge model, and this concept will be used in a detailed analysis of gasdynamic effects on a non-uniform field.

2. Non-Uniform Fields

The basic concept described above for the uniform field can also be applied to the non-uniform field distribution used in the present experimental investigation. First, the process will be described as in a non-flowing discharge section, and later, the effects of gas convection and turbulence will be discussed. Experimental data will then be scrutinized in light of the arguments presented.

a. No-Flow

First, consider a stationary discharge in a point-plane gap. For sharp points, the region near the point is characterized by very high electric fields just prior to spark breakdown of the gap. For a simple model,

consider the field distribution for a hyperboloidal point-to-plane (Ref. 10):

$$E(x) = \frac{R}{R+x} E_p \qquad (6)$$

$$E_p = \frac{2V}{R \log(4\ d/R)}$$

E_p = field at surface of point

R = point radius

V = applied voltage

d = gap length

For typical values of R and d of 0.05 and 3 cm respectively, breakdown voltage has been found experimentally to be about 27,400 volts in atmospheric air. This results in an E_p of:

$$E_p = \frac{2(27,400)}{0.05 \log(4 \cdot 3/.05)} \doteq 200,000 \text{ v/cm}$$

This corresponds to a reduced field (E_p/P) of 263 v/cm-torr.

Since this value of electric field is well above the atmospheric air ionization field strength of 15,000 v/cm (20 v/cm-torr) (Ref. 11), it is evident that intense ionization of the air will be taking place in the vicinity of the point by high energy electrons accelerating toward the positive point.

As an electron accelerates toward the point, it creates an electron avalanche. Since the electron mobility is much higher than the ion mobility, the electrons speed into the positive point and get absorbed leaving behind the ion space charge in front of the pin tip. Detailed descriptions of the development of streamers and the electron avalanche can be found in References (7, 8, 10, 12). It is sufficient for the present to realize that dense positive space charge can be formed in the immediate vicinity of the anode which can significantly alter the electric field structure there. (In an electronegative gas such as air, negative ions would also be formed, and their number, to a first approximation, can be regarded as a fraction of the number of positive ions.) The net charge density in the vicinity of the anode, therefore, remains positive, and negative ion effects will be disregarded for the time being (Ref. 9). The positive ions, under the influence of electrostatic repulsion and diffusion, begin to move slowly away from the positive point, creating the space charge region. As voltage is raised, the discharge passes through a stable, pulseless "glow" mode, and then, as applied voltage approaches the gap breakdown value, the formation of pre-breakdown streamers causes the frequency

of current pulses to increase to approximately 10^4 to 10^5 Hz. The maximum length of streamers measured under pulsed conditions has been observed to be a linear function of the applied voltage when no space charge exists to distort the electric field (Ref. 4). It seems reasonable, then, that the pre-breakdown streamers formed in a static, steady-state discharge would behave in a similar manner. The high concentrations of positive charge in the vicinity of the anode cause an apparent anode extension into the gap, reducing the effective gap length much as in the case of the "virtual" anode described in the previous section. These pre-breakdown streamers have only to travel the reduced, effective gap, then, to effect breakdown of the gap by the processes described in Reference (4). If this assumption is correct, then influencing the extent of the space-charge region by flow or turbulence should show up as changes in the measured values of breakdown voltage. To test this assumption, it is necessary to estimate what the original size of the space charge region is under no-flow conditions. The following sections address themselves to this problem, and then to the problem of determining the changes in breakdown voltage which might be expected due to alteration of the space-charge region by gasdynamic processes.

(1) Spatial Development of the Virtual Anode.

It is interesting, and will be useful later, to examine the effects of gas density variation on the anode extension and breakdown voltage under no-flow conditions. The following relationships are used:

Mean Electron Energy for Ionization: $eE \doteq eV_i$ (7)

Electric Field Distribution: $E(x) = (\frac{R}{R+x})E_p$ (8)

Breakdown Voltage Relation: $V_b \doteq ad'+b$ (9)

Virtual Anode Effect: $d' = d - \delta$ (10)

Mean Free Path: $\lambda_e = 4\sqrt{2}\,\lambda_g \doteq \frac{c}{P(torr)}$ (11)

where

e = electronic charge = 1.6×10^{-19} coul

V_i = ionization potential $\doteq$ 15.5 volts for air

a,b,c = constants

$\lambda_{e,g}$ = electron and gas molecule mean free paths

P = pressure

and all other symbols have been previously defined.

Solving for the ionization field strength from Eq. (7),

$$E_i \doteq V_i / \lambda_e$$

and using Eq. (11), this becomes

$$E_i = V_i P/c$$

Now, using this value in Eq. (8), it is possible to solve for a characteristic "ionization distance" (the maximum distance from the anode at which a free electron would, on the average, in one mean free path, gain sufficient energy to ionize by collision). Rearranging Eq. (8) with $E(x) = E_i$, and recalling E_p from Eq. (6):

$$(R+x_i) = \frac{R}{E_i} E_p = \frac{R\ E_p(v)}{(V_i P/c)} \doteq \frac{v}{P}$$

It is assumed that the anode extension δ is proportional to x_i, and that $R \ll \delta$, so that

$$\delta \triangleq x_i \doteq \frac{v}{P} \triangleq \frac{v}{\rho} \begin{matrix} \text{(Const temp)} \\ \text{(Ideal gas)} \end{matrix} \qquad (12)$$

Now, in direct analogy with the uniform field example of the previous section, the effective gap length is expressed by Eq. (10) as

$$d' = d-\delta \triangleq d- \frac{V}{\rho} c'$$

and it is seen that the effective gap length is reduced as the gas density is reduced. If this value of d' is inserted into Eq. (9), after some rearrangement it can be shown that

$$V_b \doteq \frac{(ad+b)\ \rho}{(\ \rho + ac')} \qquad (13)$$

The form of this equation will be shown to describe the actual breakdown voltage density dependence fairly well. For example, if it is rewritten as

$$V_b/V_{bo} = \frac{2(\rho/\rho_o)}{(\rho/\rho_o+1)} \qquad (14)$$

where

$$V_{bo} \doteq ad+b \doteq V_b \text{ at one atmosphere}$$

the values of V_b/V_{bo} vs. ρ/ρ_o agree with the observation. The constant term in Eq. (14) is dependent on the specific electrode geometry and type of gas. Table II is a collection of data for a positive point-to-plane for gap lengths and densities in the present range of interest.

In making comparisons of measured data at one atmosphere pressure, it was noted that Bandel's data from Table II for the 8 cm gap is inconsistent with the data of References (6) and (7) for a point-plane gap of 8 cm, and with trends noted in the present experimental work. Also, due to the fact that Bandel's breakdown voltage at one atmosphere was nearly the same for 4 and 8 cm gaps, there is doubt that the value of V_{bo} given is appropriate for the present analysis. Therefore, the value of V_{bo} used in the calculation of the voltage ratio for the 8 cm gap for comparison with Eq. (14) was 60 kV, which is in close agreement

with the other references cited. Bandel's second point for the 8 cm gap was also discarded for the reasons already mentioned. Figure (8) shows the results of observed values of the voltage ratio vs. the predicted values of Eq. (14). The close agreement tends to support the "virtual" anode/ space-charge effects model outlined above.

TABLE II

Density Ratio	V_b (kV)		I_b (a)			
	Meas	/ Calc	Meas	/ Calc	Gap Length	Source
.05	2.0	2.6	0	0	4	Bandel (Ref 18)
.09	4.0	5.8	65	60	4	"
.15	7.2	8.7	105	110	4	"
.24	14.2	14.7	225	180	4	"
.39	22	21	240	230	4	"
.63	33	33	240	230	4	"
.98	38	38	130	130	4	"
.05	4.0	5.4	25	20	8	"
.09	8.0	9.0	150	90	8	"
.15	15	14.3	180	166	8	"
.24	24	21.8	215	204	8	"
.39	32	31	170	185	8	"

TABLE II (Continued)

Density Ratio	V_b (kV)		I_b (a)			
	Meas	/ Calc	Meas	/ Calc	Gap Length	Source
.63	(33)	40	105	105	8	Bandel (Ref 18)
.98	(38)	41	40	36	8	"
1.0	4.8	2.2	8.5	1.7	.3	Werner (Ref 15)
1.0	5.0	5.8	5.5	4.8	.6	"
1.0	9.2	11	14	10.6	1.0	Townsend (Ref 17)
1.0	10	18	(10)	21.5	1.5	"
1.0	25	25	--	37.5	2.0	Meek & Craggs (Ref 10)
1.0	60	--	--	--	8.0	"
1.0	65	--	--	--	8.0	von Engle (Ref 7)

(See Appendix B for calculation procedures and formulae.)

(NOTE: Data in parenthesis do not seem to correlate with trends observed in other references.)

b. Gas Convection/Flow Orientation Effects Analysis

It has been observed from our work that the orientation of the flow field relative to the electric field has a marked effect on the electrical properties of the discharge. Most evident is the change of breakdown voltage observed in the various orientations tested (Fig. 9).

Figures (10, 11) illustrate the nature of these changes. It can be seen from the Figures that convection increases V_b/V_{bo} in the reverse and cross-flow modes (Fig. 11) quickly to a nearly constant value on the order of 1.25. In the ordinary mode, however, the general trend is for an initial decrease in V_b/V_{bo} to a minimum in the neighborhood of 0.9-0.95 at around 75 m/sec flow velocity. After that, the ratio begins to increase again, occasionally to a value greater than one.

A space-charge-convection-effects model has been developed which successfully explains some of the major features of the breakdown voltage behavior.

Two orientations were tested, one longitudinal mode with flow from anode to cathode (ordinary mode) (Fig. 9a), and one cross-flow mode with the discharge being transverse to the gas flow (Fig. 9c). The third mode analyzed by the present model is another longitudinal mode, as in case one, but with the flow direction reversed so that the gas flow is from cathode to anode (Fig. 9b).

(1) Space-Charge-Convection-Effects Model. Although the discharge sections used consisted of from 33-39 positive pins spaced one centimeter apart for the anode, and a grounded plane-type cathode, the electric field

structure for any given pin is nearly identical with that of a single point-plane configuration, since the pins are far enough apart that the space charge regions do not overlap (Fig. 2). Therefore, the model is discussed in terms of the dynamic processes taking place at one pin, with the understanding that the processes apply equally to the test section as a whole, provided that all pins contribute uniformly to the current.

It must be noted at this point, however, that due to the statistical nature of breakdown streamer size and intensity, breakdown becomes a probability related process. For example, if the voltage across a single point gap is set so as to give a probability of breakdown (P_{f1}) in a certain time interval (Δt) of $P_{f1}=.1$, then its probability of not breaking down is

$$P_{s1}=1-P_{f1}=.9 \tag{15}$$

Now, if there are 10 pins acting independently at the same applied voltage, each with $P_{f1}=.1$, then the probability of the 10 pin gap not breaking down would be given by the following expression:

$$P_{s10}= 1-(1P_{f1})^{10} = 1-(1-.1)^{10} = .65 \tag{16}$$

This demonstrates the increased susceptibility of a multi-pin

configuration (with statistically independent pins) to break down. Therefore, to obtain the same breakdown probability, a multi-pin gap must be at a lower voltage, and observed values of breakdown voltage in multiple pin configurations may reflect this reduction.

The expression used for the electric field in the space-charge convection model is the same as used in previous sections i.e., that for the hyperboloidal point-to-plane. In this model the positive space charge is assumed to be at a high enough density to cause significant distortion of the undisturbed field out to a distance where the undistorted positive point field strength is $\doteq$ 20,000 volts/cm. This point in the field was chosen because it is well inside the region of ionization by electron collision of $\doteq$ 15,000 volts/cm for air at atmospheric pressure. The corresponding reduced field strength (E/P) $\doteq$ 20 v/cm-torr. Referring again to Figure (1), an electron arriving at point a, E = 15,000 v/cm, would, on the average, have enough energy to ionize air molecules by collision and electron avalanching would start toward the positive tip. The result, as described in the previous section, is positive space charge accumulation in front of the pin. The position where the pin field strength approaches 20,000 v/cm,

point b, is conjectured to be in the critical region where the space charge field becomes significant compared with the undistorted field. When this happens, the rest of the gap acts as if the anode lies inside the high field region caused by the dense positive space charge, and the gap is effectively shortened. Figure (12) is an illustration of this idea.

The distance defined above is used in the rest of the analysis as the magnitude of the anode extension, previously defined as δ in the no-flow analysis of the density dependence of the breakdown voltage. The effective gap length, as proposed by the model, would be the distance between the cathode and the point at which the static electric field first reaches 20,000 v/cm. Expressed mathematically, this would be

$$d' = d - \delta_{20K}$$

where the subscript indicates the field value at which is computed. This value of δ will represent the no-flow anode extension and will be referred to as $\delta_o = \delta_{20K}$.

(2) Experimental Inputs and Basic Model.

Experimental data over a range of gap lengths under no-flow conditions at atmospheric pressure have yielded an approximately linear relation between gap length and breakdown

voltage, closely approximating the point-to-plane curves of References (8, 10) (Fig. 13).

The apparent reduction in gap length, , can again be calculated from Eq. (8), using E(x) = 20,000 v/cm, as

$$\delta_o = x_{20K} = \frac{REp}{20,000} - R \qquad (17)$$

but note that

$$Ep = \frac{2V}{R \log(4d/R)}$$

Using the experimentally derived relation for breakdown voltage (Fig. 13):

$$V_b = 7800d+4000 \quad \text{(volts)} \qquad (18)$$

With an estimated R=0.05 cm, then

$$\delta(d) = \frac{.05\left(\frac{2(7800d + 4000)}{.051\log(4d/105)}\right)}{20,000} - .05 \qquad (19)$$

TABLE III

d(cm)	δ (cm)	δ/d
2	.34	.17
4	.56	.14

The quantity δ/d in Table 3 is a measure of the relative reduction in gap length for two gaps in the range of interest. It can be seen that the relative

reduction due to the presence of space charge over the 2 cm difference is only about 3%. What this means is that the linearity suggested in the data may not be between V_b and d, the actual physical gap length, but may be a linearity between V_b and d', the apparent gap as speculated earlier. Due to the small relative reduction of gap length, it is not possible to determine from the data alone which is the actual case.

In the ensuing discussion, it is assumed that V_b is a linear function of the effective, reduced gap:

$$V_b \doteq d' = d - \delta \qquad (9, 10)$$

Adoption of this hypothesis leads to some interesting conclusions.

(3) Calculation of Maximum Voltage Ratio due to Convection. In flow orientations two and three, (Fig. 9 b&c), it can be deduced from the above theory, that the maximum value of breakdown voltage occurs when convection effects remove all the space charge from the gap, thereby increasing the effective gap spacing from its normal no-flow value of $d'_o = (d - \delta_o)$ to d, its upper limit. The maximum ratio attainable then at any velocity should be

$$(V_b/V_{bo})_{max} = \frac{d}{d - \delta_o} \qquad (20)$$

where the subscript 'o' denotes the no-flow value ($\delta_o = \delta_{20K}$).

The Table below summarizes the results of this calculation for several gaps in the range of the experimental data.

TABLE IV

REVERSE AND CROSS-FLOW MAXIMUM VOLTAGE RATIOS

Gap Length d(cm)	Anode Ext (Eq. 17) δ_o (cm)	Effective Gap $d_o' = d - \delta_o$ (cm)	Voltage Ratio (max) Theory	Experiment
1	.22	.78	1.28	--
1.4	.27	1.13	1.24	1.27
1.45	.27	1.18	1.23	1.26
2	.34	1.66	1.20	--
3	.45	2.55	1.18	1.20
3.2	.47	2.73	1.17	1.15
4	.56	3.44	1.16	1.13

(See also Figure 14)

It is evident from the Table that theory and experiment agree quite well, despite many crude approximations which went into the calculations. The close numerical agreement tends to verify the initial assumption that the point where E(x)=20,000 v/cm may be considered to be the approximate axial range of the anode extension under no-flow conditions. Perhaps even more significant than

the numerical agreement is the fact that the theory predicts a decrease in the maximum voltage ratio with increasing gap length. This trend has been experimentally verified.

(4) Minimum Voltage Ratio. The ordinary flow mode, Figure (9a), is more complicated as can be seen from the data summary plot of Figure (10).

It might be expected from a space charge convection point of view, that in this orientation the space charge would be carried toward the cathode in some characteristic time interval which would tend to increase δ. If δ increases, the effective gap length decreases, which in turn results in a decrease in V_b, since $V_b \triangleq d'$. This agrees with the initial trend of the data of Figure (10). The breakdown voltage vs. velocity curves show a minimum though, beyond which V_b begins to increase again. At short gaps, in fact, V_b has been observed to not decrease at all, but show a slight increase which remains relatively constant with increasing velocity.

In order to shed some light on these apparent inconsistencies at short gaps, and to attempt to explain the complex nature of the breakdown in this orientation, it is necessary to look into the relative magnitudes of the convective and field effects on the ions with

reference to their specific locations in the total field structure. A convenient parameter for such a comparison is the "slip parameter"

$$S = \frac{U}{kE} = \frac{U}{v_d} = \frac{\text{gas velocity}}{\text{drift velocity}} = \frac{\text{convection effect}}{\text{electrostatic effect}} \qquad (21)$$

When the order of magnitude of the slip parameter is $\overset{o}{=} 1$, convection effects become as important to ion motion and location as the E field, whereas if $S = U/v_d \ll 1$, convection effects would be negligible. Conversely, for $S \gg 1$, the electrostatic effects become negligible. Figures (15 & 16) illustrate the magnitude of this parameter plotted against U for the field point E=20,000 v/cm, and E=Ep.

It is evident from Figure (15) that an ion located in an electric field of strength E=20,000 v/cm, would experience significant convective effects at very low velocities. Figure (16) is an illustration of the slip parameter values at the anode surface, $S=U/v_{dp}$, without considering the effects of space charge. However, it must be remembered that in actuality, a positive ion at the anode surface is located between the tip and a region of high positive space charge, which reduces the effective field strength at its location (See Ep' in Fig. 12).

By reducing the effective value of E_p by an amount $f(n^+)$, then $E_p'=E_p-f(n^+)$, and $S_p=U/k^+E_p'$ increases, which could render convection a significant effect even at the tips of the pins. An important aspect of the quantity U/k^+E_p' is that it is dependent on the gap length, since, as stated earlier, at breakdown:

$$V_b \doteq 7800d + 4000 \quad \text{(volts) and}$$

$$E'_{pb} = \frac{2Vb}{R\log(4d/R)} - f(n^+) \text{ which yields}$$

$$\frac{U}{v_{dp}'} \qquad \frac{U}{k^+2(7800d+4000)/R\log(4d/R)-f(n^+)}$$

Due to the nature of the log term, this yields approximately the following important dependence:

$$S_p = \frac{U}{v_{dp}'} \doteq \frac{U}{d-f(n^+)} = \frac{(U/d)}{1-\frac{f}{d}} \doteq \frac{U}{d}\left(1+\frac{f}{d}\right) \doteq \frac{U}{d}\left[1+c\left(\frac{i}{d}\right)\right] \qquad (22)$$

What this equation effectively says is that at short gaps, the convective effects will become more prominant and may tend to dominate the discharge, while at longer gaps, at least through the range tested, both factors may be important. It is noteworthy that the quantity $f(n^+)$ is proportional to the current, since the charged particle density is proportional to the current. This factor would

also tend to increase the slip parameter as the current increased.

The alternative to attempting to analyse the exact magnitude of the effective electric field at the anode surface is to inspect the available data for evidence of significant flow effects which may alter the breakdown voltage characteristics due to creation of a sufficiently high slip parameter at the anode surface.

A closer inspection of the data of Figure (10) indicates a reversal of the declining trend in V_b vs. U for those gaps greater than about 2 cm in the range of 60-90 m/sec flow velocity. Therefore, it is assumed that this is the velocity region in which convection begins to seriously affect the ion population closest to the pins. The current vs. velocity curve also indicates that the current starts to rise sharply in this range, so the combined effects of high velocity, high current, and short gap (Eq. 22), appear to significantly alter the dynamics of the situation. Since convection becomes important, it is reasoned that, in a certain characteristic time interval (The time between current pulses or breakdown streamers seems to be appropriate in this case, and can be estimated from the pulse frequency cited in the introduction as

$T_f \doteq \frac{1}{f} \doteq 10^{-4}$-$10^{-5}$ sec.), the ions are displaced by such an amount away from the pin tip anodes, that the space charge no longer acts as an anode extension. Instead it becomes a detached region of floating charge, no longer able to act as a bridge for infeeding electrons at the head of succeeding avalanches, to run all the way into the anode itself. Figure (17) illustrates the various stages of progression of the events just described. A separate shortening effect of the anode extension, due to high current density and recombination, may also play a part in the observed voltage characteristic rise, and it will be discussed fully in the next section in connection with observations in the cross-flow mode.

To summarize up to this point for the ordinary flow mode, the sequence of events as described is as follows:

(a) No Flow

$$S = U/v_d = 0 \qquad \text{Fig. (17a)}$$

The physical gap is effectively reduced by the concentration of space charge. The effective gap is $d'_o = d-\delta_o$, and $V_b/V_{bo}=1.0$.

(b) Intermediate Flow (IF):

$$S = U/v_{d(20K)} \overset{o}{=} 1 \qquad \text{Fig. (17b)}$$

Convective effects extend δ further into the gap and $d'_{IF} = d'_o - UT$. $V_b/V_{bo} < 1.0$.

(c) Fast Flow (FF):

$$S_p = U/v_{dp}' \overset{o}{=} 1 \qquad \text{Fig. (17c)}$$

Space charge detaches from tip and $d'_{FF} > d'_{IF}$, so V_b/V_{bo} begins to increase again.

Biblarz and Nelson (Ref. 16) stated that the maximum observed voltage ratio in the ordinary flow mode equaled but did not exceed the maximum reverse flow value of 1.13 for the 3.9 cm gap in their tests. This observation is consistent with the present model, since 1.13 is the maximum ratio for any flow mode and represents the entire physical gap.

There still remains the strange behavior of the breakdown voltage curve for the short gap depicted in Figure (10). Going back to Eq. (22), recall that $U/v_{dp}' \doteq \frac{u}{d}(1+c\frac{j}{d})$, so it would be expected that at sufficiently short gaps and high currents, convection effects would dominate the space charge at the tips, even at very low velocities. This would lead to early (low velocity) separation of the space charge from the anode, resulting in an early rise in breakdown voltage probably to a near

constant value at or below $(V_b/V_{bo})_{(max)}$ since, as decreased, $d' \rightarrow d$. The data for the 1.6 cm gap appear to be a manifestation of this phenomenon.

A numerical example may help to clarify the ideas outlined above.

Let d=3 cm gap length

$$V_b \triangleq 7800d+4000 \doteq 27400 \text{ volts} \qquad (18)$$

Location of field point E=20,000 v/cm from Eq. (17):

$$\delta_{20K}=.45 \text{ cm} = \delta_o$$

Effective gap length (due to space charge presence):

$$d'_o = d - \delta_o = 3 - .45 = 2.55 \text{ cm}$$

Effective electric field (neglecting ΔV):

$$E'=V_b/d'_o = 27000/2.55 = 10{,}588 \text{ v/cm}$$

Assume $T_f \doteq 2(10)^{-5}$ sec, U= 76 m/sec = 7600 cm/sec

Anode extension due to convection:

$$x = UT_f = 7600(2\text{x}10^{-5}) = .15 \text{ cm}$$

$$d'_U = d'_o - UT_f = 2.55-.15 = 2.40 \text{ cm}$$

and finally,

$$V_b/V_{bo}=E'd'_U/V_{bo}=10.588(2.4)/27.0 = \underline{.94}$$

Experimental values for V_b/V_{bo} in the 76 m/sec velocity range fall in the <u>.94-.96</u> range, with the current relatively

constant for all measurements. Above this velocity, convection at the tip, and/or the decreasing recombination distance (to be explained in next Section) takes over, and the effective gap length and V_b begin to increase again.

(5) Turbulence Effects on Breakdown Voltage. Figure (18) is a schematic of visually observed spatial characteristics of the tip glow patterns around the pins under no-flow, laminar flow, and turbulent flow conditions. It can be seen that the intense glow region of (a) is greatly extended by convection, (b), and that the addition of turbulence tends to spread the glow over a much larger region. In fact, turbulence appears to shorten the maximum extent of the glow under some conditions. It would seem probable that this spreading and reduction of the glow region would have an effect on the breakdown voltage. In fact, according to the model, it should increase V_b, due to physical shortening of δ. This trend is well illustrated in Figure (10), where the curves for the 2.9 cm gap show a definite upward shift with increasing turbulence level. The symbols, in order of increasing turbulence, are ▽, □, . It should be noted that these symbols also indicate the order of increasing current, so again, increased current density could cause faster recombination

and smaller anode extension which would also cause an increase in V_b. Figures (19, 20) are photographs of the discharge section which illustrate the patterns of Figure (18).

The next section analyzes in more detail the nature of flow and charged particle interactions in the cross-flow mode.

(6) Cross-Flow Stability and Field Interactions. Figure (21) is a schematic representation of the space charge, electric and cross-flow field interactions as envisioned with the present model. The visual character of the discharge, as observed in many tests, appears to bear out the conclusions reached in the following analysis.

Under no-flow conditions, the discharge gap experiences an apparent anode extension δ_o, due to space charge accumulation as in Figure (17a). As pointed out in the last Section, this apparent extension results in a reduction of effective gap length to $d'_o = d - \delta_o$. It was assumed that the breakdown voltage was proportional to d'_o, so the maximum voltage ratio attainable in this configuration would be realized if the space charge could be removed completely, resulting in $d'_o \rightarrow d$ and $V_b/V_{bo} \rightarrow d/(d - \delta_o)$.

Due to the nearly orthogonal orientation of the electric and flow fields in the cross-flow arrangement, these two effects operate nearly independently of each other to impart motion to any ionic space charge under their respective influences. For example, a positive ion formed at the tip of pin (a) in Figure (21) would experience electrostatic drift and convective motion as follows:

X direction: $v_x = U$

Y direction: $v_y = k^+ E(y)$

The important result is that the space charge location is strongly influenced by the magnitude of U. Taking the tip of pin (a) as the origin, the downstream displacement is:

$s = Ut$ (cm)

U = gas velocity (cm/sec)

$t \doteq T_f$ = time (sec)

For U = 30 m /sec (3000 cm/sec), and $t = T_f \doteq 2 \times 10^{-5}$ sec, the displacement $x \doteq 0.06$ cm. For small tip radii, this amount of displacement can severely alter the local field structure, resulting in an asymetric field distribution. Consider the region between the displaced space charge and the anode for example; this region would be characterized by a relatively weak field as the opposing positive point and space charge fields tend to

cancel each other. On the other hand, the region from which the space charge was removed will be at near the full undisturbed point potential. The undistorted high field region on the upstream side of the pins would then be a source of continuous, stable corona, as electron avalanches feed into it and the space charge is quickly removed by convection. Visual observations of a cross-flow discharge give the impression that the stable, blue-violet glow, which characterizes region 1 of Figure (21), leans into the wind. This result at first seems contrary to intuition, but on closer inspection, it appears to be a natural result of the field interactions.

On the other hand, while removal of space charge from region 1 enhances stability there, convection of that charge into region 2 promotes instability.

It has been shown elsewhere (Ref. 7) that the presence of space charge enhances ionization in a uniform gap if the reduced field (E/P) is less than one half the Stoletow constant B, which for air is 365 volts/cm-torr, and B/2=183 v/cm-torr. This is much higher than E/P in the non-uniform gap used in the present investigation, except in the immediate vicinity of the anode. It is evident then, that convection of space charge into region 2 will result in ionization instabilities there.

Manifestation of the instability described above takes the form of numerous arcs across the gap, commencing generally from the second and third rows of pins, and spreading to the first row of pins just prior to breakdown. Even while heavy arcing is taking place from the first row of pins however, the arcs are confined to the region behind the blue-violet glow which marks the beginning of the discharge activity, thus demonstrating the destabilizing effect of the space charge.

Since the power supply used in these tests is designed to "trip" on overvoltage and overcurrent (and it does faithfully in the ordinary flow mode), the numerous arcs observed must be limited to fairly low currents, and it is not until applied voltage is raised to the value required to break down the relatively space-charge-free gap across the first row of pins that complete breakdown occurs, resulting in a large current pulse with resultant power supply shutdown.

Actual breakdown streamer propagation velocities have been reportedly measured in the 10^7 to 10^8 cm/sec range (Refs. 4, 10, 12), so that the breakdown streamer can travel the width of the gap (in the ranges tested) virtually unaffected by the gas velocity. For

example, in the longest cross-flow gap tested, d=3.2 cm, the time of transit of a primary breakdown streamer is $t=d/v = 3.2/10^7 = 3.2\times10^{-7}$ sec. The displacement of an average molecule or ion by convection in this time interval, even at U= 150 m/sec is $Ut \doteq 5\times10^{-3}$ cm. The result is that in the cross-flow mode, alteration of the field structure begins at low gas velocities by space charge convection, resulting in a stable upstream region of very low space charge, and a downstream region of instability caused by space charge distortion effects. Breakdown occurs across the nearly space-charge-free gap upstream at a value of $V_b/V_{bo} \doteq d/(d-\delta_o)$, virtually unaffected by gas convection due to the high propagation velocity of the breakdown streamers.

(7) Observed Effects of Charged Particle Density on Recombination Times. A very interesting phenomenon was observed during the course of the cross-flow tests. While heavy arcing took place across all rows of pins, undistorted by convection due to their high propagation velocity, a secondary pattern of luminous filamentary channels was also evident which appeared to be very much affected by the convective velocity (Fig. 21). Contrary to intuition again, however, the luminous secondary

streamers are convected a shorter distance at higher velocities. Their intensity also increased with increasing velocity. Figure (22) is a graph of recombination distance observations vs. velocity.

In order to understand this behavior, it is necessary to focus on the exact mechanism which is responsible for these luminous streamers. In the streamer theory, the formation of a highly ionized channel from anode to cathode results in a highly conductive channel through which massive quantities of secondary electrons flow, having been released when the propagating streamer strikes the cathode. When the arc is extinguished, a column of space charge remains which is made up of positive and negative ions and electrons. When radiative recombination takes place between particles of opposite charge, whatever the particular specific mechanisms, energy is released in the form of photons. The secondary streamers are believed to be caused by the massive recombination of the charged particles left in the aftermath of an arc.

The standard approach to the recombination problem (Refs. 4, 7, 8, 13) is as follows: where charges of opposite sign reside together, they will be mutually attracted to each other, and so will come together, exchange

charge and neutralize each other, emitting radiation in the process. There are several varieties of recombination, all of which are discussed in detail in the references cited. It is sufficient for the present to say that the recombination rate will be at least proportional to the numbers of charged particles available, although the proportionality varies with the process, so the change in the number of existing particles in a time (dt) will be given by an expression of the form:

$$dn = - \alpha_r n^+ n^- dt \tag{23}$$

where α_r is a constant of proportionality. The number of negative charges is not always equal to the positive charges, but n^- can be expressed as a fraction of n^+.

$$n^- = cn^+$$

where c could also vary. Now, calling $n^+ = n$, with the aid of the above, Eq. (23) can be written as

$$dn = - \alpha_r c n^2 dt$$

and

$$dn/n^2 = - \alpha_r c dt \tag{24}$$

which, when integrated yields the following:

$$1/n - 1/n_o = \alpha_r ct$$

showing that:

$$t_{rec} \doteq 1/ \alpha_r c(1/n - 1/n_o) \tag{25}$$

Reference (13) states that recombination phenomena are usually recognized by the linear dependence of t on 1/n. But n is directly proportional to j, the current density:

$$j = e(n^+v^+ + n^-v^-) = en(v^+ + v^-c) \qquad (26)$$

and also, it has been shown by other experimenters (Ref. 14) and empirically from the present experiments that $j \doteq U^2 \doteq n$. Making use of this relation between n and U in Eq. (25) leads to the following:

$$t_{rec} \doteq 1/U^2$$

Multiplying both sides by the gas velocity U gives the distance traveled during recombination in the arc-caused space charge column:

$$x_{rec} = Ut_{rec} \doteq 1/U$$

which is the observed dependence.

It is possible to do an order of magnitude analysis of x_{rec} by going back to Eq. (25). Assuming that $c \overset{o}{=} 1$, which is reasonable under these circumstances, and $\alpha_r = 2(10)^{-6}(cm^3/sec)$ (Ref. 13). If it is assumed that the final number of charged particles is $\doteq .1n_o$ (90% recombination), then

$$t_{rec} = (1/2\cdot 10^{-6})(1/.1n_o - 1/n_o) = (1/2\cdot 10^{-6})(9/n_o) \qquad (27)$$

The relation between n_o and U can be estimated by solving for the current in terms of n and U

as follows:

$$j \doteq en(k^{+}E + k^{-}E) \tag{28}$$

which reduces to

$$j \doteq en(k^{-}E) = env_d^{-} \tag{29}$$

since $k^{+} \ll k^{-}$. The drift velocity of electrons is difficult to estimate due to the variable field and severe space charge modification, but a reasonable approximation is the streamer propagation velocity $\doteq 10^7$ cm/sec (Ref. 12). This gives

$$j \triangleq 1.6(10^{-19})(10^{7})n_o = 1.6(10^{-12})n_o \tag{30}$$

Now, from observed data, j(U) can be calculated, assuming $j \doteq U^2$. Taking a point from the data for atmospheric pressure and no turbulence;

$$j = 15 \text{ ma} = AU^2$$

where typically $U \triangleq 10^4$ cm/sec.

Then

$$j = .015 \text{ amps} = A(10^4)^2$$

$$A = 1.5(10^{-10}) \text{ (amp-sec}^2/\text{cm}^2)$$

and

$$j \doteq 1.5(10^{-10})U^2 \tag{31}$$

Now, equating (30) and (31),

$$n_o = 90U^2 \text{ (ions/cm}^3) \tag{32}$$

This yields a value of $n_o \cong 10^8\text{-}10^9$ ions/cm^3, which is a reasonable value.

Now, plugging this value of n_o back into Eq. (24),

$$t_{rec} \cong 1/2(10^{-6})(9/90U^2) \text{ and}$$

$$x_{rec} \cong 5(10^4)/U \text{ (cm)} \qquad (33)$$

which yields for $U = 10^4$ cm/sec,

$$x_{rec} \cong 5 \text{ cm}$$

It can be seen that the order of magnitude of the terms involved appears to approximately agree with the observed data. This tends to substantiate the basic assumptions regarding the secondary filaments as a recombination phenomenon. Figure (22) shows the comparison of Eq. (33) with observed data.

Assuming that the dependence illustrated in the preceding paragraphs holds for the "ordinary" flow mode, it can be seen that this idea can also be applied to the "virtual" anode concept in the following manner. Since x_{rec} is a measure of the maximum extent of the space charge, it must be proportional to δ, the anode extension, which is also a measure of space charge extent. This leads immediately to the following result:

$$x_{rec} \triangleq \delta \triangleq (1/U)C$$

and

$$V_b \triangleq V_{bo}(d-\delta) \doteq V_{bo}(d-C/U) \qquad (34)$$

so as U increases, V_b increases. This effect has, of course, been observed as noted in the previous section at velocities above ≐ 75m/sec. As a result of the above, it is difficult to determine at this point which process, detachment of space charge from the anode or increasing recombination rate, or a combination of the two, is responsible for the upward swing of the V_b/V_{bo} vs velocity curve in the ordinary flow mode (Fig. 23).

(8) Reverse Flow Convection Effects. In this orientation (Fig. 9b), with no flow, the static anode extension exists as in Figure (17a). As velocity is increased, any positive ion located anywhere off the pin tip stagnation streamline will experience velocity components in the y direction due to the radial component of the anode electric field and in the negative and positive x directions due to convection and axial electric field components. The total velocity in vector form will be

$$\bar{v} = k^{+}\bar{E}+\bar{U}$$

where the positive direction is from anode to cathode.

Due to the radially directed field lines near the pin tips, the resulting space charge pattern will tend toward the pattern of flow produced with a source flow immersed in a uniform flow field. The result is that velocity has a direct shortening effect on the anode extension; but also note that the space charge tends to spread radially which reduces the charge density and therefore the field strength. The reduction of δ and spreading tendency reduce the probability of streamer formation due to high charge concentrations, and thus reduce the current flow. Reduction in current means less charge, and so the glow collapses (this point will be covered in more detail in a later Section), which quickly reduces the space charge distortion to the point that the breakdown voltage approaches the upper limit as δ approaches zero (Fig. 24). It would be logical to assume that most, but probably not all, of the space charge anode extension would be destroyed or reduced below the critical level, and $V_b/V_{bo})_{max} = d/(d- \delta_o)$.

It can be seen from Figure (14) for the reverse flow mode that this was the case. $V_b/V_{bo})_{max}$ for a 3.9 cm gap is predicted by the present model as 1.16 and the experimental value was $1.13 \leqq V_b/V_{bo})_{max}$.

Werner (Ref. 15) reports on some work with a negative point-plane gap with velocity from the plane (anode) to the point (cathode). The resulting space charge pattern and dynamic processes should be similar to that described above, only with the negative ions playing the part of the positive ions in the former case. It might be expected then that the negative point would experience trends in the same direction as a positive point in regard to breakdown voltage and current changes with increasing velocity. It turns out that this is the case. Breakdown voltage increased with increasing velocity with a maximum $V_b/V_{bo} \doteq 1.08$. Calculating $V_b/V_{bo})_{max}$ for this case from Eq. (20) yields $\doteq 1.25$, so the voltage ratio is less than the maximum. Reference (15) also reported no distortion in the glow pattern with flow while being observed under a microscope except for a reduction of size. This would be a logical result of the process described above for the positive point-to-plane since convection causes glow collapse, and an equilibrium glow region would be established which was much smaller than the no-flow glow.

The apparent reduction of current at constant voltage in the reverse flow mode is of further

importance. Reference (16) reported no appreciable change in breakdown current in the reverse flow mode over the ordinary mode. This implies a reduction in current at a given voltage, since V_b increased appreciably; while Reference (13) definitely experienced lower currents at a given voltage with flow as the present analysis would expect. This fact will make it possible to determine the correct form for the functional dependence of the discharge current on velocity which will be undertaken in the next section.

(9) Analytic Considerations in $I = f(U)$. While many investigations have derived expressions for current vs. velocity of the form $I \doteq U^2$ (Ref. 14), it can be shown that a more appropriate expression is $I \doteq (\exp)^U$.

In order to see this, it is necessary to examine some facts about the functional observed dependence. It is known that

$$I = f(U) \qquad \text{Condition (1)}$$

and within practical limits of velocity,

$$I \geq 0 \qquad \text{Condition (2)}$$

Also, when $U = 0$, $I = I_o$ (the no-flow value). Condition (3)
It has been shown also that when $U < 0$ (reverse flow) the current tends to decrease. This implies that

$$dI/dU \geq 0 \text{ at } U = 0 \qquad \text{Condition (4)}$$

and from References (15, 16),

$$dI/dU \geq 0 \text{ at } U < 0 \qquad \text{Condition (5)}$$

There are several functions which could satisfy conditions (1 & 2), but two of the simplest are:

$$\begin{aligned} I_1 &\doteq U^2 \\ I_2 &\doteq (\exp)^U \end{aligned} \qquad (35)$$

To satisfy condition (3), these can be written:

$$\begin{aligned} I_1 &= AU^2 + I_o \\ I_2 &= I_o(\exp)^{CU} \end{aligned} \qquad (36)$$

Now,

$$\begin{aligned} dI_1/dU &= 2AU \qquad (a) \\ dI_2/dU &= I_o C(\exp)^{CU} \qquad (b) \end{aligned} \qquad (37)$$

It can be seen that Eq. (37a) does not satisfy condition (5), but (37b) does provided that C is a positive number. Therefore, the equation which meets all the appropriate conditions can be written

$$I = I_o(\exp)^{CU} \qquad (38)$$

In a later section it will be shown that, from a physical standpoint, the exponential form for velocity dependence evolves quite naturally, although in a slightly different form than Eq. (38).

B. GASDYNAMIC EFFECTS ON DISCHARGE CURRENT (NON-UNIFORM FIELD)

As stated in the Introduction, a point-to-plane discharge can be divided into distinct regions due to the divergence of the applied electric field distribution. These are (1) an intense region of ionization near the point, (2) a space charge region fed from the ionization region by electrostatic repulsion of positive ions, and (3) the quasi-neutral region in which the applied electric field has dropped below the value necessary for appreciable ionization activity. This last region is disturbed more and more, however, as gap breakdown is approached by the intrusion of pre-breakdown streamers whose maximum lengths are proportional to applied voltage (Ref. 9). The actual length of any one streamer is a statistically varying quantity due to the nature of the dynamic processes involved. The amount of current associated with a specific streamer is proportional to its length, and current is also proportional to streamer frequency. Since both streamer length and frequency are proportional to applied voltage, the current must be nearly proportional to the square of the voltage.

Several empirical expressions have been used to describe the current-voltage relationship in a point-to-plane

discharge under no-flow conditions. Reference (7), for example, gives the following empirical formula for a positive point-to-plane:

$$I_o = CV(V-M) \tag{39}$$

where M is the starting potential of the corona current, and C is a function of the geometry and gas related variables. This formula gives the V^2 dependence previously mentioned, and has been found to satisfactorily describe the I-V characteristic under no-flow conditions.

Combining this expression with the current-velocity dependence developed in the preceding section, the equation is now

$$I(U) = I_o(\exp)^{CU}$$

where I_o is given by Eq. (39). I_o can also be written as $I_o = CkV(V-V_c)$ which explicitly reveals the density dependence in the mobility $k \doteq k_o(\rho/\rho_o)$ (Ref. 11). This expression is also too limited, however, since it does not provide any means of introducing the effects of turbulence on discharge current. Since turbulence has proven to be a significant parameter, an equation to describe gasdynamic effects on a discharge must be capable of reflecting turbulence as well as convection and density change effects. Such an expression can be found by going back to the basic

physical mechanism of current production in a gaseous discharge, the electron avalanche.

In the special case of a uniform field with no space charge, the current (i) produced by an electron avalanche can be expressed as a function of the Townsend first ionization coefficient α in the following way (Refs. 4, 7, 8, 12):

$$i = i_o(\exp)^{\alpha x} \tag{40}$$

This equation indicates the exponential increase in current due to the nature of the electron avalanche process and is well described in the references cited. This expression becomes more complicated in a non-uniform field where α being a function of the electric field, changes with x. It is then necessary to integrate α over the distance of avalanche travel:

$$i = i_o(\exp)^{\int_o \alpha(\zeta)d\zeta} \tag{41}$$

For purposes of the present discussion an effective can be defined over the avalanche travel distance:

$$\alpha_{eff} = (1/x)\int_o \alpha(\zeta)d\zeta$$

where x is the avalanche travel and $0 \leq \zeta \leq x$, then

$$i = i_o(\exp)^{\alpha_{eff}x} \tag{42}$$

The subscript notation for α will be dropped for convenience, but it must be remembered that in a non-uniform field with space charge, α can vary in the space of a mean free path.

A commonly used semi-empirical expression for α is the following (Ref. 4):

$$\alpha/p = A(\exp)^{(-BP/E)} \tag{43}$$

where A and B are constants of the specific gas under consideration. For air, Reference (4) gives

A = 15 ionizations/cm-torr

B = 365 volts/cm-torr

with a reduced field range of validity of

E/P = 100-800 volts/cm-torr.

Of course, the current measured in a point-to-plane discharge circuit is the sum of many small avalanches which form primarily near the point in the high field region; but streamers, which propagate far into the low field region are also built up from numerous secondary avalanches feeding into the tip of an advancing streamer. It seems apparent that any analysis of gasdynamic effects on discharge current, and hence power, must begin at this level to determine how the gasdynamics affect the electron avalanche.

1. Pure Convection Effects on Current

Consider first the effects of pure convection. The model used in discussing breakdown voltage predicts that extension of the space charge region will initially occur as gas velocity is increased. This anode extension effectively moves the boundary of the high field region further from the anode, resulting in a longer average electron avalanche travel distance (Fig. 25). (Note that in discussing breakdown voltage, the apparent anode extension was thought of as a reduction of effective gap length, and in discussing current effects, it is an increase in avalanche travel.) Recalling from the numerical example computed earlier the no-flow anode extension δ_o was 0.45 cm, and the apparent increase above this due to convection was 0.15 cm. An avalanche commencing at the beginning of the critical space charge region with convection would only travel 0.15 cm further than in the no convection case. This does not seem like much, but a simple calculation of avalanche current from Eq. (40) for both cases leads to surprising results. Using an average field strength of E_{avg}=50,000 volts/cm, P=760 torr:

$$\alpha = AP(\exp)^{(-BP/E)} = 44.4 \text{ ionizations/cm}$$

and since $(i/i_o) = \exp^{\alpha x}$, for x = 0.45 cm (no flow):

$$i/i_o)_{NF} = 4.77(10^9)$$

and for x = 0.45 + 0.15 (with flow):

$$i/i_o)_F = 3.71(10^{11})$$

and the increase of current for this single avalanche is

$$\frac{i/i_o)_F}{i/i_o)_{NF}} \doteq 80$$

Although the numbers used above are only order of magnitude correct, the obvious conclusion is that even very small distortions of E-field structure by space charge convection can cause large changes in current.

It is worthy of note at this point that the exponential current-velocity dependence derived in the previous section from purely empirical and functional considerations, turns out to be the same form the physical model would predict, that is an exponential increase due to increased avalanche travel in the high electric field region.

2. Current-Voltage Characteristics

As a further test of the space charge model proposed, it is instructive to look at other observed I-V characteristics. For example, the standard, no-flow I-V curve is known to be well described by the empirical

expression of the form of Eq. (39). Now, in terms of physical processes, consider point-plane electrodes with increasing voltage. There will be no ionization activity until the point reaches the potential required for ionization of the surrounding gas molecules, which gives rise to the "inception" voltage (M or V_c), at which the corona current starts as small weak pulses caused by the initial formation of the electron avalanches. As voltage continues to rise, the high field front of the electric field moves out into the gap, causing the average distance at which avalanches can form to move with it. As already demonstrated, this results in a rapid rise in current, which, from a physical standpoint, is better described by an exponential function rather than a U^2 type of empirical fit.

A simplified representation can be obtained for the total current by observing the general form of the result of a summation of several individual avalanche currents. This will be useful in later developments and for a general trend analysis to further test the validity of the proposed model.

Assume that the total number of avalanches per unit time is N. Then the total current is

$$I = \sum_{j=1}^{N} i_j = i_1 + i_2 + \ldots$$

Since most activity takes place in the same small region of the pin tip, let the following average quantities be defined:

$$\bar{x} = (1/N) \sum_{j=1}^{N} x_j$$

$$\bar{\alpha} = (1/N) \sum_{j=1}^{N} \alpha_j$$

$$\bar{i}_o = (1/N) \sum_{j=1}^{N} i_{oj}$$

Summing up all the avalanche contributions, the total current is

$$I_o = i_1 + i_2 + \ldots = \bar{i}_o (\exp)^{\bar{\alpha}\bar{x}} + \bar{i}_o (\exp)^{\bar{\alpha}\bar{x}} + \ldots$$

$$I_o = C_1 (\exp)^{\bar{\alpha}\bar{x}} - C_2$$

where $C_1 \doteq \bar{i}_o N$ and C_2 is a function of the electrode geometry, since no exponential increase in current can take place until the electric field strength at the electrode surface at least reaches the ionization strength of the gas surrounding it. Discounting normal saturation currents due to free electrons which are always present in the air,

C_2 can be evaluated by the fact that $I_o = 0$ at the inception of the corona current:

$$I_o = 0 = C_1(\exp)^{\bar{\alpha}\bar{x}} - C_2$$

so

$$C_2 = C_1(\exp)^{\bar{\alpha}\bar{x}} \qquad \text{at corona ignition}$$

but at the point when ionizing activities first commence, $\bar{x} \doteq 0$, and

$$C_2 = C_1(\exp)^{0} = C_1 = C$$

and, therefore,

$$I_o = C(\exp^{\bar{\alpha}\bar{x}} - 1) \qquad (44)$$

Equation (44) is the basic physical result for non-uniform fields under no-flow conditions as derived from the space charge model. The associated constant is again a function of gas type, density and electrode geometry. It is interesting to note that this is nothing more than the expression for current between parallel plates in a uniform field, written to accommodate variable geometry.

Closer inspection of the constant $C = \bar{i}_o N$ shows that it is still a function of streamer length $L \doteq f(V)$ and frequency $N \doteq f \doteq V$, so C_1 can be rewritten as CV^2 and then Eq. (44) can be written as

$$I_o = CV^2(\exp^{\bar{\alpha}\bar{x}} - 1)$$

or, taking one V inside,

$$I_o = CV(V\exp^{\bar{\alpha}\bar{x}} - V)$$

and from the condition that $I_o = 0$ and $\bar{x} = 0$ at $V = V_c$, this results in

$$I_o = CV(V\exp^{\bar{\alpha}\bar{x}} - V_c)$$

This is nearly identical with the previous empirical forms for the no-flow condition, except that now the exponential expression introduced permits easy interpretation of gas-dynamic effects on the discharge current.

The $\bar{x}$ in Eq. (44) is proportional to δ, so it will be less confusing to rewrite the current equation in the following form:

$$I_o = CV(V\exp^{C\,\bar{\alpha}\,\delta} - V_c) \qquad (45)$$

remembering that the subscript 'o' represents no-flow conditions. Equation (44) is plotted in Figure (26).

It is now easy to see the effects of increasing velocity on the current, since in the ordinary mode, increases with flow. This would increase the exponent which has the effect of shifting the I-V characteristics up and to the left as in Figures (27 a&b). These curves are typical of the characteristic shifts which have been

observed in the present experimental work. The general form of δ in terms of the other variables is $\delta = \delta_o + UT - f(u) = c\frac{V}{-} + UT - f(u)$, where f(u) is the result of space charge "blowout" and recombination effects.

Looking again at the reverse flow case discussed earlier with the aid of Eq. (45), it is now easy to see how a low current equilibrium situation is established. As soon as there is even a slight distortion (shortening) of the space charge region, the current decreases along an exponential curve, which results in less charge production, further decrease in current, etc., until equilibrium is again established, when the space charge region shrinks far enough into the high field region of the anode that it is no longer affected by convection. Figure (28) summarizes the effects of velocity on δ and the breakdown voltage characteristic curves.

3. Diffuser/Density Effects on Current

The effects of reduced density on the current are also easily deduced from Eq. (45), since as shown earlier, δ increases with a density reduction, but also $\bar{\alpha}(\rho)$ increases with decreasing density over the ranges of reduced pressure discussed so far. (There is an optimum ionization efficiency, $\eta \alpha/E$, which occurs for air at an

$E/P \doteq 365$ volts/cm-torr = B, which will be discussed below (Ref. 12)). The result of this dual exponential effect is a rapid rise in current with decreasing density, until the reduced pressure in the ionization region drops below the optimum. Beyond that point, the effects of density reduction on the current could actually reverse if the ionization efficiency drops too far (Fig. 29).

To arrive at an estimate for optimum pressure for best ionization efficiency, it is possible to write

$$E/P)_{opt} = 365 \text{ v/cm-torr} = B$$

and using $E \doteq 200{,}000$ volts/cm (value at pin for a 3 cm gap, hyperboloidal point-to-plane),

$$P_{opt} \doteq E_p/B = 200{,}000/365 = 547 \text{ torr}$$

The value computed from the data of Reference (18) in Appendix (b) for a 3 cm gap is $\doteq 480$ torr, which is not too far off, considering the approximation inherent in the point model used. (For example, if the point radius were assumed to equal the wire radius of $\doteq 0.08$ cm, then P_{opt}=375 torr). Since the discharge in the present investigation was operated at a pressure well above the optimum value for most efficient ionization, it would be expected that any density reduction produced in the test

section by the addition of a diffuser would enhance ionization significantly, which it does (Fig. 30).

4. Turbulence Effects

While the study of turbulence is, in itself, a complicated field, the basic interactive effects of turbulence on an electric discharge can be qualitatively described with only the most basic characteristics of a turbulent flow field; those of fluctuating, time-dependent variations in gas density and velocity.

The turbulence generated in the discharge section in the present work ranged in frequency from $\stackrel{o}{=}$ 100-20,000 Hz (Ref. 3). This frequency range yields characteristic times $\tau_t = (1/f)$ of the order of $2(10^{-3})$-$5(10^{-5})$ sec. These times are long compared with the characteristic times associated with charged particle kinetic processes (Table I). The result is that the charged particle properties adjust in a quasi-steady fashion to fluctuations in gas properties. Thus, charged particle kinetics and energy transfer processes couple to fluctuations in the neutral gas primarily through changes in gas temperature and density (Ref. 19).

For example, consider a point in a turbulent discharge region; gas density at this location will vary periodically around a mean value. Although the time

average of the fluctuations at the point is zero, and the point experiences as much time at elevated pressures as it does at reduced pressures, the net effect of these fluctuations on discharge current are very significant. This is due to the exponential dependence of the local value of the ionization coefficient on the local reduced pressure (E/P). As long as the discharge (E/P)> B, pressure fluctuations will significantly increase the average effective ionization coefficient.

EXAMPLE: $\overline{P}$ = 760 torr = mean pressure

p = 50 torr = fluctuating component

$\alpha = AP(exp)^{(-BP/E)}$

and using a simple expression for current for illustration:

$$I = I_o(exp)^{\alpha x}$$

Computing ionization coefficients for E = 50,000 v/cm:

$\alpha_{760} = 44.4$ Mean

$\alpha_{810} = 32.9$ High P fluctuation

$\alpha_{710} = 59.8$ Low P fluctuation

Current computations for $I_o = 1$, x = 0.5 cm:

$I = (exp)^{44.4(.5)} = 4.38(10^9)$ Mean

$I = (exp)^{32.9(.5)} = 1.39(10^7)$ High P

$I = (exp)^{59.8(.5)} = 9.67(10^{12})$ Low P

$I_{avg} = (I_{hi} + I_{lo})/2 = 4.83(10^{12})$

The amplification of the current over the mean due to a fluctuation in pressure is then:

$$I_{avg}/I_{mean}=4.83(10^{12})/4.38(10^{9}) = 1103$$

Obviously, the effects of turbulent fluctuations in pressure or density can cause substantial increases in current due to the quasi-steady coupling of electron kinetics to temporal variations of the neutral gas properties.

Local increases in electron/current density, however, can have a great destabilizing effect on the discharge, since increased local current density causes increased joule heating ($j \cdot E$) of the gas. This heating results in local density reduction, increased conductivity and further increases in current density which may result in a runaway condition leading to complete breakdown of the gap (Ref. 20).

Fortunately, it is the basic nature of turbulence that the strongest density fluctuations are accompanied by the highest fluctuating velocity components (Ref. 19). These high velocity components tend to disperse concentrations of space charge, dissipate local hot spots and promote stability. The role of turbulence, then, is two-fold: on the one hand, it enhances ionization, while on the other hand, it jointly acts to prevent an unstable, runaway

condition from developing due to formation of local hot spots in the gas.

Before leaving the subject of turbulence, it is worthwhile to do a general frequency analysis to determine how a given turbulent frequency spectrum will affect a discharge. It was pointed out in Reference (16) that turbulence spectra which were heavily weighted in the low frequency regions gave the best improvement in power enhancement to the discharge.

That this should be so can be seen by analyzing the effects of turbulence more explicitly on the ionization coefficient α. In a turbulent field, $\alpha = \alpha(t)$, and if $f(\omega t)$ is a periodic fluctuation of gas density, then the time average of $\alpha(t)$ over one cycle will be:

$$\overline{\alpha} = 1/T \int_o \alpha(t) dt$$

but since ω is an independent parameter of the problem, it may be included as follows:

$$\overline{\alpha} = 1/\omega T \int_o (\omega t) d(\omega t) \doteq \frac{1}{\omega} \qquad (46)$$

This shows that $\overline{\alpha}$ is inversely proportional to the turbulent frequency components. It should be possible to develop a weighting factor for a given turbulence spectrum

by summing the contributions of the various frequency components to the ionization coefficient. It must be realized, however, if an attempt is made to quantify the effects of a given turbulence spectrum, that inhomogenieties in the turbulence pattern can lead to premature breakdown through a relatively inactive "dead" region of the gap where instabilities may develop uninhibited.

The following is a summary of the gasdynamic effects on discharge current observed in the present experimental work and interpreted in terms of the present model:

a. No-Flow

$$I_o = CV\ (V\exp^{C_1 \bar{\alpha} \delta_o} - V_c)$$

Current commences at an inception voltage V_c and rises on a modified exponential curve until breakdown occurs (Fig. 26).

b. Flow (ordinary mode)

$$I(U) = CV(V\exp^{C\alpha\delta\ (U)} - V_c)$$

The anode extension δ increases due to convection of space charge, shifting the characteristic curve up and left, while $\bar{\alpha}$ also increases due to high space charge in the gap (Fig. 27b).

c. Reduced Density (diffuser on)

δ and $\overline{\alpha}$ increase due to reduced density, and δ also increases due to the convection effect. The result is a large shift of characteristics up and left. The reduced density also reduces the breakdown voltage significantly, and may result in a reduction of maximum power ($I_b V_b$) (Fig. 30).

d. Turbulence (diffuser off)

Substantial improvements in $\overline{\alpha}$ can be realized with the proper type of turbulence, and stability is concurrently enhanced. Mean velocity also causes δ extension due to convection, and a large increase in $\overline{\alpha}\,\delta$ results, with the accompanying shift up and left of the I-V curve (Fig. 27a).

e. Turbulence and Density Reduction (diffuser on)

The combined effects of (c) and (d) above result in maximum I-V shift and high power capacity due to stability enhancement by turbulence.

Figures (19, 20) are a sequence of pictures of the discharge section and the discharge operating under some of the conditions described above, and Figure (18) is a schematic of the pin tip regions as they appeared during visual observation. One additional feature of turbulence

which is evident from these figures is that in addition to homogenizing the discharge region the turbulence creates a much larger ionization region at the anode, which is the major source of the additional current.

5. Maximum Current/Discharge Stability

Figure (31) shows how the breakdown current varied in the present investigations as a function of mass flow rate through the discharge region for the various configurations already mentioned.

The curve for pure convection (no diffuser, no turbulence grid) shows increasing stability with increasing mass flow rate. This stability increase is probably due, at least in part, to convection of heat out of the high current density regions near the pin tips where growing thermal instabilities may develop under no-flow conditions. The data indicate that a limit is apparently being approached in this mode. This would be expected in a relatively smooth laminar type of flow, since the joule heat developed at a pin tip would flow toward the cathode with relatively slow radial diffusion, resulting in a column of heated gas between anode and cathode, increasing the conductivity and breakdown probability of the gap.

The addition of the diffuser raises the curve, thus indicating a stabilizing effect associated with reduced density. This stabilization can most probably be traced to the increased diffusion rates of charged particles, reducing high density charge build-up, and increased thermal conductivity, which also tends to reduce local heating. The problem of laminar flow is still present, however, and it can be seen that, once again, a current or power limit is being approached as mass flow rate increases.

The addition of the turbulence generating screen in either of the above configurations demonstrates a very marked increase in stability, with no apparent saturation limit being approached within the limits of the power supply capabilities used in the present investigations. It thus appears that the fluctuating, large scale, high intensity velocity components introduced are very effective in enhancing discharge stability. This enhancement is presumed to act through intense mixing of ionic space charges with surrounding areas, and rapid dissipation of heat from local regions of the discharge gap. The result is a smoothing out of the electric field distortion caused by space charge, and a rapid redistribution of heat

throughout the entire discharge volume, whereas in the laminar flow cases, the heat was confined to relatively small columnar volumes between anode and cathode.

The most effective screen design turned out to be a redesigned "number 9" screen of Reference (6). Reference (3) gives detailed engineering data on all equipment used in the present work. One of the significant features of the redesign was the incorporation of large boundary layer bleed areas around the discharge volume (Fig. 2). Flow velocities measured through this boundary layer region were 2-3 times the average discharge velocity with the turbulent screen in place. It is felt that this high velocity region serves as a heat sink for the discharge and greatly enhances the thermal stability by very rapid removal of waste heat generated in the discharge region.

Reference (3) should also be consulted for an interesting approach to power input optimization for the type of flow device used in this work.

V. CONCLUSIONS

It appears that the space charge convection model presented here is a valid approach to electric discharge and gasdynamic interaction analysis in highly non-uniform fields. The model has also been shown to hold as an approximation to discharge breakdown properties in a uniform field, and so may not be limited to non-uniform geometries where it appears to describe many observable effects concerning gasdynamic interactions.

Gasdynamic interactions promote stability of a discharge in several ways, through pure convection, density reduction, and turbulence. It appears that the basic mechanism of all three of these is through thermal stabilization by heat removal from potentially developing "hot spots" in the gas.

High intensity, low frequency turbulence is best for stabilization. This fact may permit quantitative analysis of individual turbulence spectra for use in optimization studies.

The addition of a diffuser and turbulence generating screens results in much higher power input at lower mass

flow rates, and therefore is an important economic consideration in the construction of larger devices of this type.

VI. RECOMMENDATIONS

A. The major recommendation resulting from this study is that, initially, more comprehensive testing should be done on all aspects of the gasdynamic/flow interactions reported in order to establish accurate empirical inputs required for optimization studies. Concurrently, attempts should be made to derive accurate relations among the parameters discussed using the Poisson Equation and appropriate flux equations.

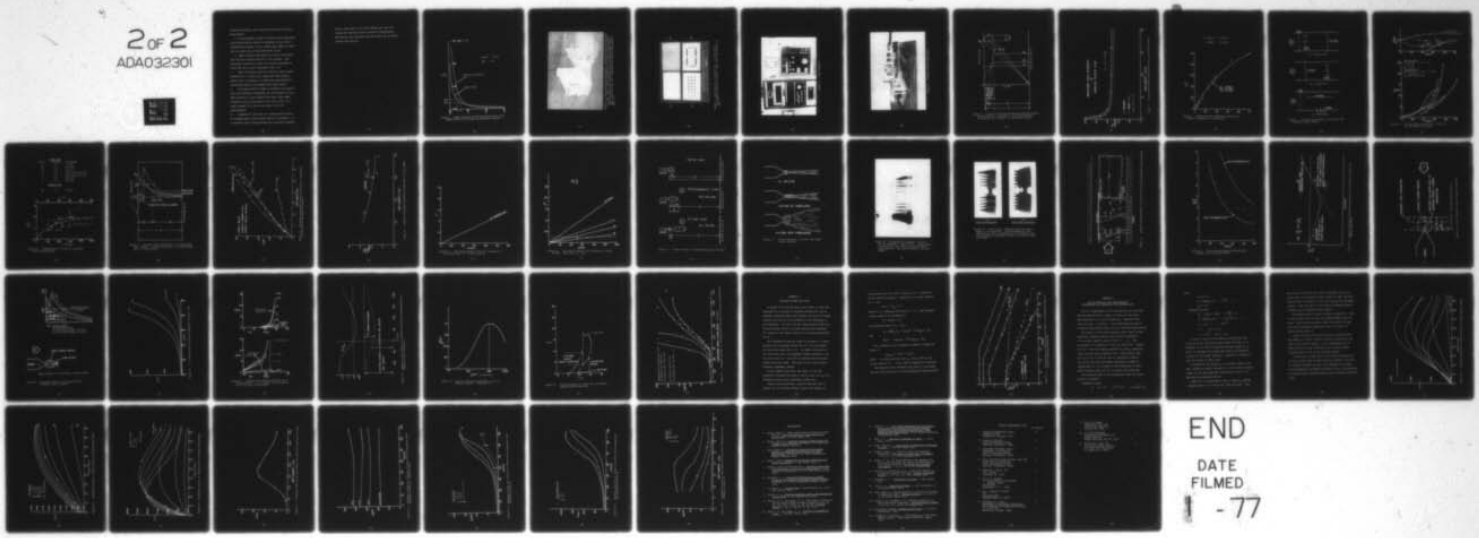
B. The stability problem is probably the most critical and complex, but since it is the key limiting performance parameter for high pressure discharges, an accurate means of quantification is necessary which properly reflects the influence of gas dynamics. It is hoped that the relatively simple model presented here will aid in visualization of the stability problem and the gasdynamic factors which affect it. In regard to discharge stability, it is specifically recommended that the following tests be performed:

1. Current distribution studies should be performed for correlation with temperature profiles and breakdown

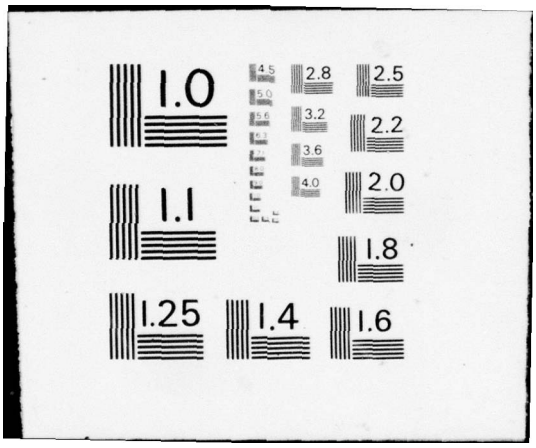
AD-A032 301 NAVAL POSTGRADUATE SCHOOL MONTEREY CALIF F/G 20/5
GASDYNAMIC EFFECTS ON AN ELECTRIC DISCHARGE IN AIR.(U)
SEP 76 J L BARTO

UNCLASSIFIED NL

2 OF 2
ADA032301



END
DATE FILMED
1 -77


1.0
1.1
1.25
1.4
1.6
1.8
2.0
2.2
2.5
2.8
3.2
3.6
4.0
4.5
5.0
5.6

location statistics, and turbulence and velocity profile measurements.

2. Oscillographic studies of current and voltage waveform characteristics should be attempted in the various configurations tested, and at various gap lengths to determine the exact type of breakdown which occurs.

3. Small diameter wire should be tried as the anode, with the wires mounted parallel to the cathode. Wire electrodes resulted in a much more uniform discharge in recent MHD laser cavity experiments (Ref. 22).

C. Since the present work was limited by power supply capabilities, a larger power supply with much greater power output is necessary to extend the investigation of optimum gap length, and maximum power input limits.

D. An attempt should be made to determine more specifically the mechanism responsible for the increase in V_b at high velocities in the ordinary flow mode, since small increases in V_b at that point in the curve result in a large increase in I_b due to the slope of the I-V characteristic.

E. Extension of this work to a lasing mixture should be attempted when a better power supply is available. It is believed that a lasing mixture may prove more thermally

stable, since most of the input energy goes into the vibrational molecular states instead of translational gas heating, and therefore even more power can be stably coupled into the gas.

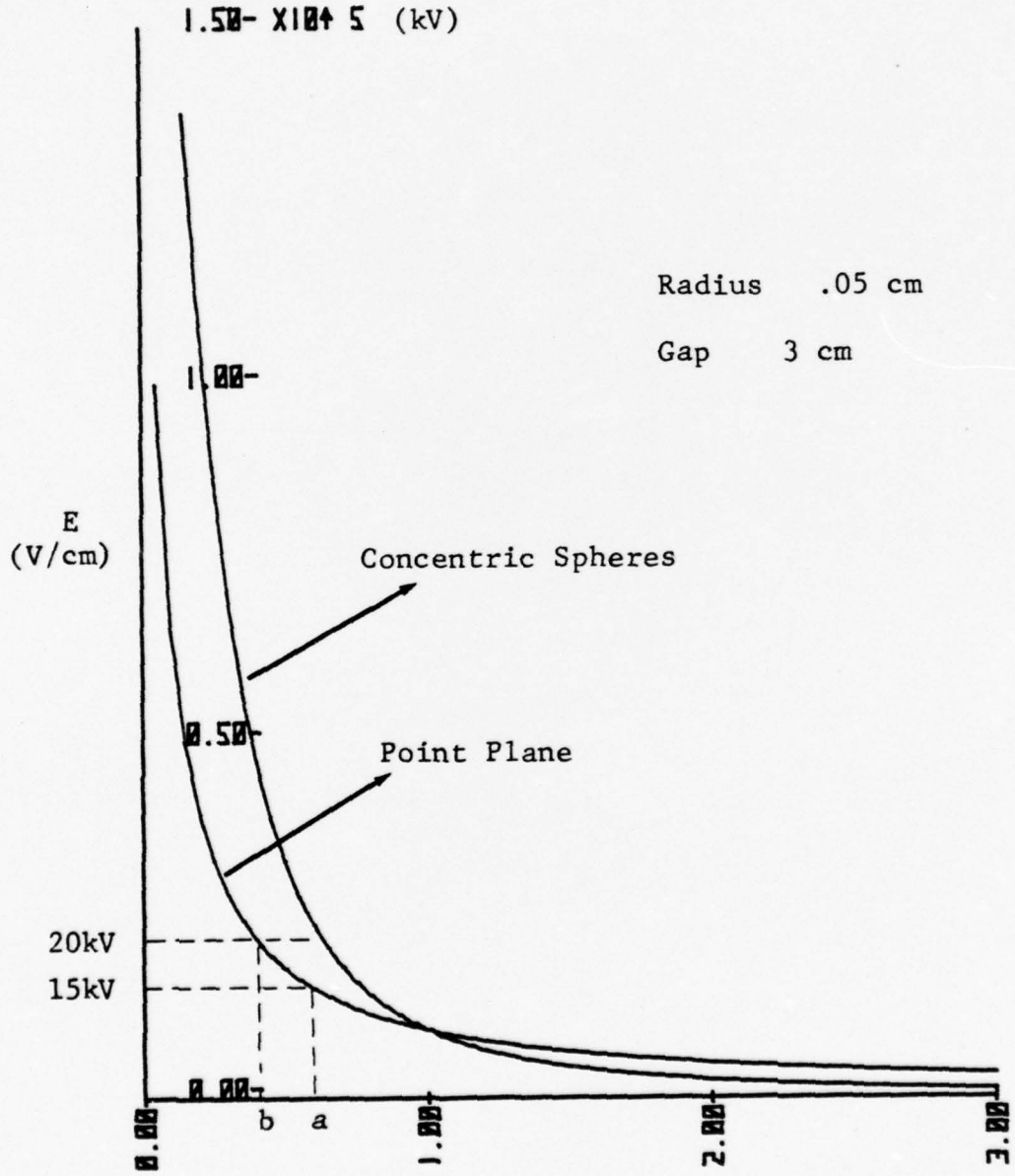


Figure 1. Sample Electric Field Distribution Curves for Hyperboloidal Point-Plane and Concentric Spheres.

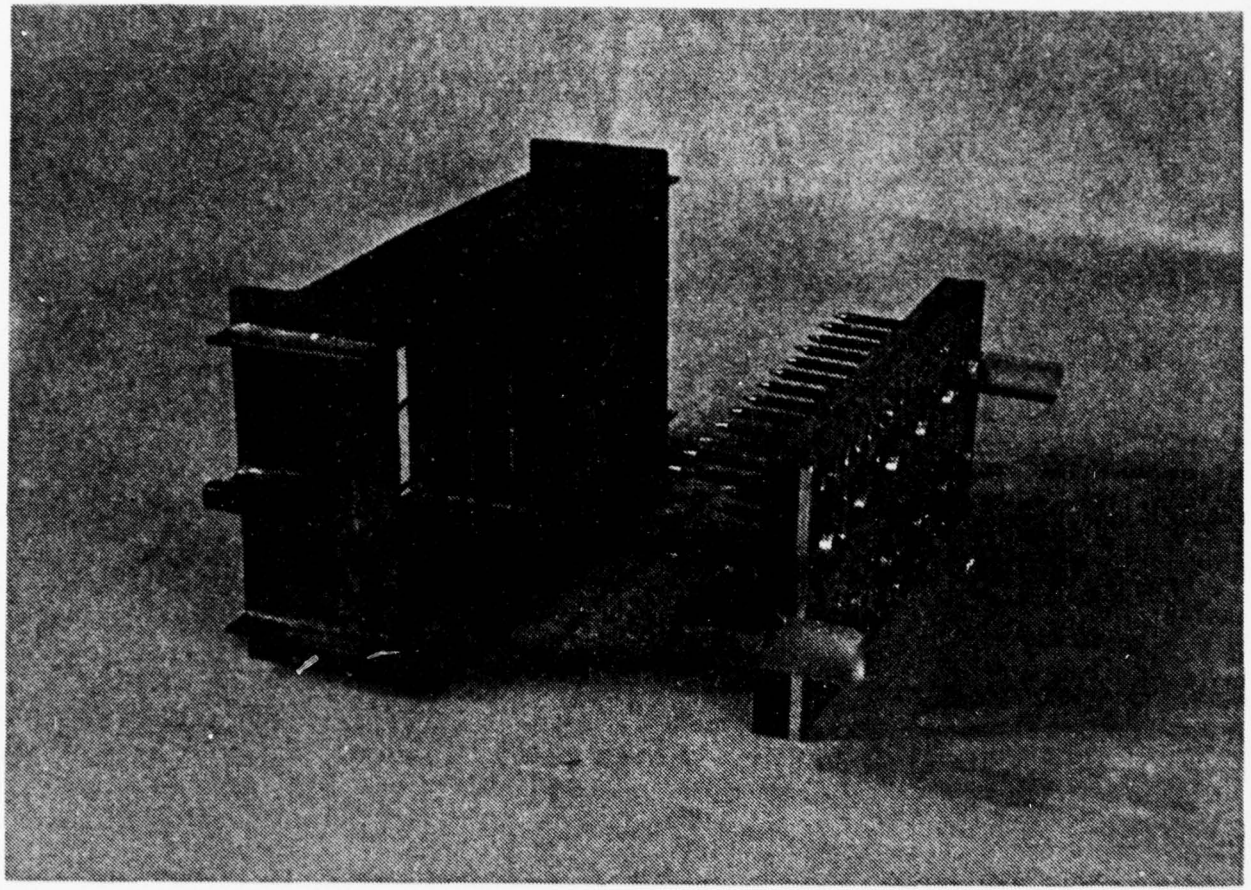


Figure 2. Final Electrode Arrangement. Modified Screen #9 Attached to Pins. Note: Screen and pin area $\doteq \frac{1}{2}$ total cross-sectional area of test section, resulting in high speed boundary layer flow. (See also Fig. 3d). Used with test section described in Ref. 3.

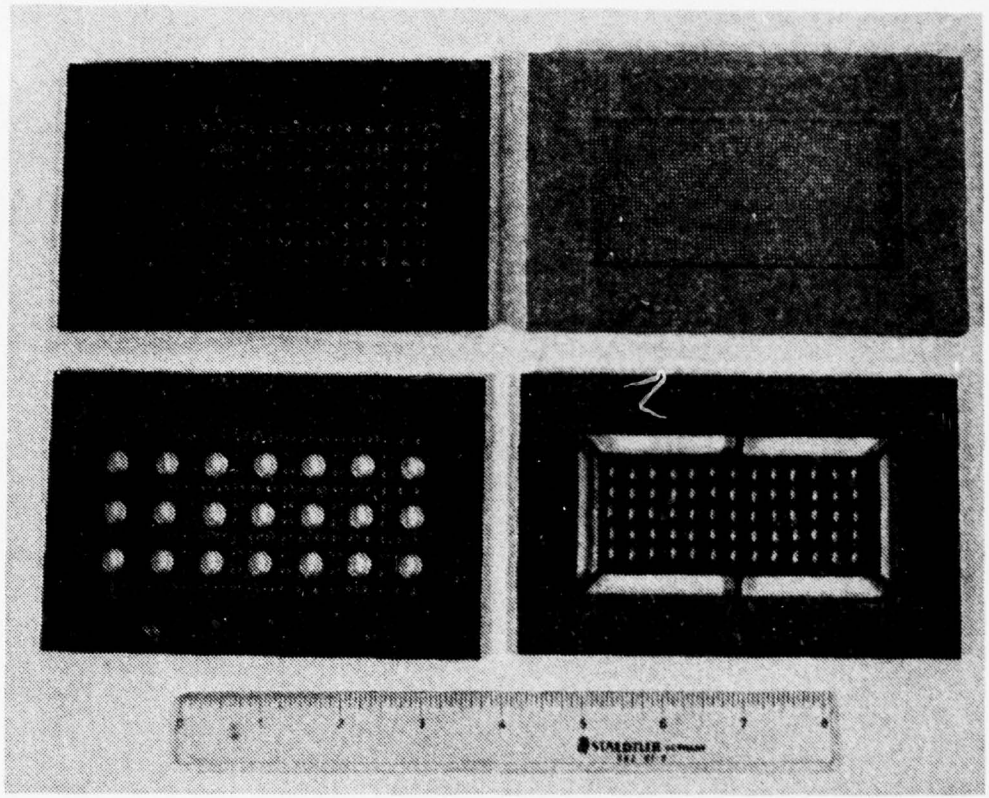


Figure 3. (a) Screen #6. (b) Screen #1. (c) Screen #9 (d) Boundary Layer Slot Screen. Used with test section of Ref. 6.

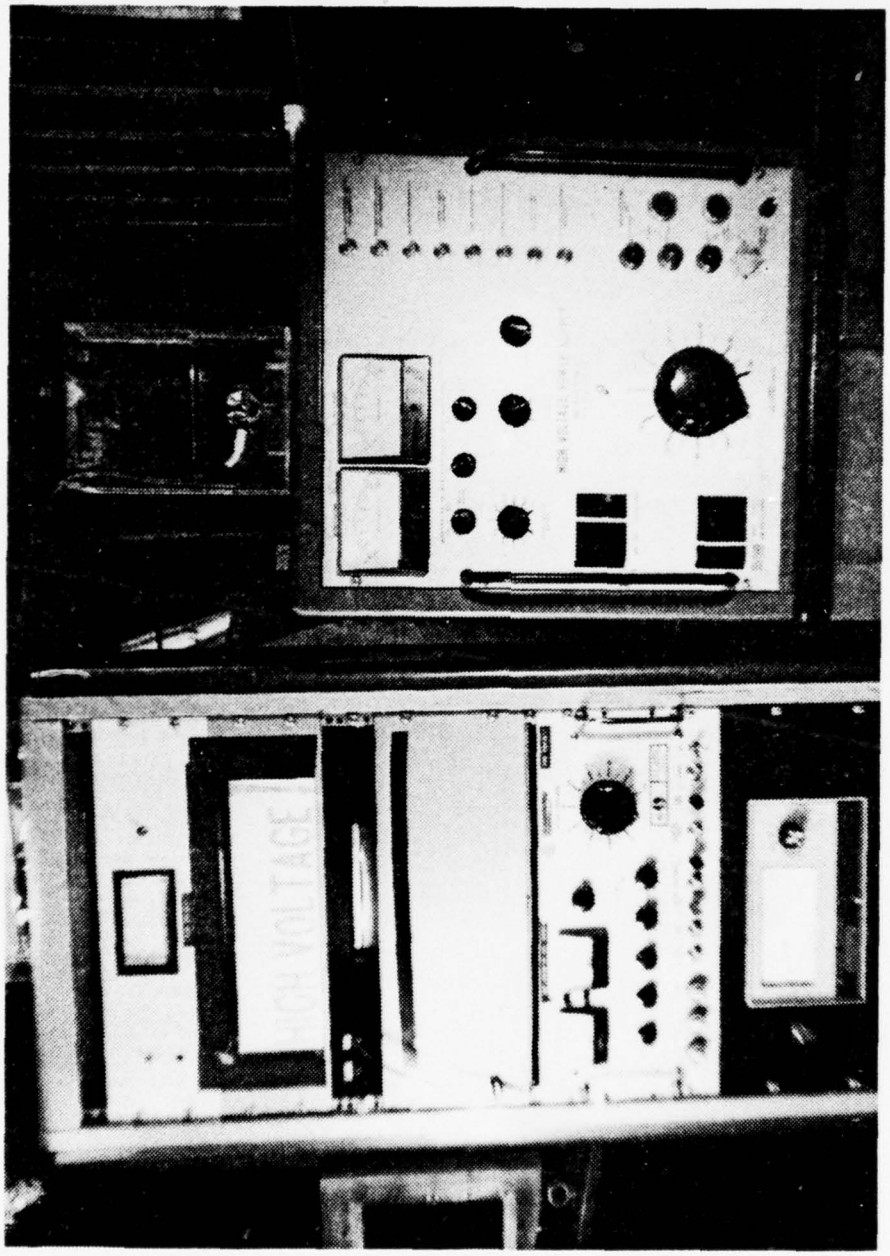


Figure 4. Power Supplies

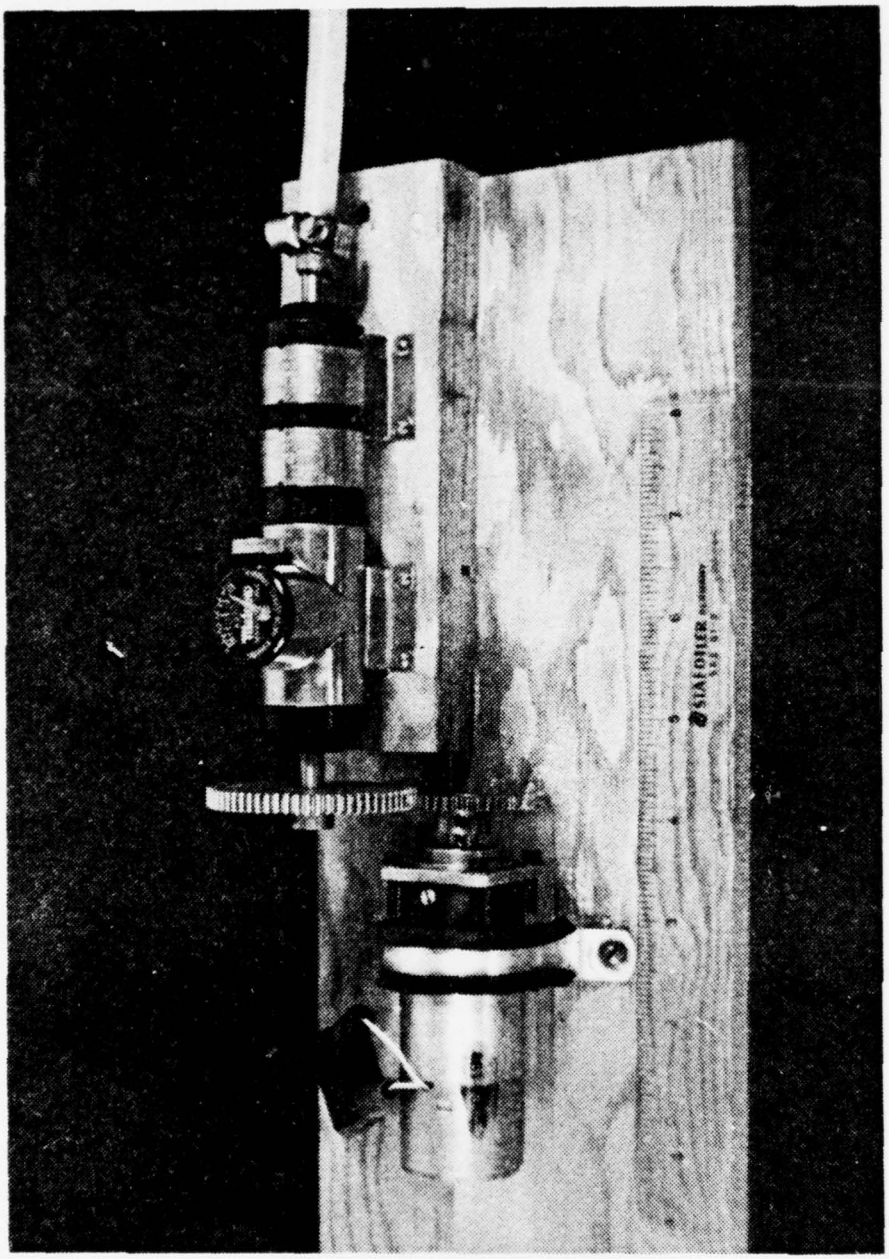


Figure 5. Variable Speed Transmission

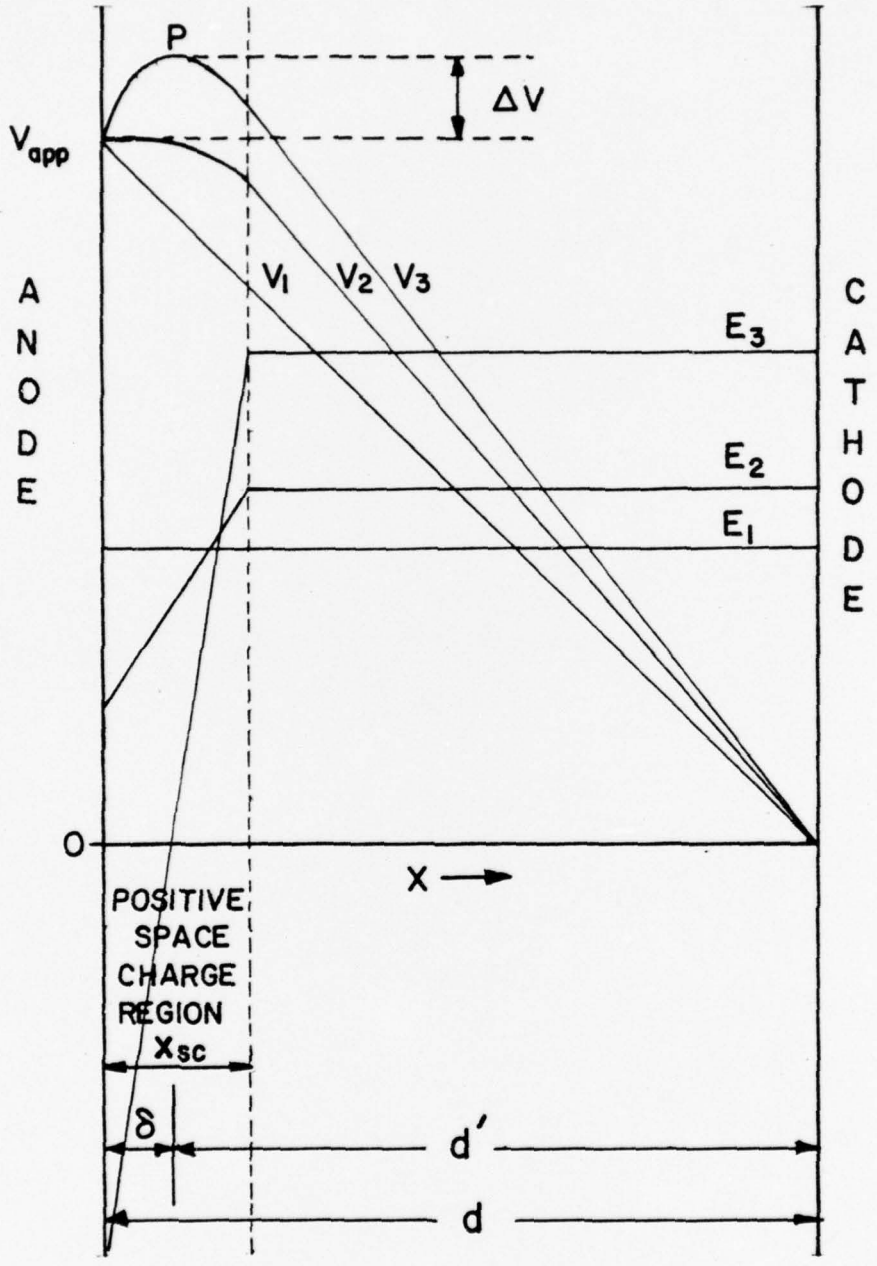


Figure 6. *Electric Field and Voltage Distribution between Parallel Plates.* Subscripts: (1) No Space Charge (2) Moderate Space Charge (3) High Space Charge

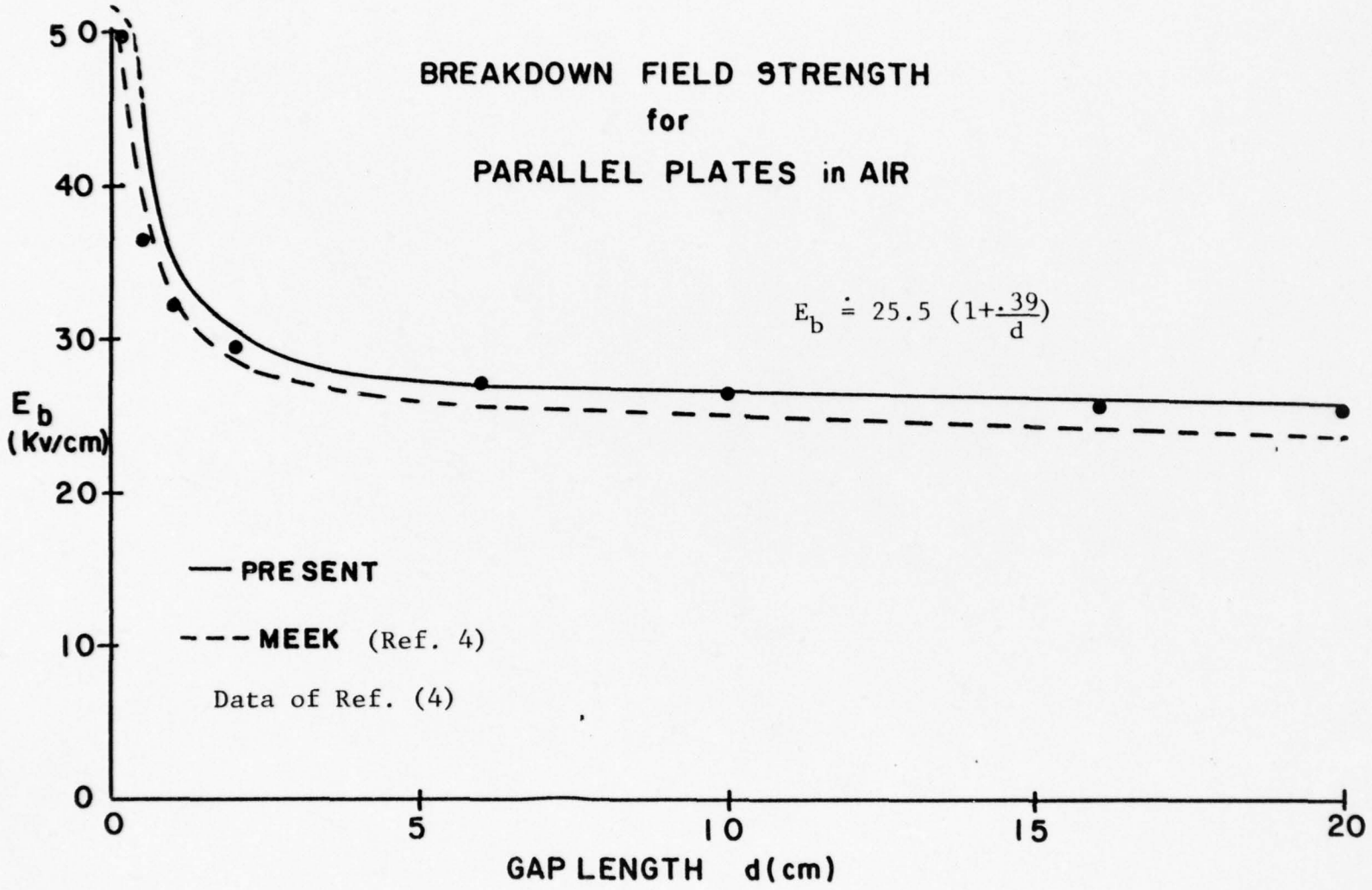


Figure 7. Measured and Calculated Values of E_b for Parallel Plates

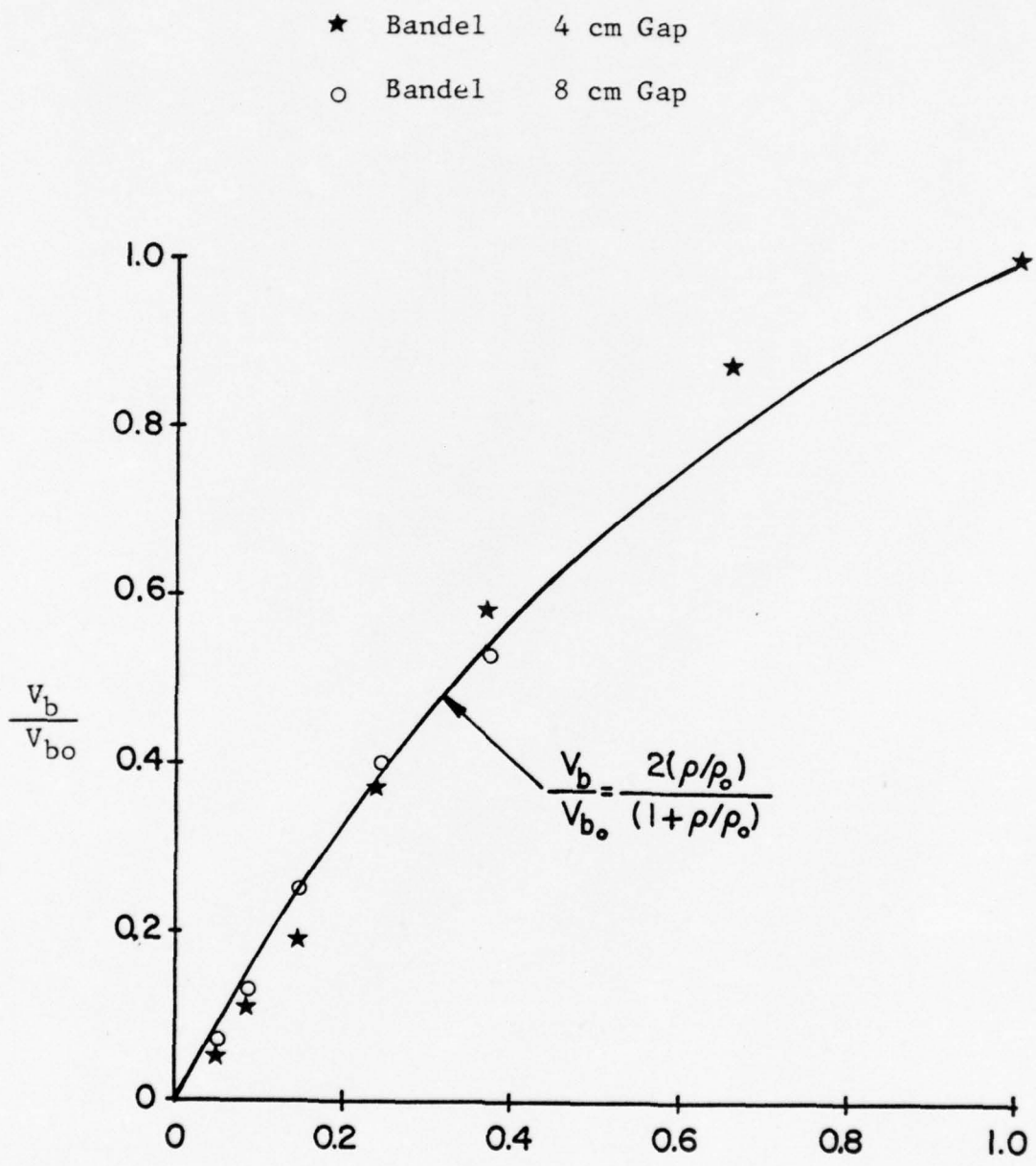
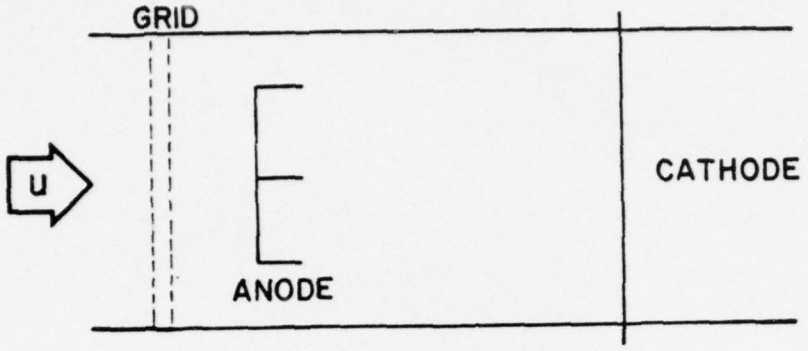
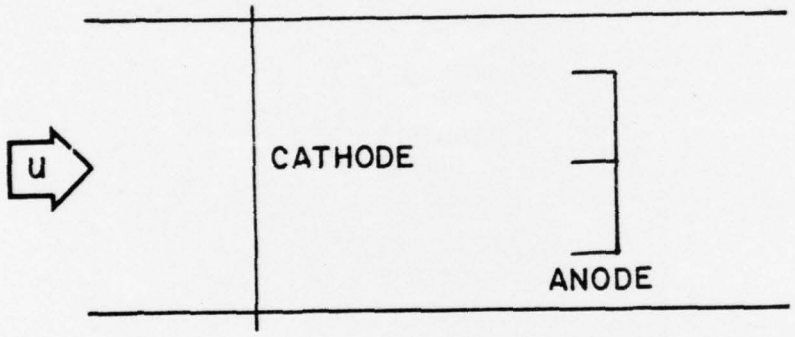


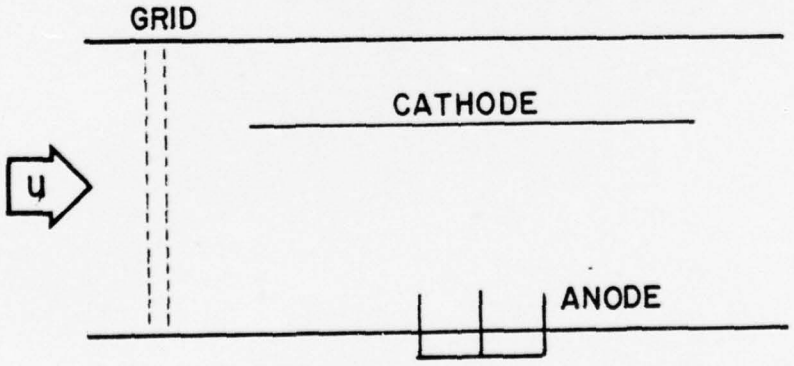
Figure 8. Predicted Model Breakdown Voltage Ratio Density Dependence vs. Actual Data.



(a) Ordinary Mode



(b) Reverse Flow



(c) Cross-Flow

Figure 9. Various Orientations of Electrodes and Turbulence Grids Tested.

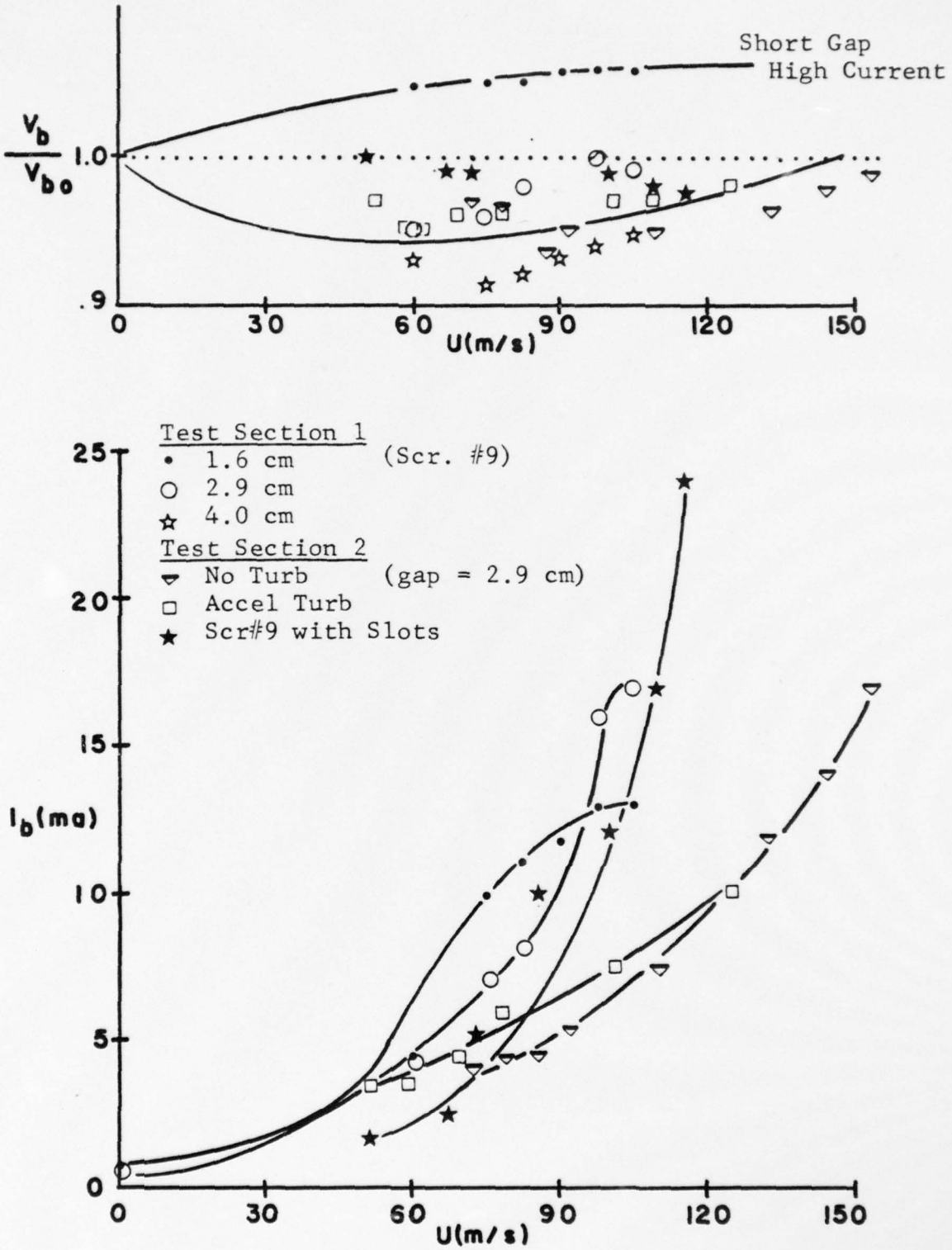


Figure 10. Voltage Ratio and Current vs. Velocity in the Ordinary Flow Mode.

CROSS FLOW

Symbol	Gap (cm)	Turbulence
●	3.2	No Grid
★	3.0	No Grid
◇	3.0	Scr # 9
△	3.0	Bdry Layer Slot Scr
○	1.4	Bdry Layer Slot Scr
□	1.4	No Grid
▽	1.4	No Grid

REVERSE FLOW

☆	3.9	No Grid

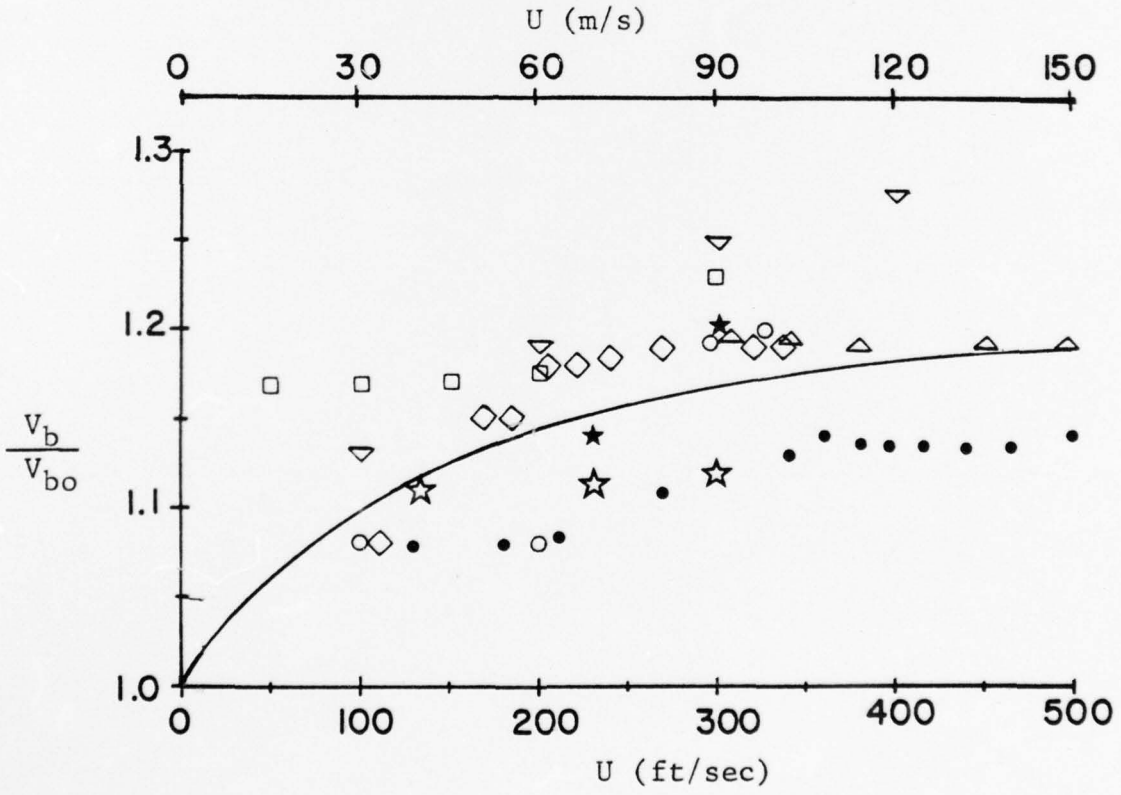


Figure 11. Voltage Ratio vs. Velocity in Reverse and Cross-Flow Modes.

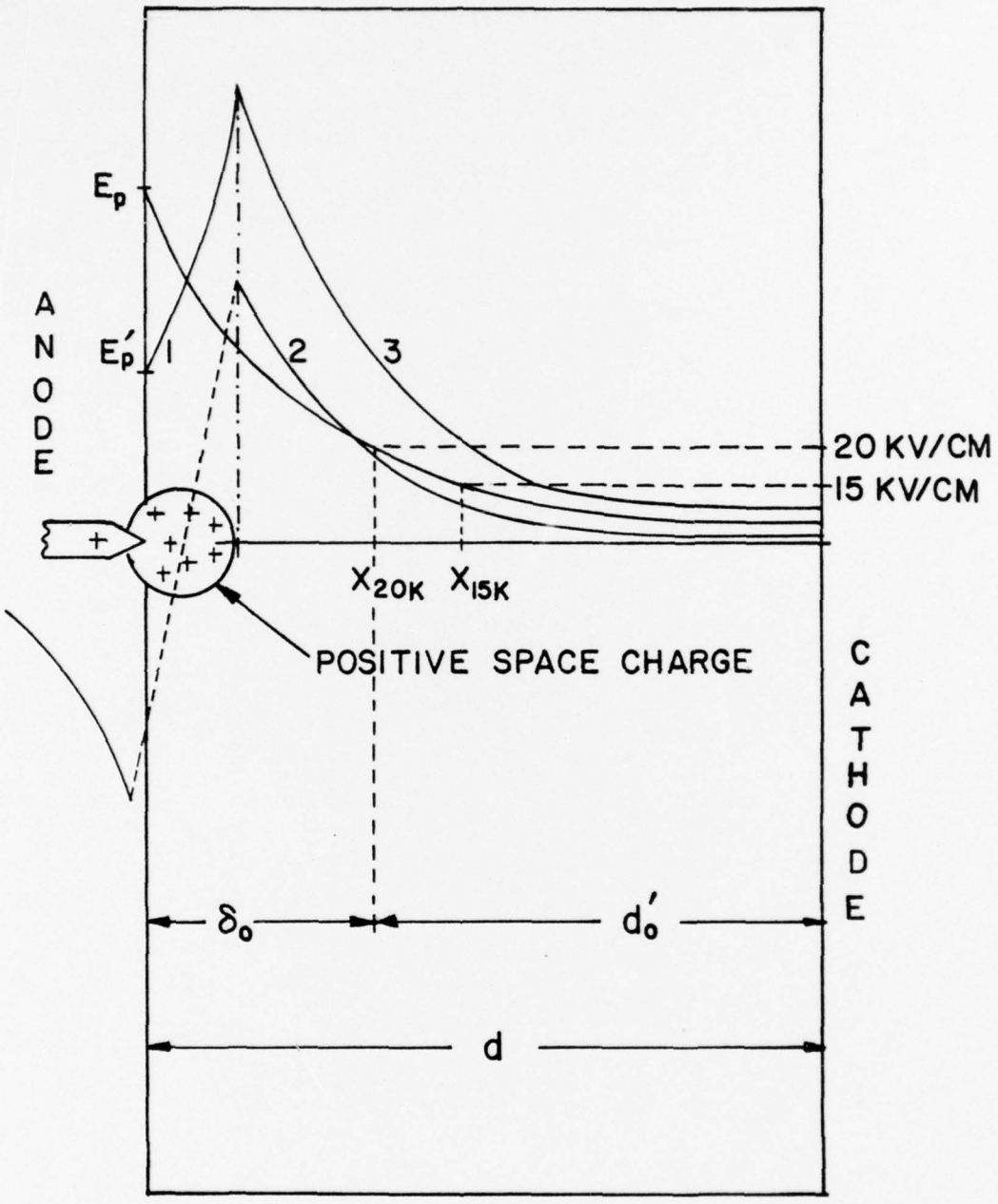


Figure 12. Electric Field Distribution in a Point-Plane Gap. Curves: (1) Point Field Only (2) Space Charge Only (3) Total Field

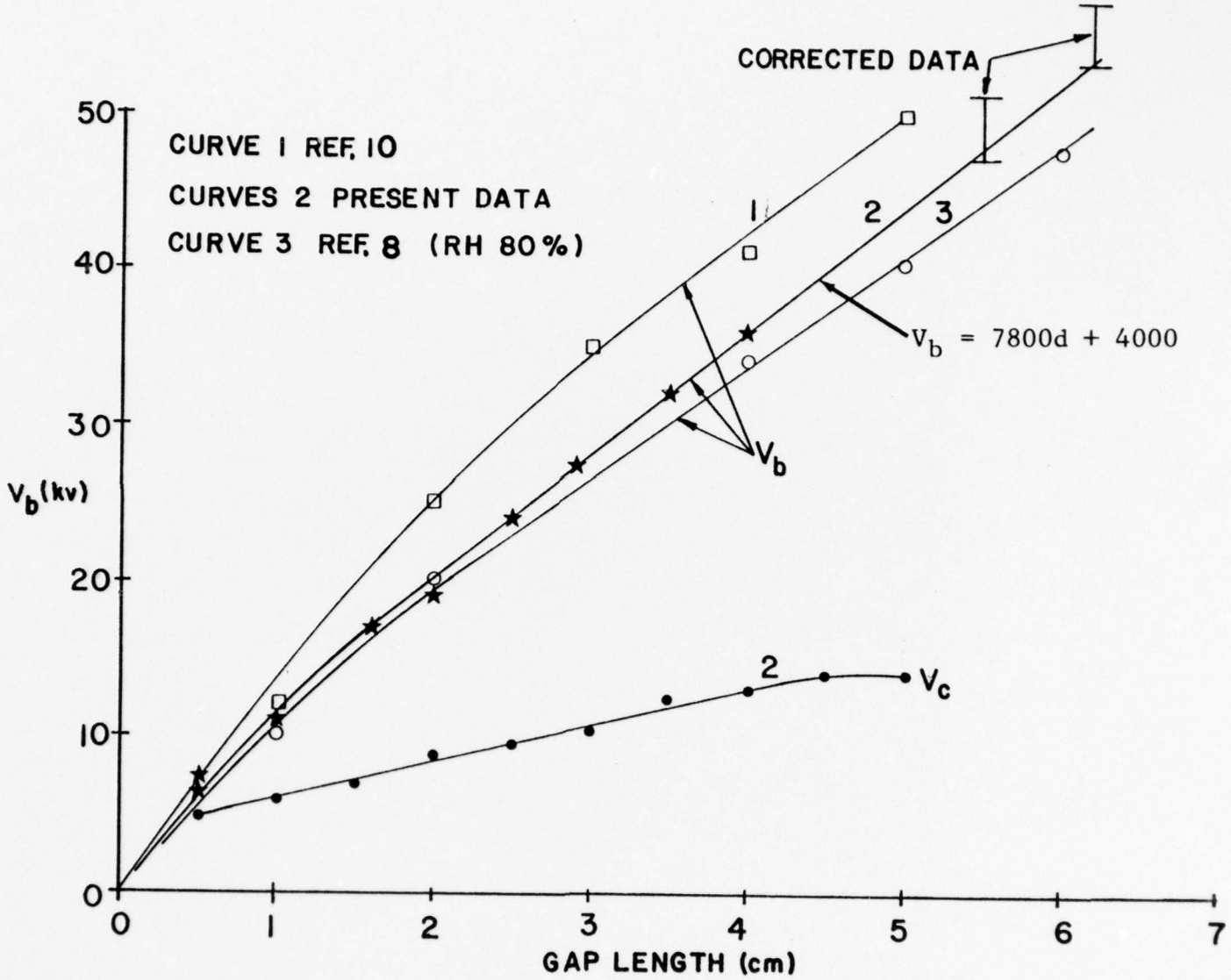


Figure 13. Breakdown and Corona Initiation Voltage vs. Gap Length for No-Flow at Atmospheric Pressure.

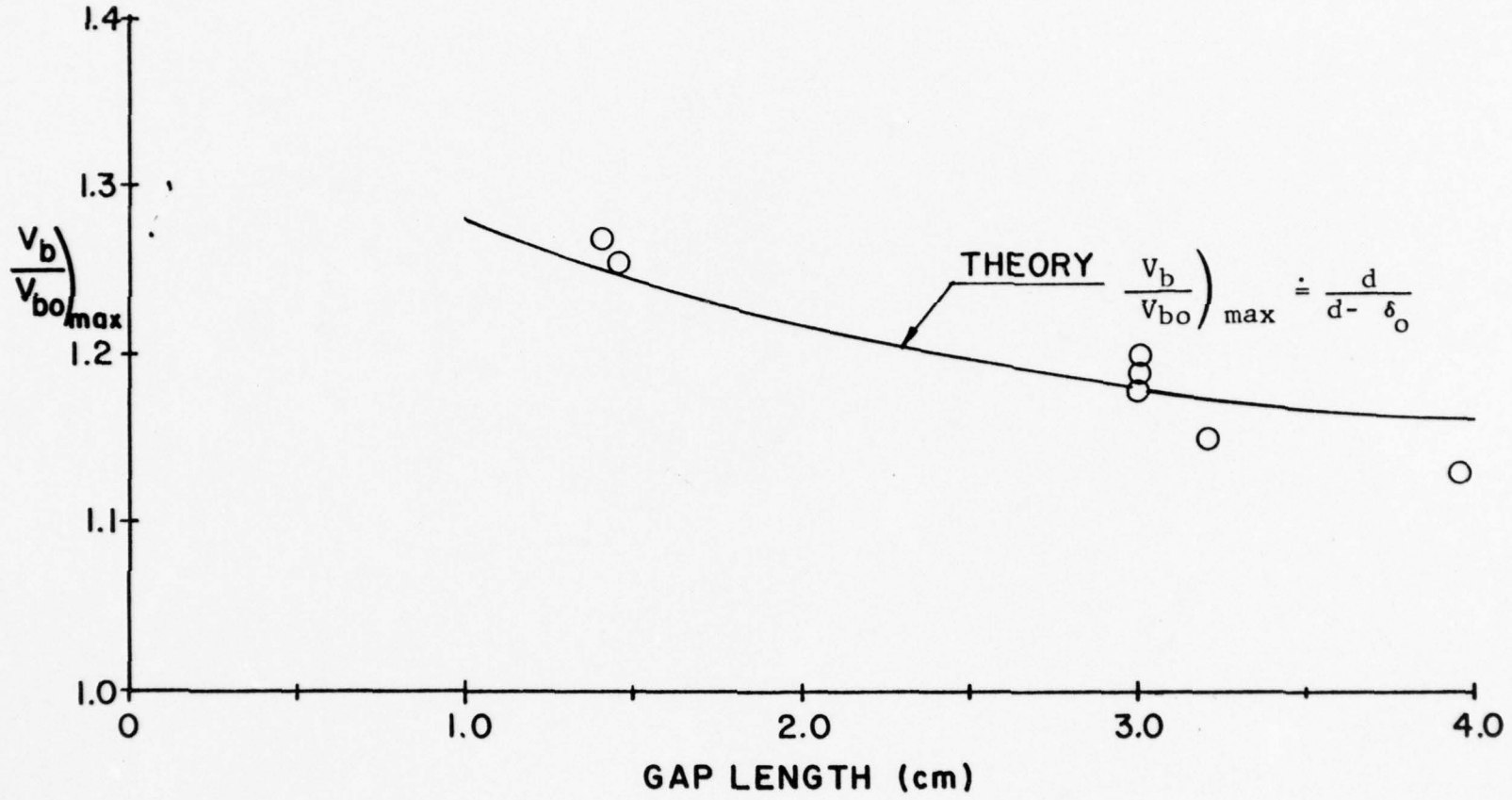


Figure 14. Summary of Maximum Breakdown Voltage Ratio vs. Gap Length

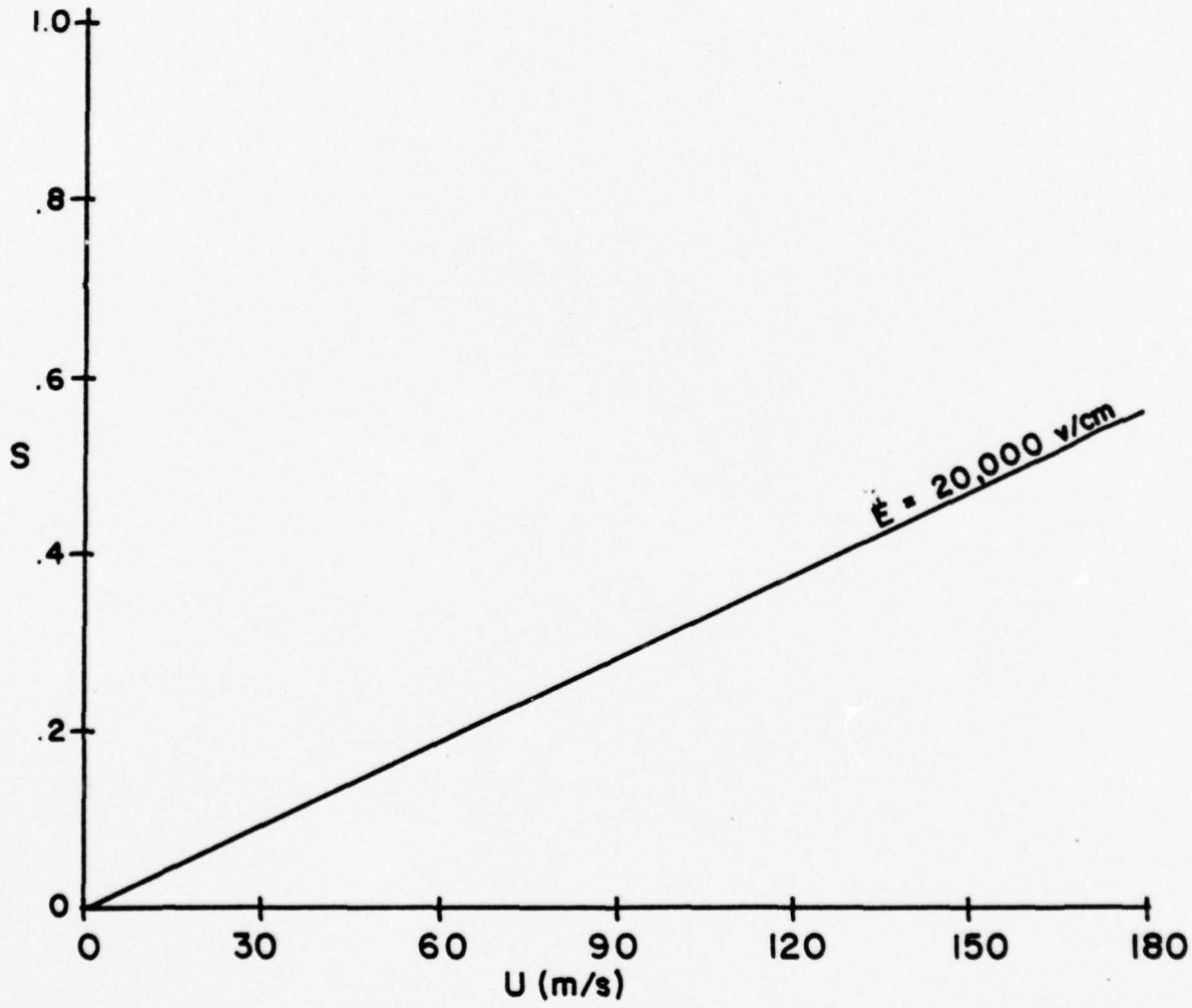


Figure 15. Calculated Values of the Slip Parameter at the Field Point E = 20,000 volts/cm.

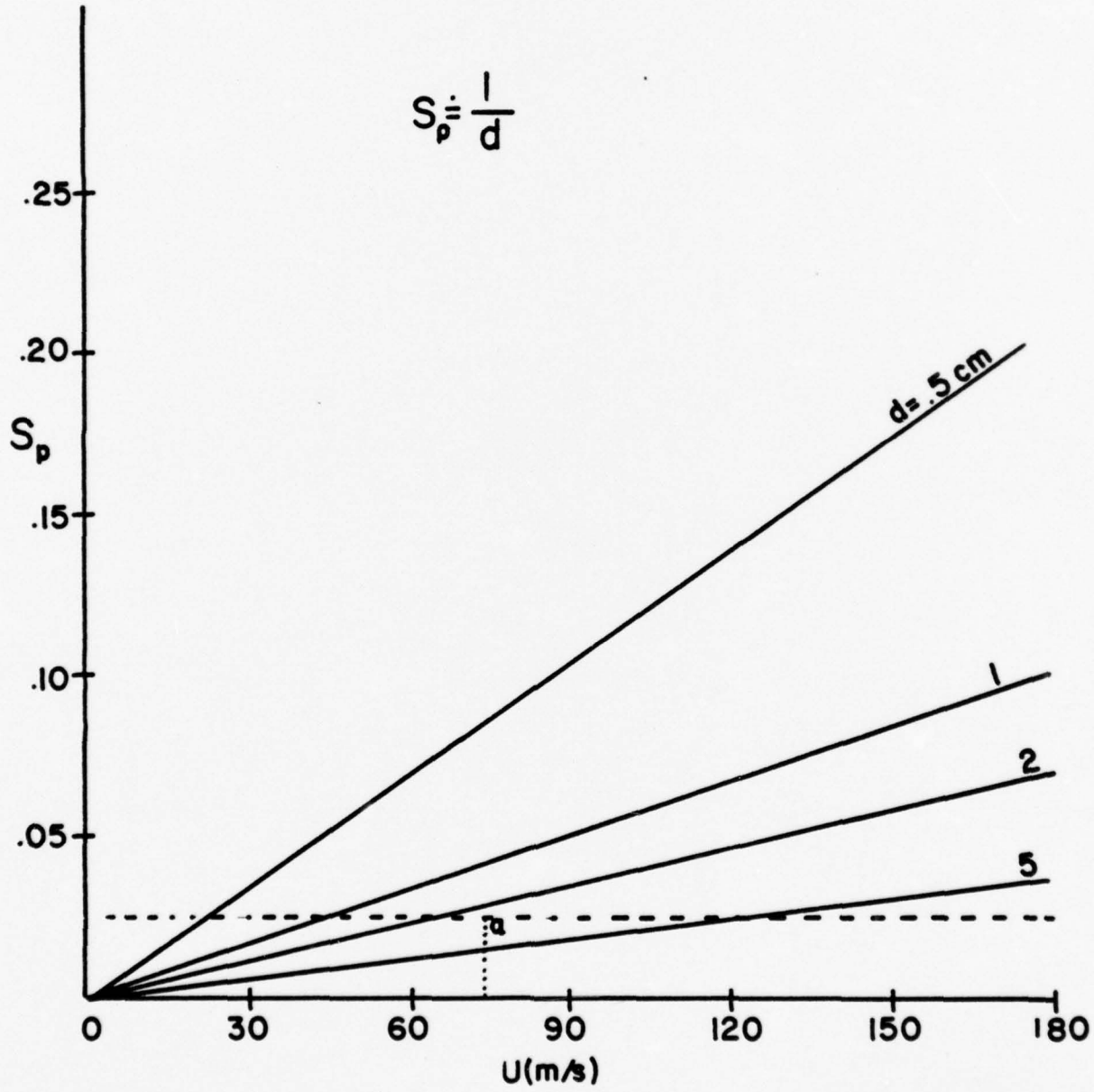


Figure 16. Calculated Values of Slip Parameter at Anode Surface. Note that $S_p = f(d)$.

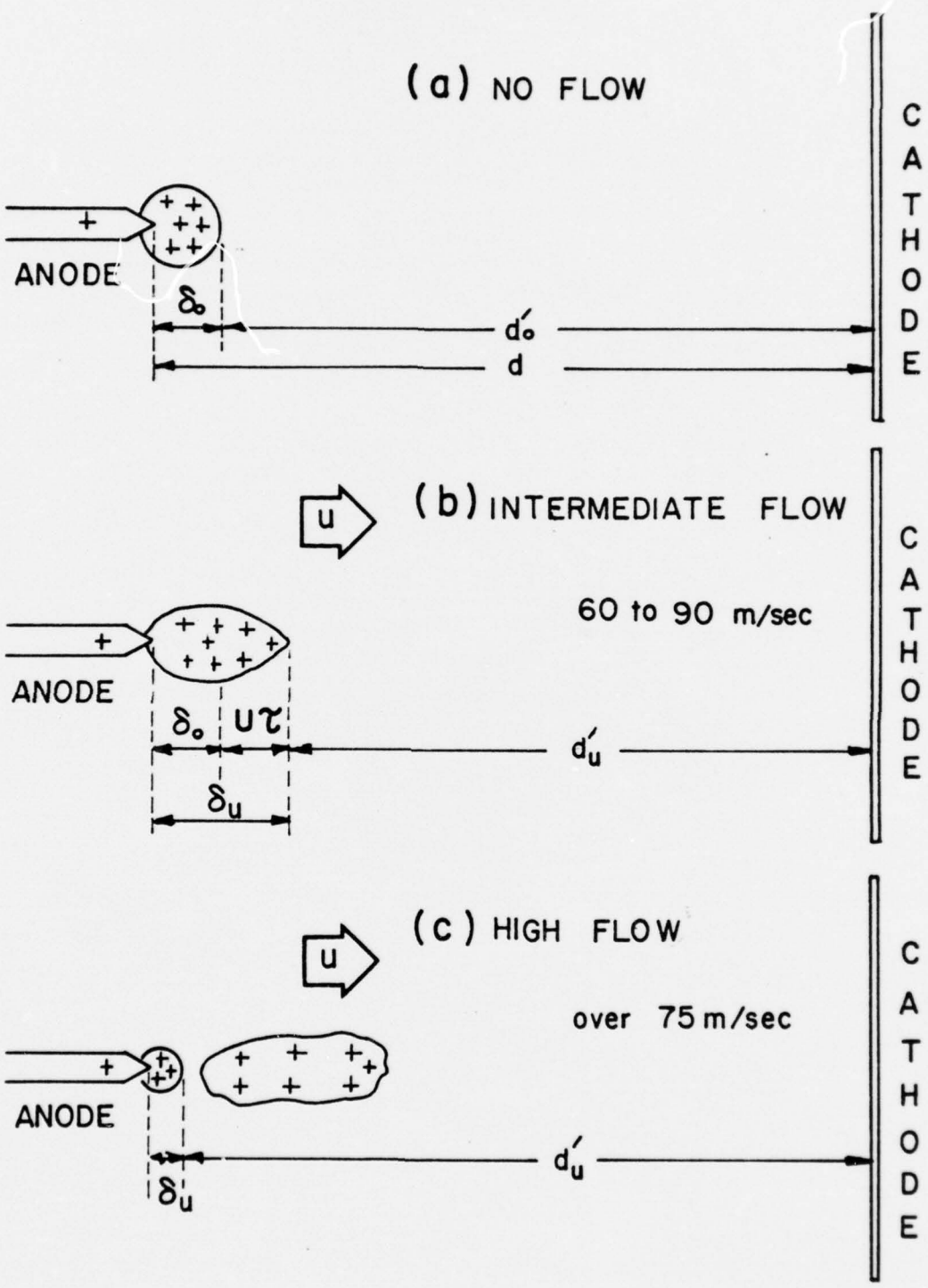


Figure 17. Various Stages of Anode Extension and "Blowout"

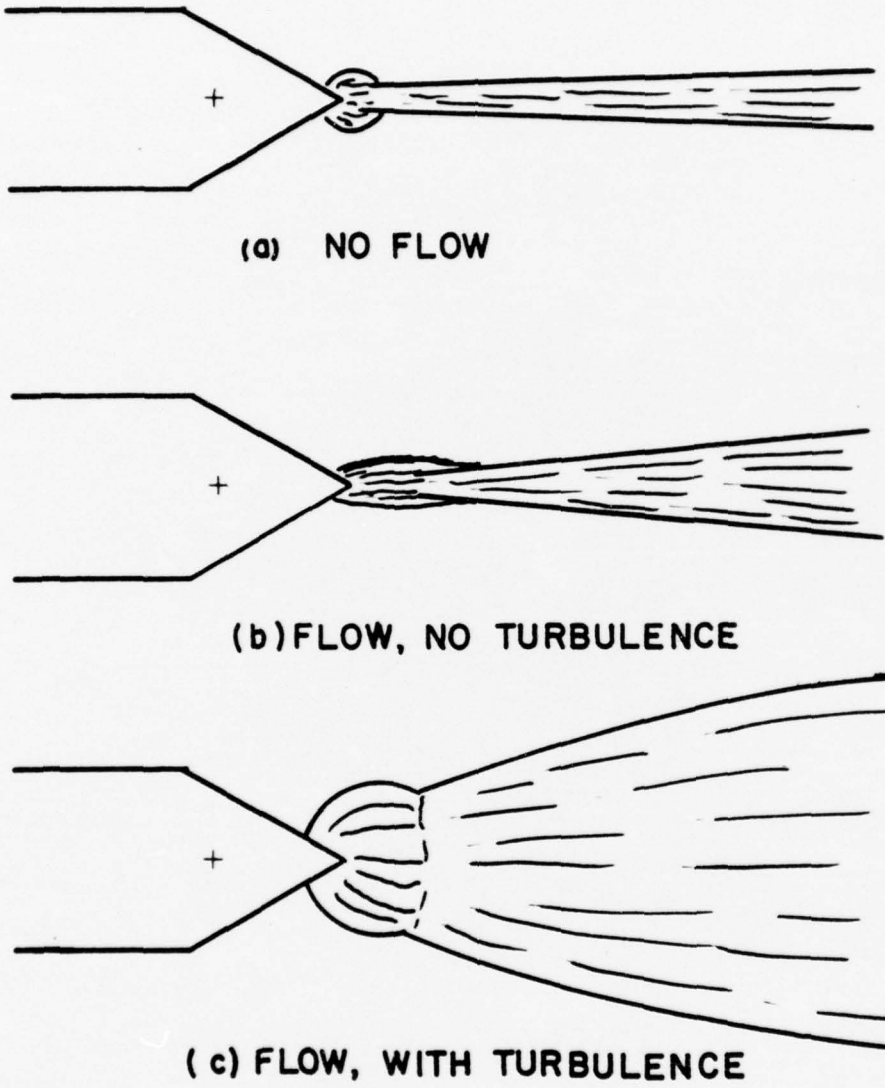


Figure 18. Visual Character of Various Glow Modes without Diffuser

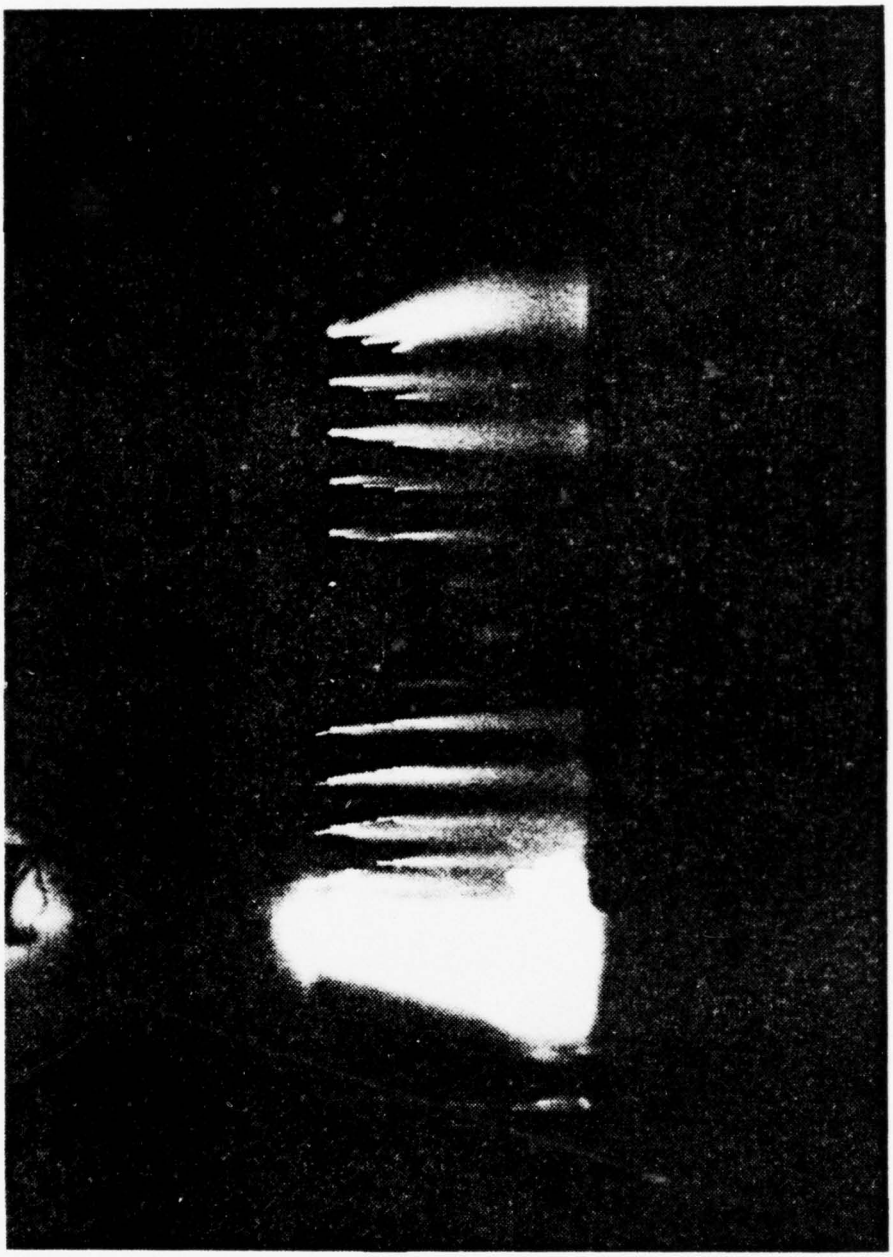
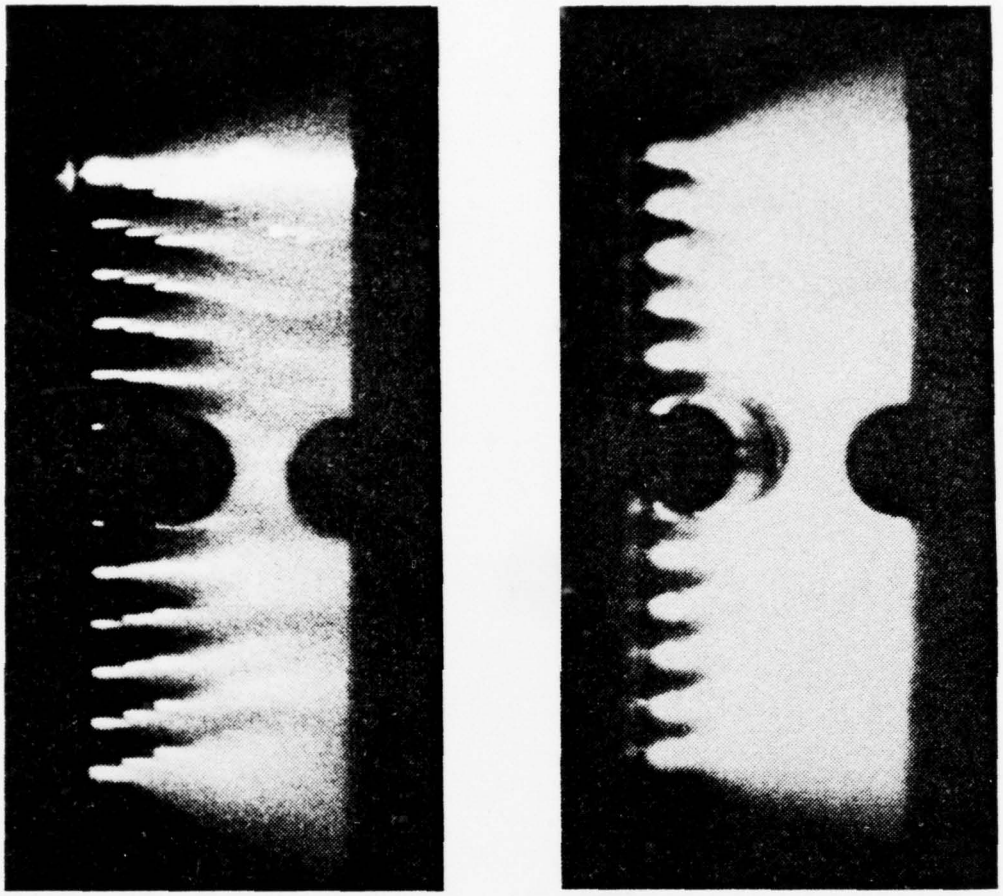


Figure 19. Photograph of Discharge. No Flow (10 sec exposure). Pins on Left. Bright region on bottom is an arc which took place during timed exposure. Note small spherical tip glow region.



(a)

Flow, No Turbulence

(b)

Flow, With Turbulence

Figure 20. Pins on Left. Ordinary flow from left to right (1 sec exposures). Note elongation of glow region in (a) due to convection ($u \doteq 150$ m/sec), and very homogeneous spreading of glow in (b) due to high turbulence.

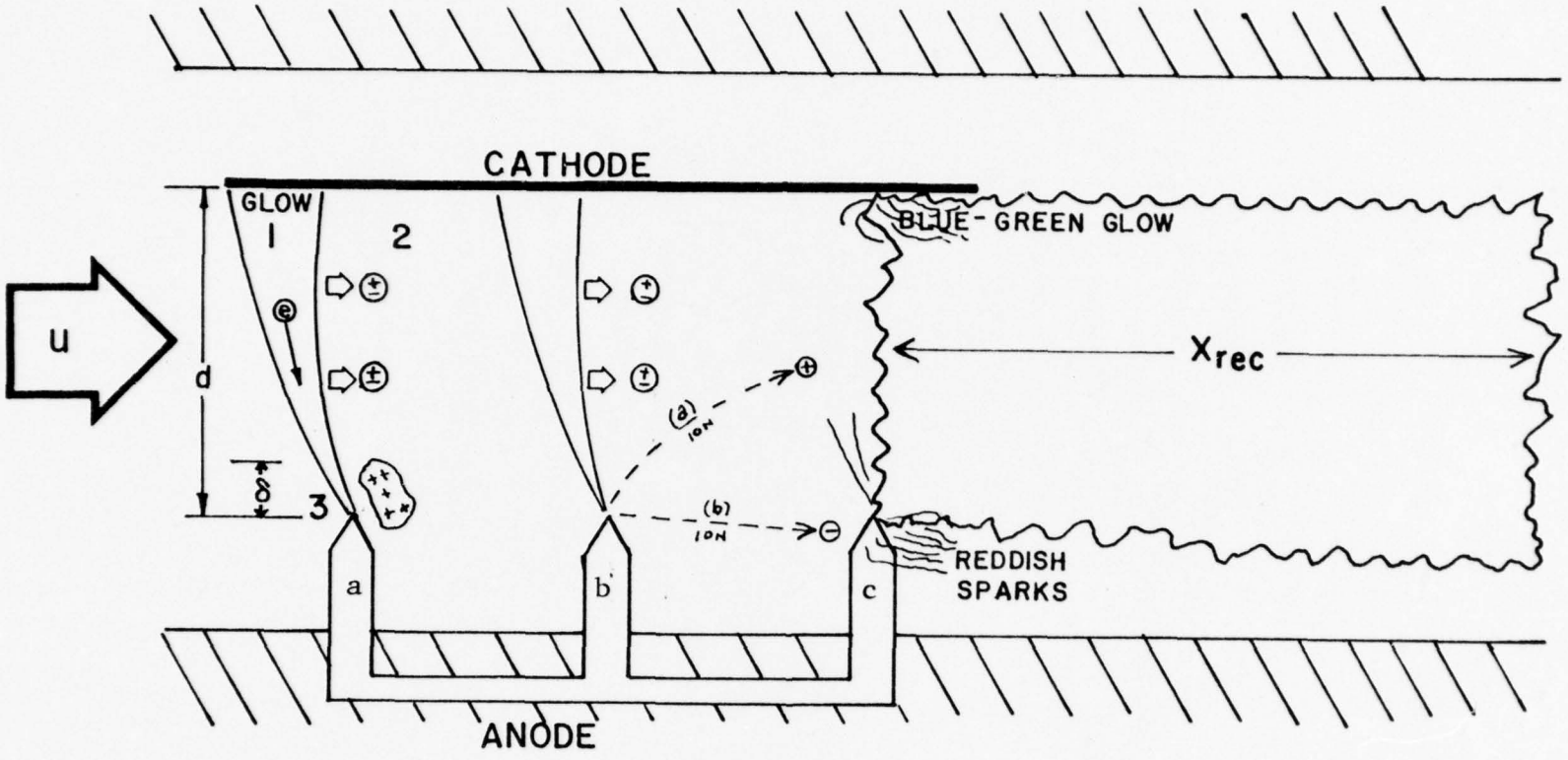


Figure 21. Schematic Representation of Cross-Flow Current Distribution (Observations).

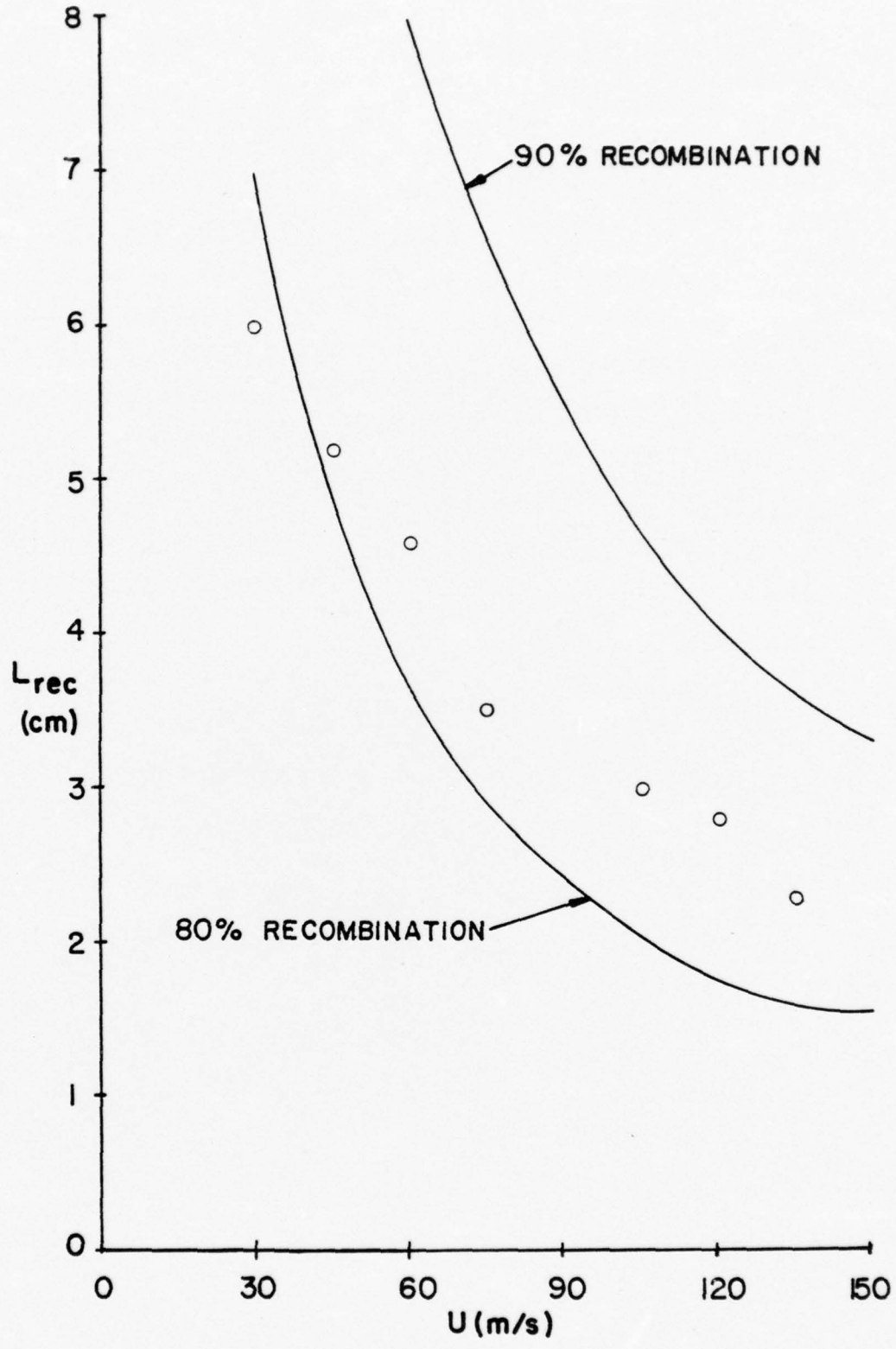


Figure 22. Calculated and Measured Recombination Lengths in the Cross-Flow Mode.

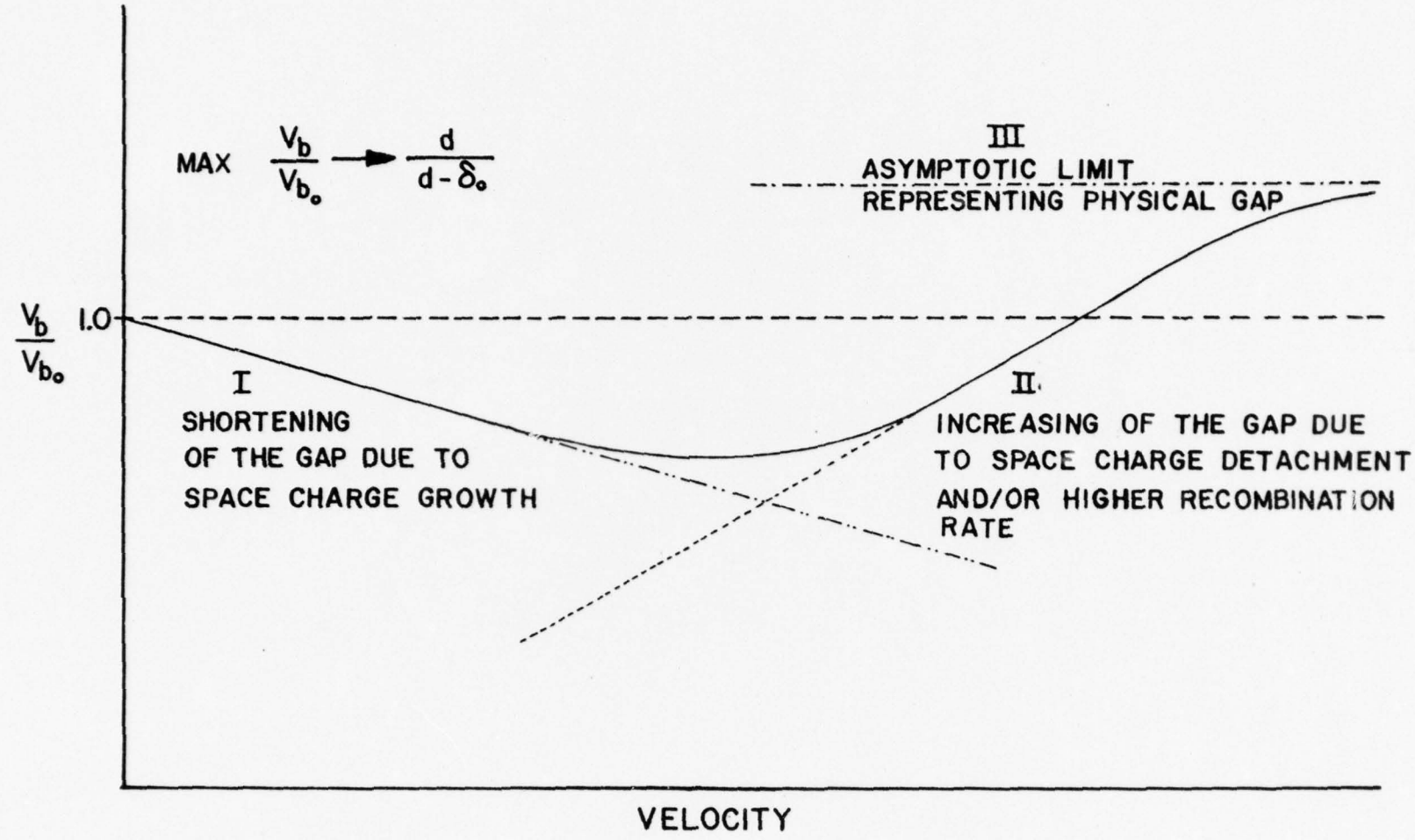


Figure 23. General Breakdown Voltage Characteristics as Predicted by Model for Ordinary Flow Mode.

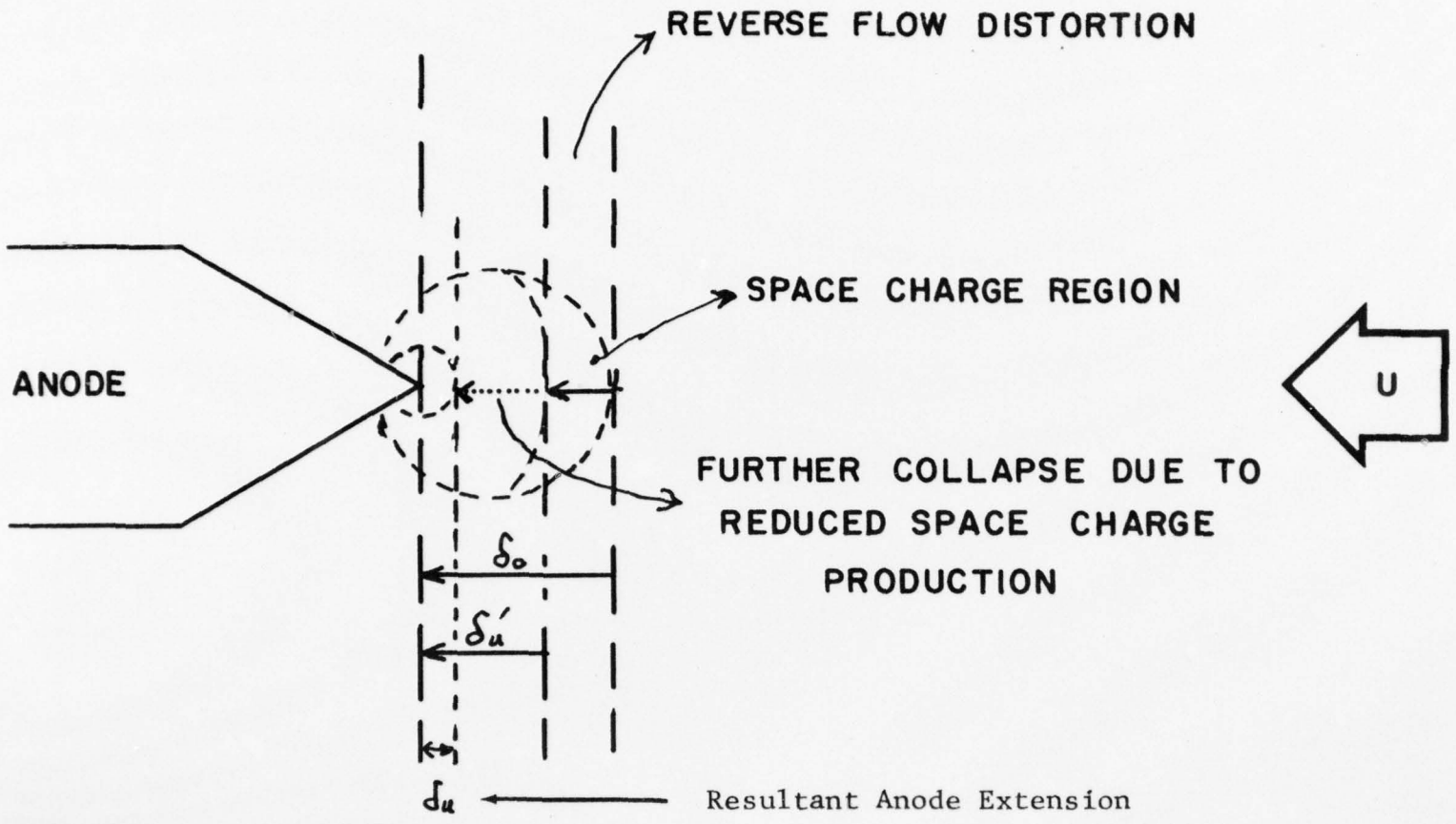
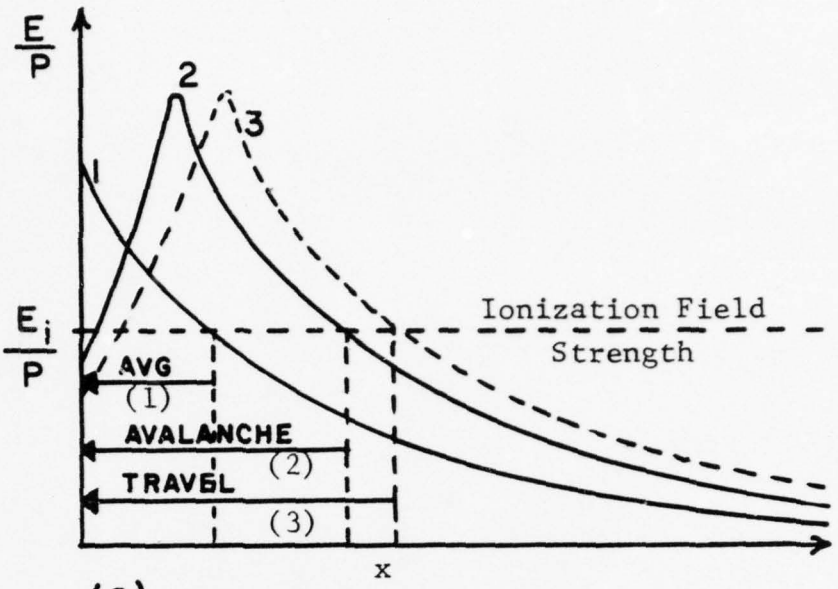
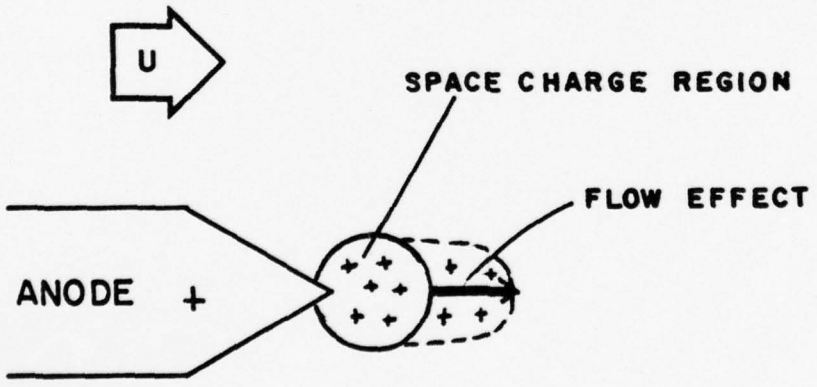


Figure 24. Space Charge Collapse in Reverse Flow Mode.



(a) Electric Field
(1) No Space Charge
(2) With Space Charge, No Flow
(3) With Space Charge, and Flow



(b) Schematic of Flow Effect on Space Charge

Figure 25. Convection Effects on Average Electron Avalanche Travel Distance

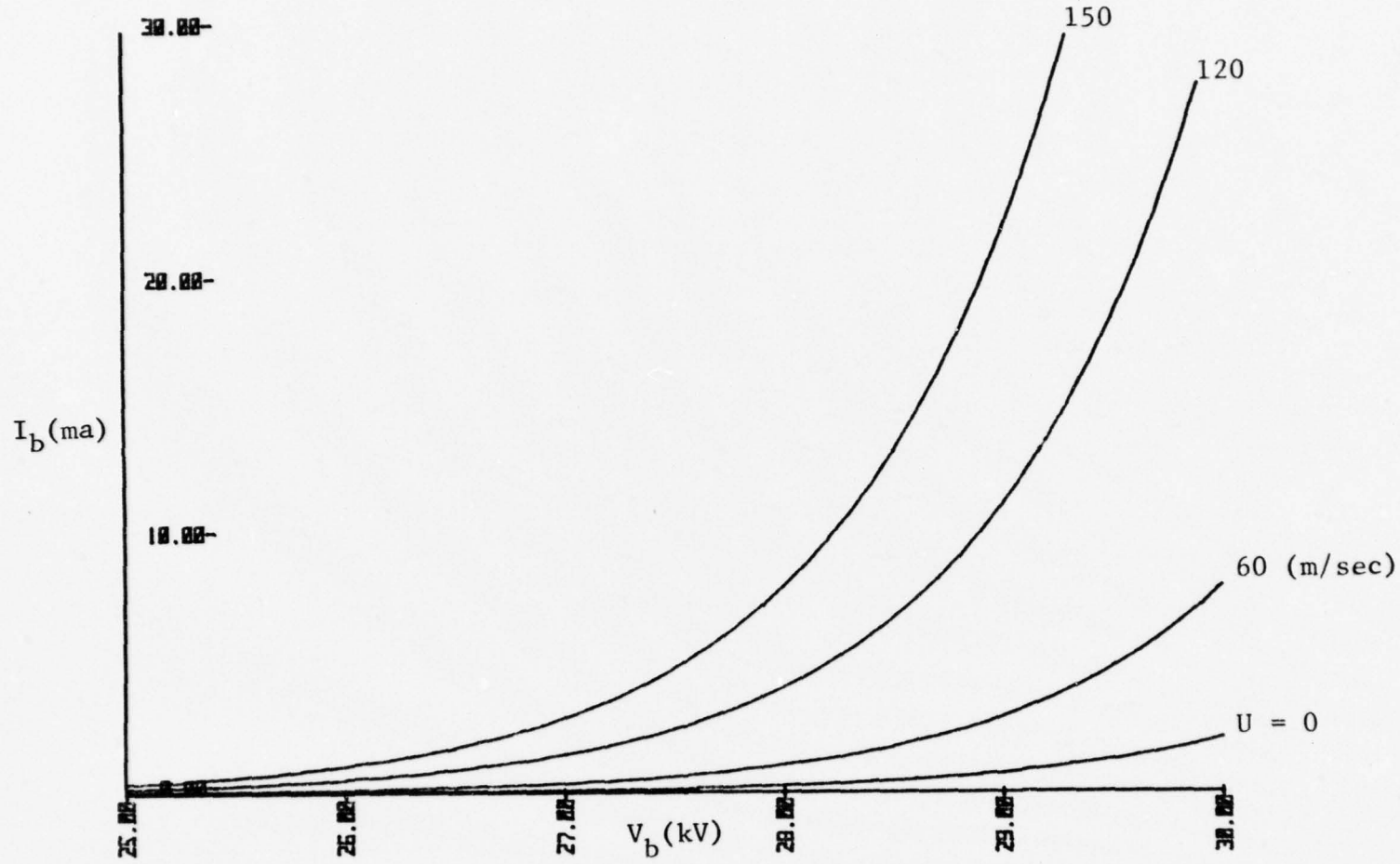


Figure 26. I-V Characteristic Velocity Dependence from Eq. (44)

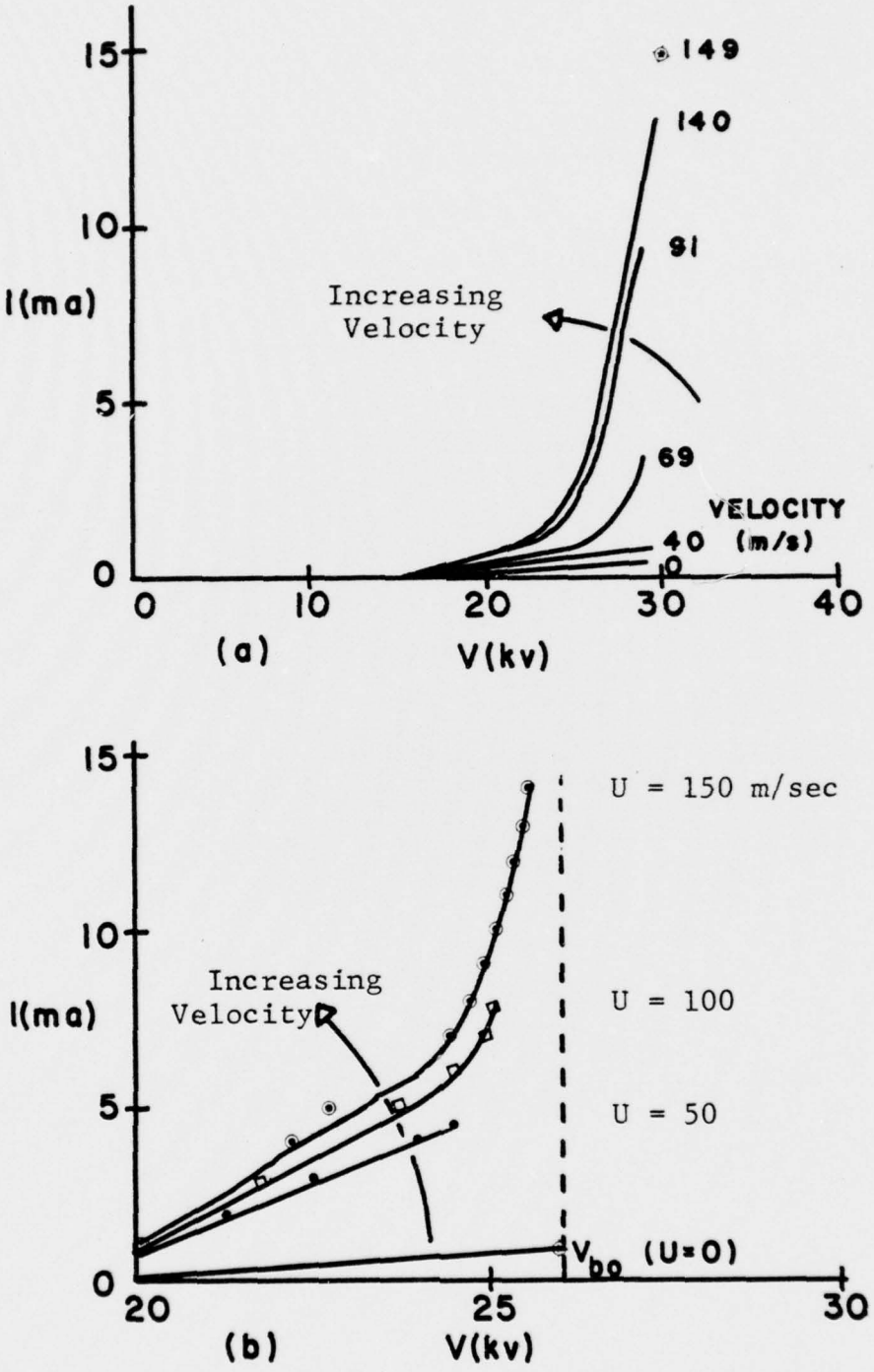


Figure 27. Convection and Velocity Effects on I-V Characteristics. (a) 3 cm gap, with Turbulence. (b) 2.9 cm gap, no Turbulence.

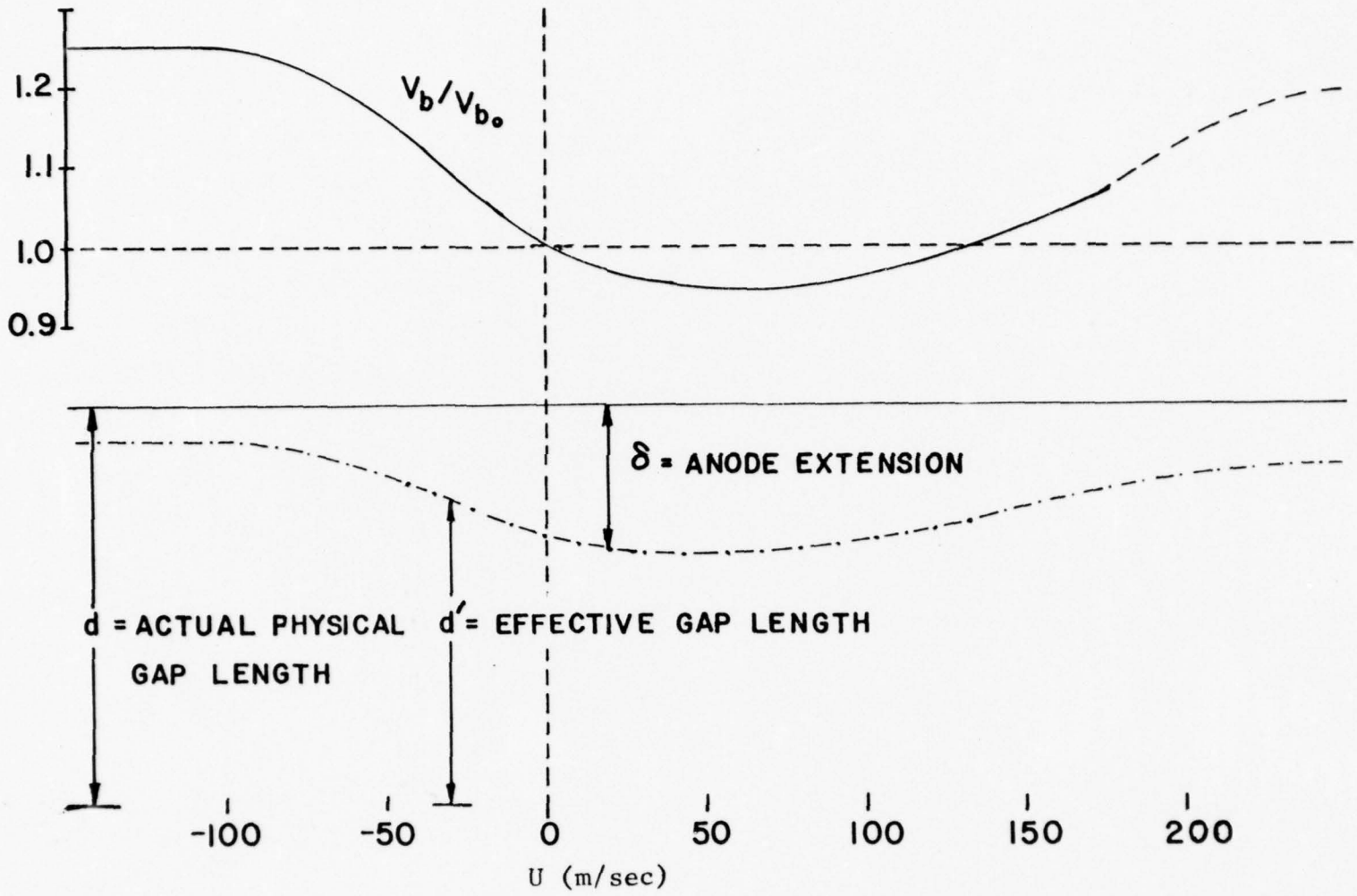


Figure 28. Summary of Flow Effects on Breakdown Voltage with Representation of Pertinent Model Parameters.

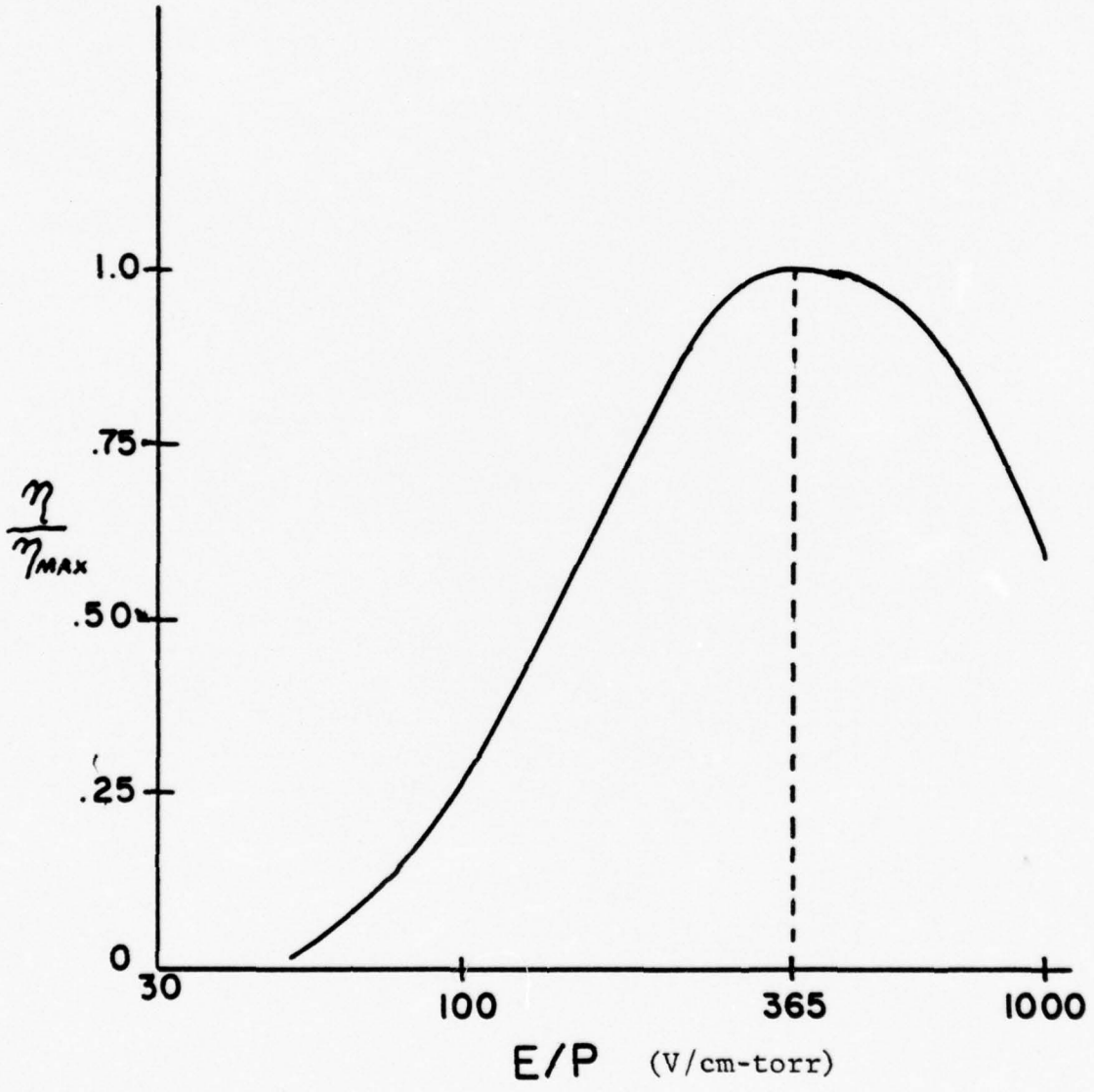


Figure 29. Relative Ionization Efficiency of Air vs. Reduced Pressure. (From Ref. 4)

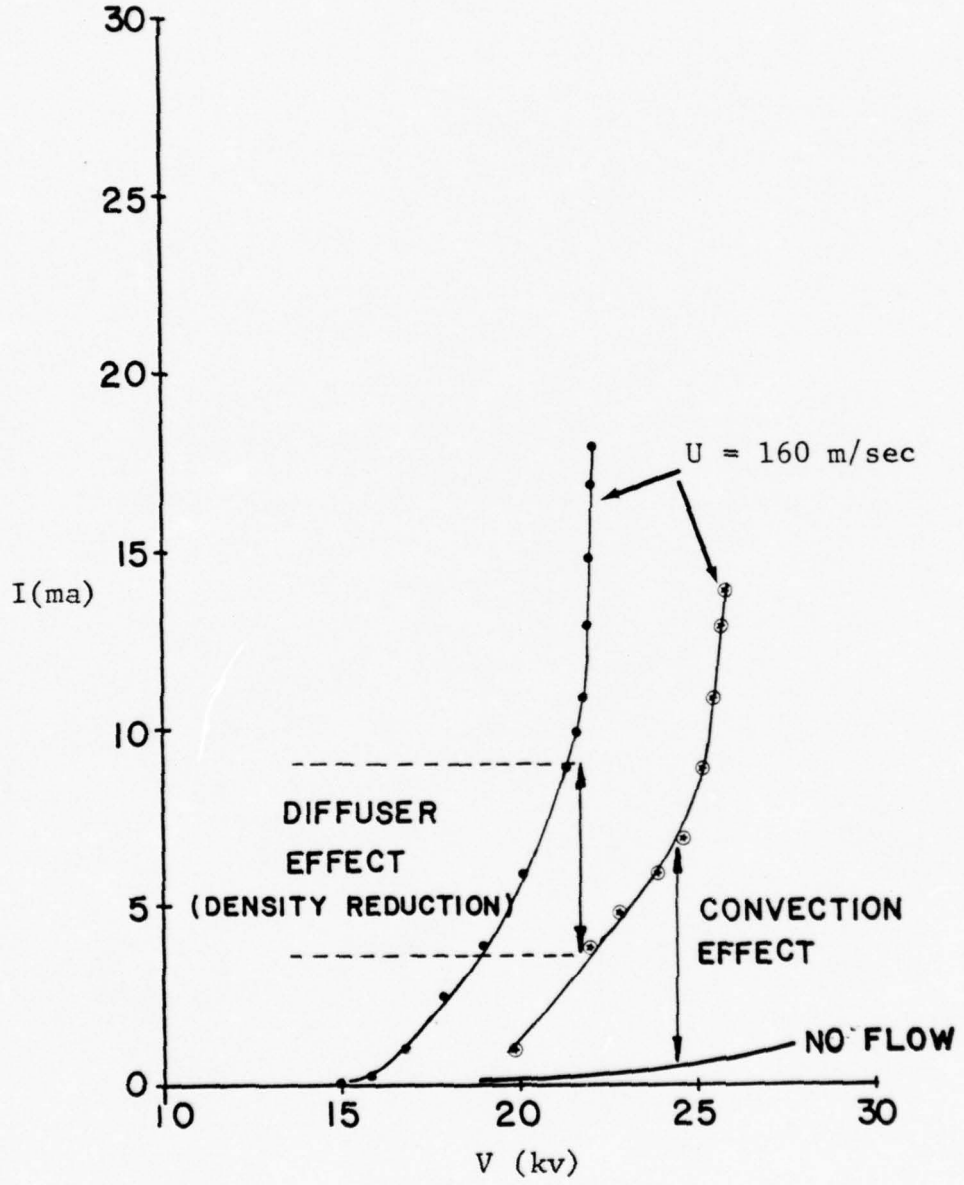


Figure 30. Typical Observed I-V Shift due to Diffuser Induced Density Reduction

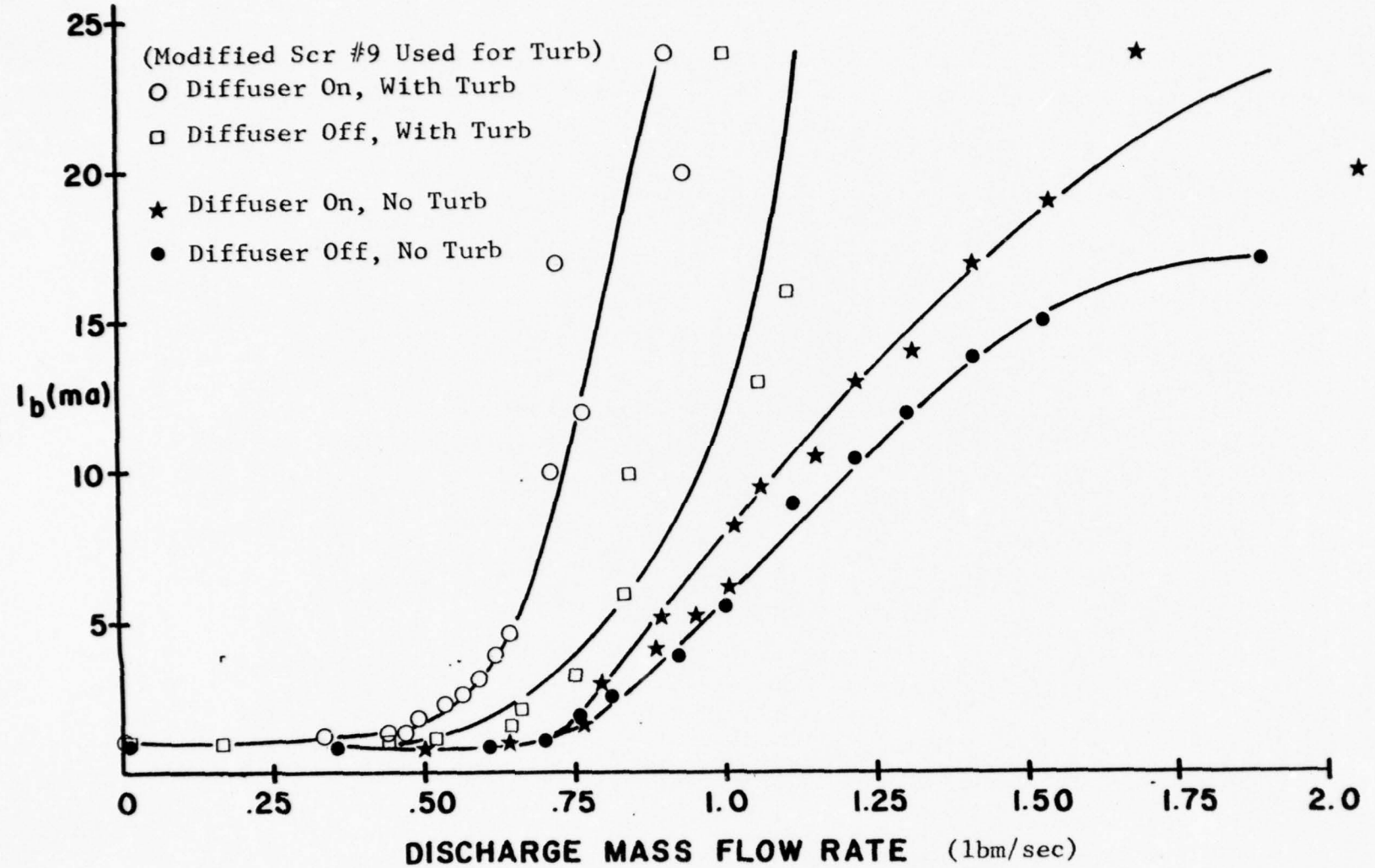


Figure 31. Breakdown Current vs. Discharge Mass Flow Rate for Various Configurations.

APPENDIX A

VARIABLE VOLTAGE RATE TESTS

As stated in the Introduction, this series of tests was undertaken in an attempt to determine whether any type of resonance condition might exist between the rates of voltage increase used and any of the dynamics of the discharge or gas parameters. The fact that the characteristic times for current pulsing, rates of voltage increase and turbulence all overlap in the ranges tested was the primary motivating factor.

The breakdown voltage was found to decrease in a linear fashion with increasing voltage rate (γ) in the ordinary and cross-flow modes (Fig. A-1). At higher velocities in the cross-flow mode, the breakdown voltage increased at the very low values of γ as would be expected from the space-charge-convection model. The slope of the curves remains basically unchanged, however.

In the ordinary flow mode, the effect of the flow definitely increased the slope of the V_b curve, but V_b still decreased linearly with increasing voltage rate.

Under no-flow conditions, using the Townsend type of formula for the relation between current and voltage, it

can be shown that the slope of these V_b vs. γ characteristics should be negative. Assume V_b is a linear function of γ, and

$$V_b(\gamma) = V_{bo} + A\gamma$$

where the 'o' indicates the value at $\gamma \doteq 0$. The Townsend current equation for breakdown is

$$I_b = CV_b(V_b - V_c)$$

and breakdown power is $P_b = I_b V_b$.

$$P_b = CV_b^2(V_b - V_c) = C(V_{bo} + A\ )^3 - C(V_{bo} + A\ )^2 V_c$$

and

$$dP_b/d\ = 3C(V_{bo} + A\ )^2 A - 2C(V_{bo} + A\ )AV_c$$

Now, assuming P_b has a maximum or minimum, letting the above = 0:

$$_{max/min} = (2V_c/3 - V_{bo})/A$$

Since is always positive and V_{bo} $2V_c/3$, then A, the slope of the V_b vs. curve, must be negative as observed.

The reason for this decrease in V_b and I_b is not known and was not pursued due to the uninteresting trends observed.

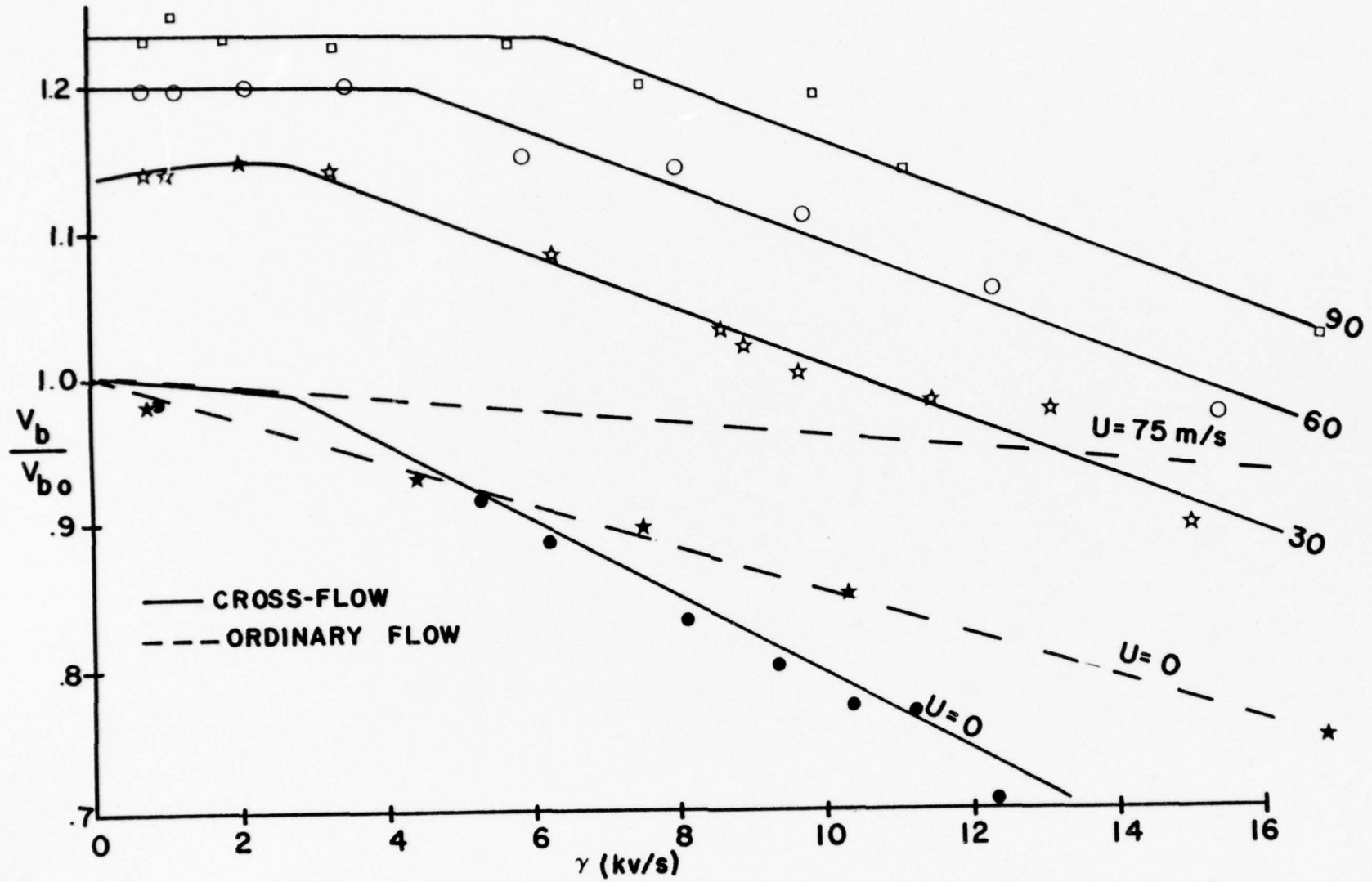


Figure A-1. Variable Rate of Voltage Increase Effect on Breakdown Voltage for Cross and Ordinary Flow Modes.

APPENDIX B

NO-FLOW EMPIRICAL GAP LENGTH/DENSITY OPTIMIZATION AND COMPARISON WITH OBSERVED DATA

Prior to commencement of the testing phase of this work, data was gathered from a number of sources on the breakdown properties of a point-to-plane gap. Empirical equations for $V_b(d, \ )$ and $I_b(d, \ )$ were developed and used in a computer optimization study for this electrode configuration.

The results of this study indicated that, under no-flow conditions, maximum power/cm input could be obtained at $d \doteq 4$ cm and a density ratio of $0.65 \doteq (\ / \ _o)$. This corresponds to a pressure of $\doteq$ 420 torr (Fig. B-1). Figures B-2 & B-3 show the computer generated V_b and I_b characteristics plotted against density ratio. These figures indicate that the 4 cm gap was best at atmospheric pressure too, while data from the present experiments yielded an optimum gap of $\doteq$ 1.6 cm under no-flow conditions at atmospheric pressure (Fig. B-4) for a multiple pin electrode.

The equations used in the optimization study are listed below for reference:

Breakdown Voltage:

$$V_b(\ ,d) = 51(\ / \ _o)^{1.16}(1.8- \ / \ _o)(1-\exp^{T}) + B$$

where

$$T = d^{1.5}/3$$

$$B = 20(d/d_o - 1)(\quad/\quad)^{.65}(1 - \quad/\quad)$$

$$d_o = 4 \text{ cm}$$

Breakdown Current:

$$I_b(\quad, d, V_b) = .09C((\quad/\quad)^{E}V_b^2 - A)$$

$$A = 590(d/d_o - 1)(\quad/\quad - .04)^{.62}(1.2 - \quad/\quad)$$

$$E = 1.05 + (\quad/\quad - .05)^{.33}$$

$$C = 1 \quad \text{for } d \quad 4 \text{ cm}$$

$$C = .11d^{1.6} \quad \text{for } d \quad 4 \text{ cm}$$

A series of tests in the ordinary flow mode was conducted using the turbulence screen number "9" (Fig. 2) of Reference (6) at various velocities and gap lengths in an effort to determine the optimum gap length at atmospheric pressure in the present apparatus. Figures B-5 through B-8 show the results of these tests.

In Figure B-5 the typical V_b vs. velocity trend is evident, showing an initial decrease of V_b and a later increase, except for the short gap-high current case of the 1.6 cm gap which was explained earlier.

Figure B-6 is interesting in that it shows I_b reaching a maximum value of $\doteq$ 17 ma for the three best gaps. This

may be due to the fact that, with no boundary slots as in later tests, the blockage of this screen is ≐ 60%, and maximum velocity is limited to ≐ 120 m/sec through the discharge section. This may result in the section becoming thermally unstable due to inefficient heat removal.

The maximum specific power is shown in Figure B-7. Here it can be seen that the short gap permits highest specific power. This would be expected, since the shorter the gap, the lower the maximum temperature rise in the gas at a given velocity (Ref. 5).

Figure B-8 shows the breakdown current variation with gap length for various constant velocity profiles from the data of the previous figures. It is interesting that at high velocity and high turbulence, the 4 cm gap current increases faster than at the other gap lengths.

It must also be noted that it was later discovered that the power supply used in these tests was limited to 18-19 ma by internal problems, so part of the apparent 17 ma limit in the discharge illustrated in Figure B-6 may be attributable to a power supply limitation rather than a discharge stability limit.

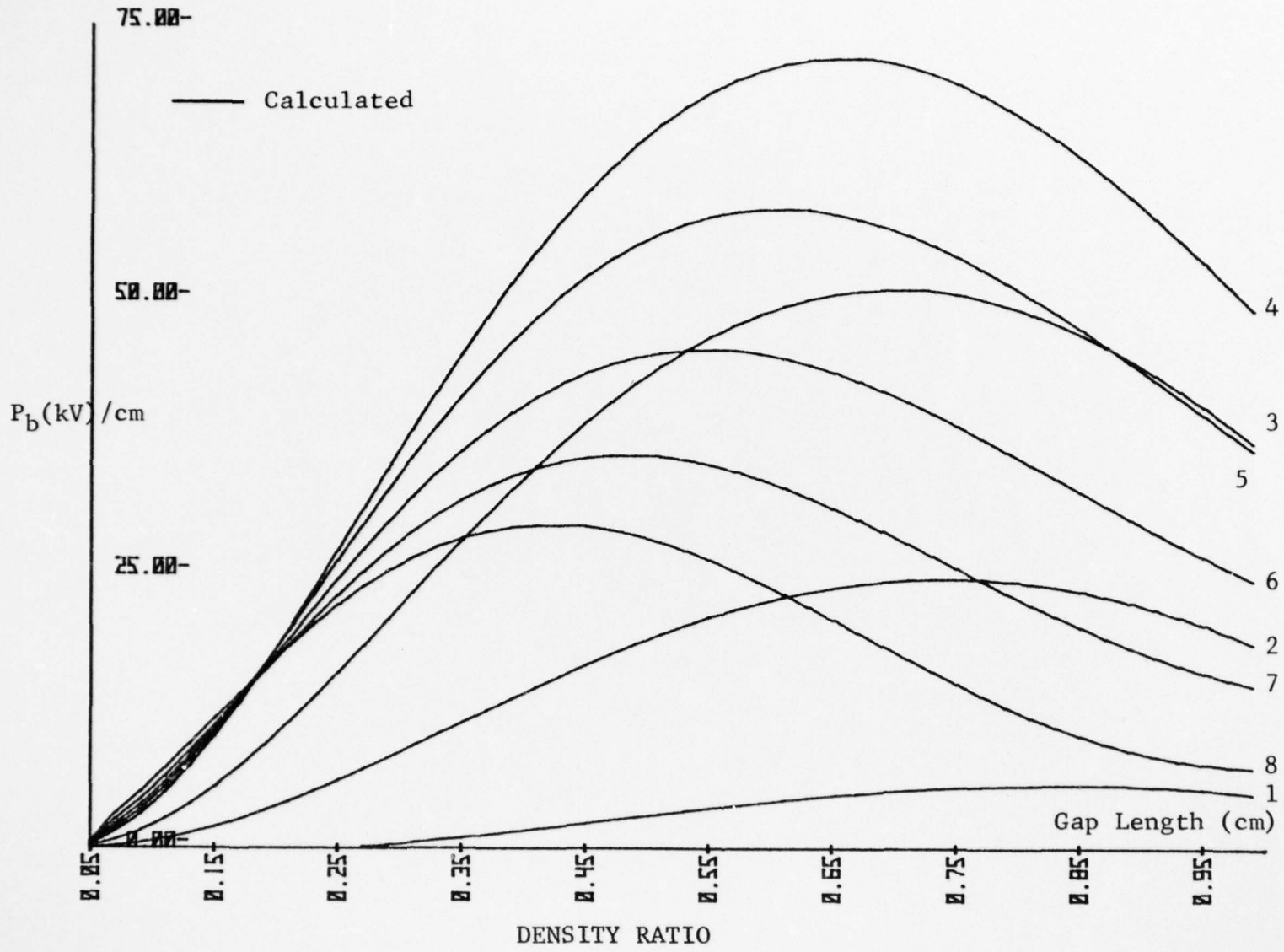


Figure B-1. Breakdown Power/cm vs. Density Ratio for Single Point-to-Plane

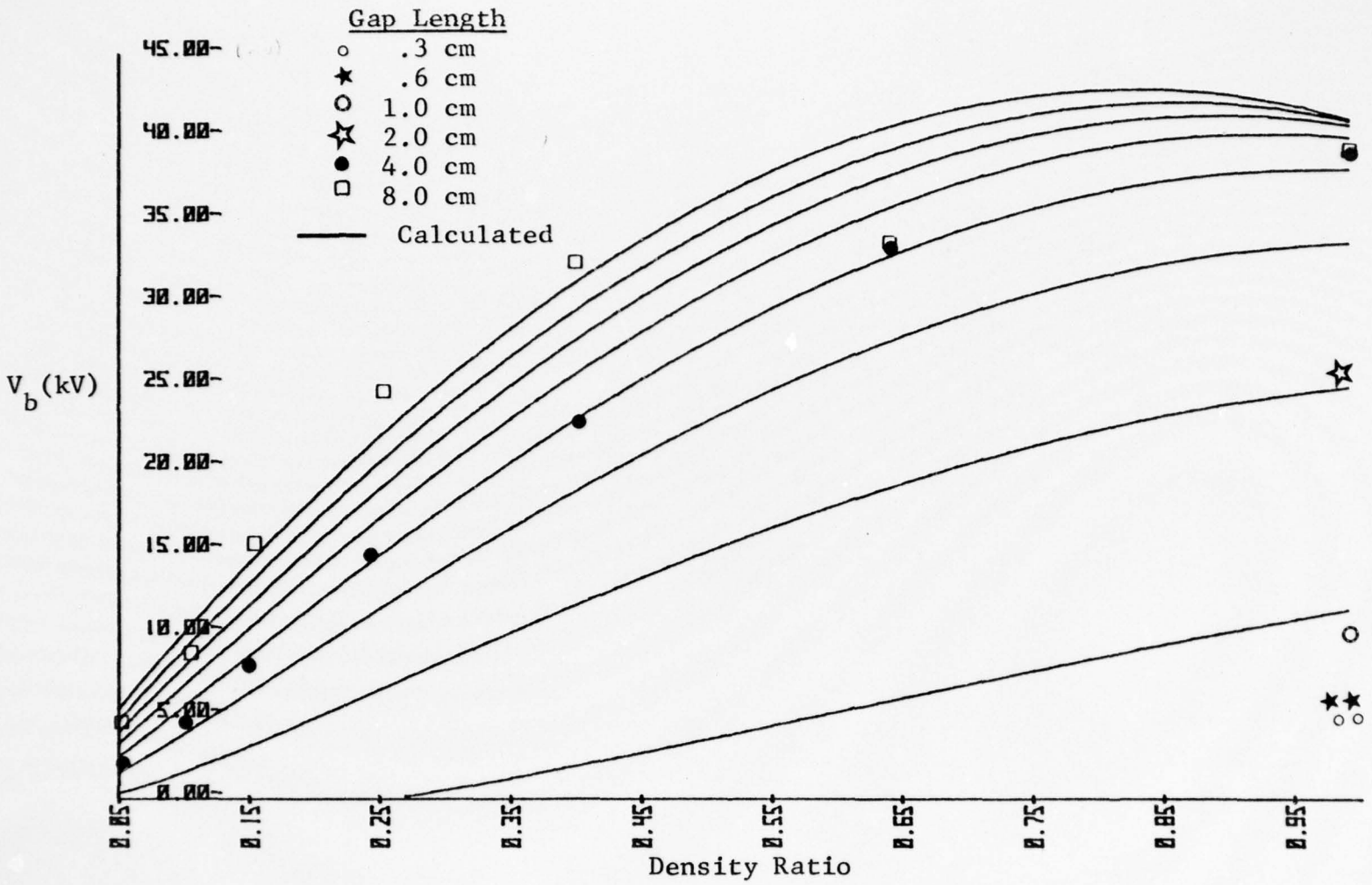


Figure B-2. Breakdown Voltage vs. Density Ratio for Single Point-Plane

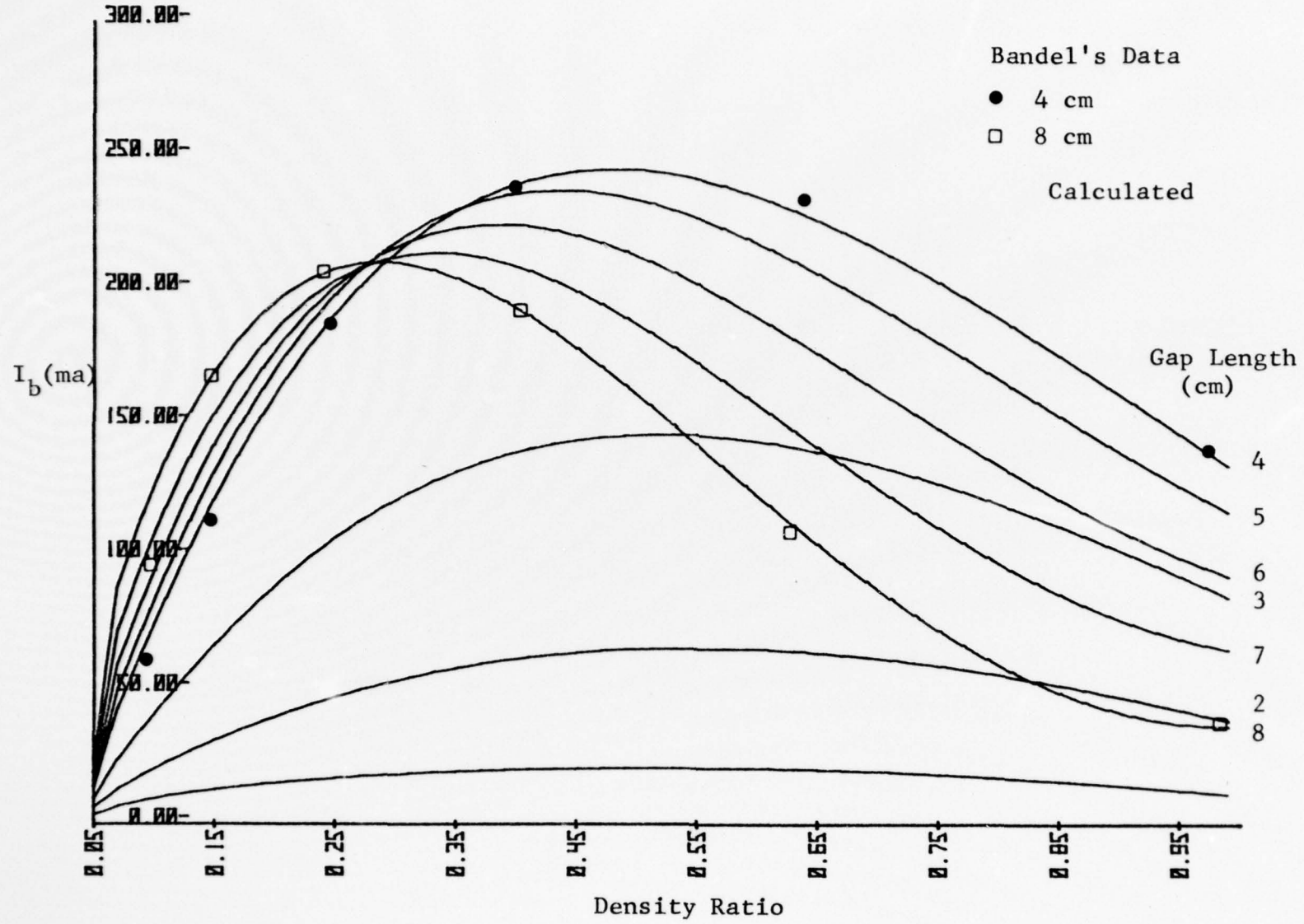


Figure B-3. Breakdown Current vs. Density Ratio for Single Point-Plane.

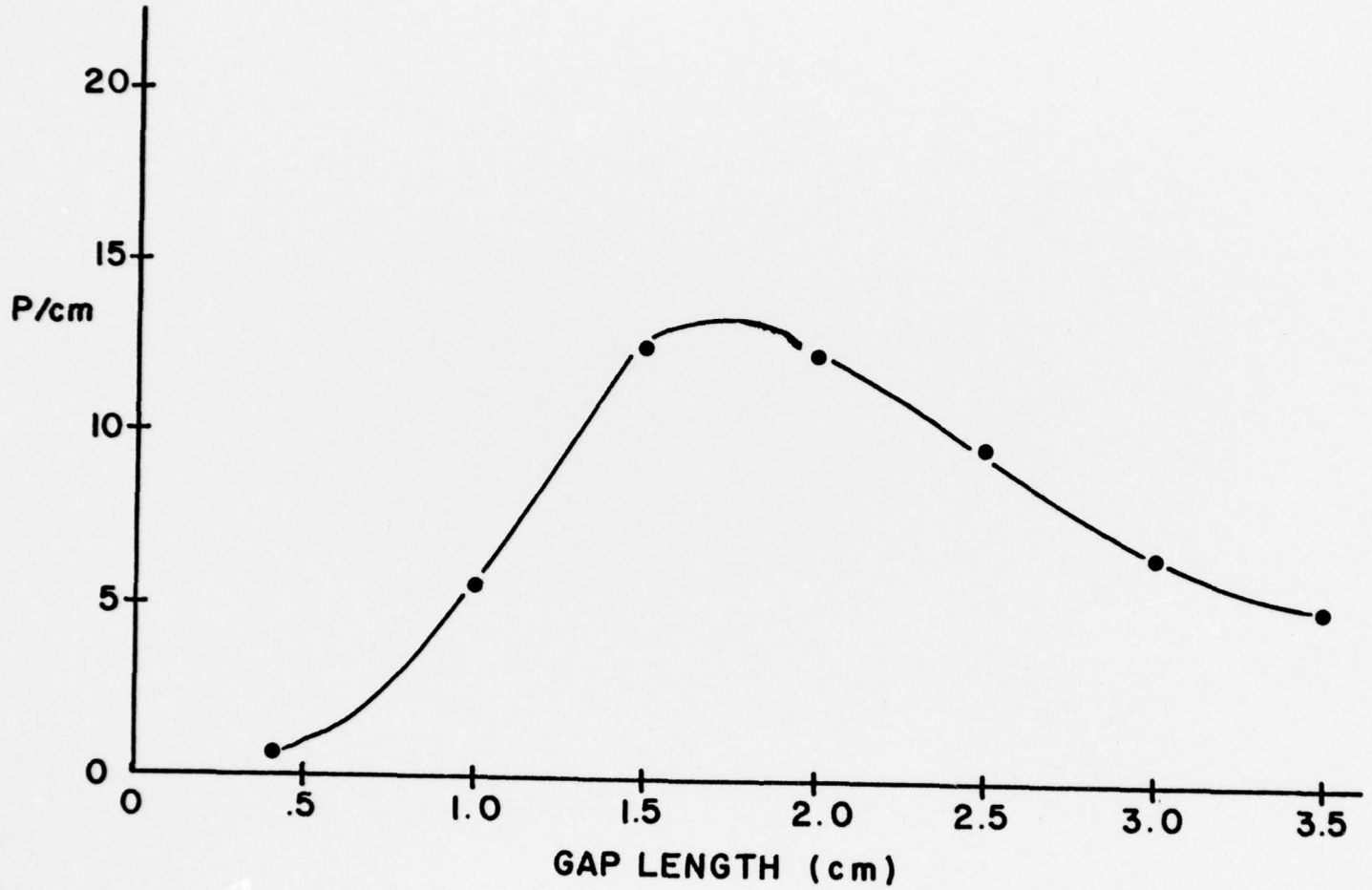


Figure B-4. Breakdown Power/cm vs. Gap Length (No Flow) for Multi-pin to Plane

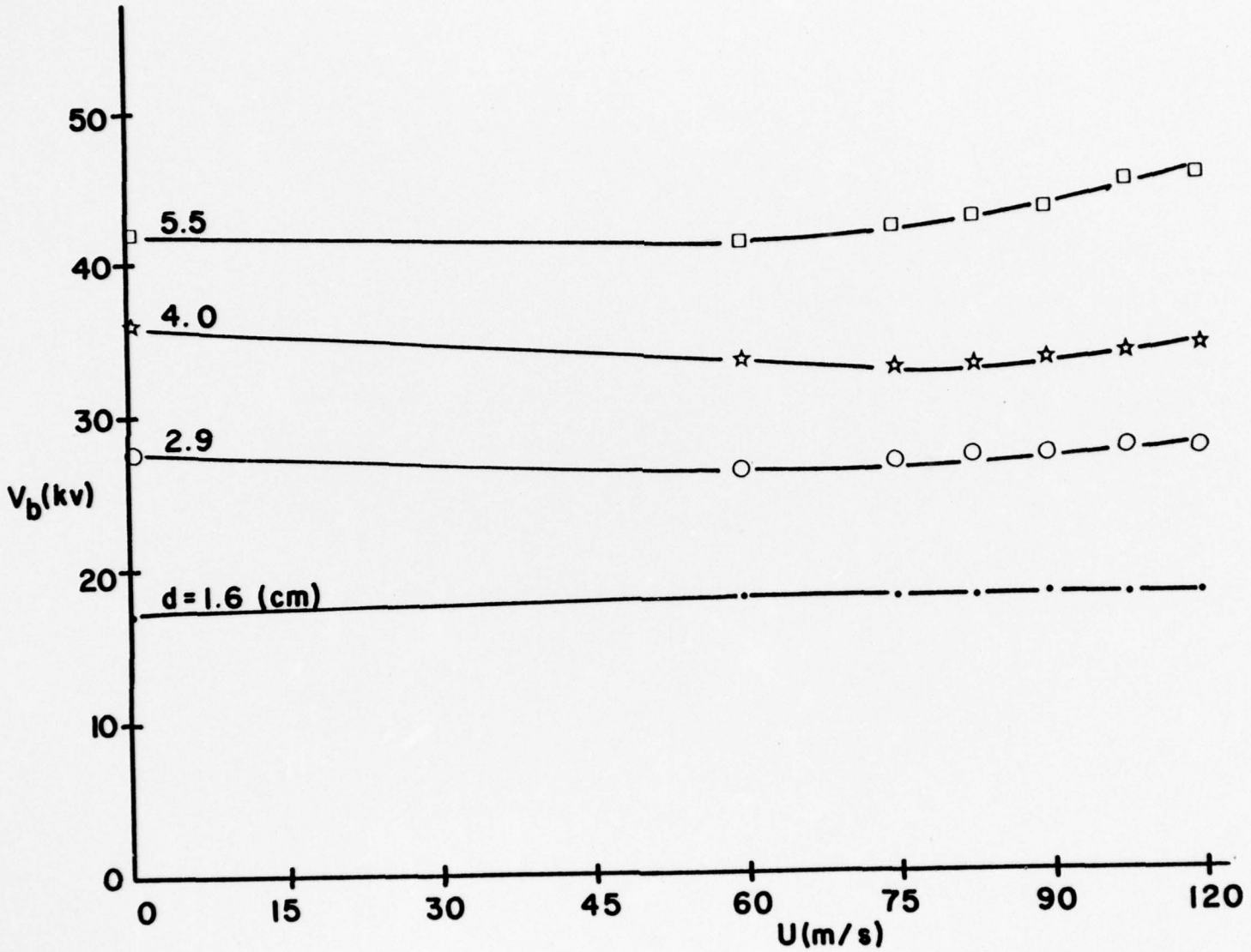


Figure B-5. Breakdown Voltage vs. Velocity for Multi-Pin Configuration with Turbulence Screen #9. (Various Gaps)

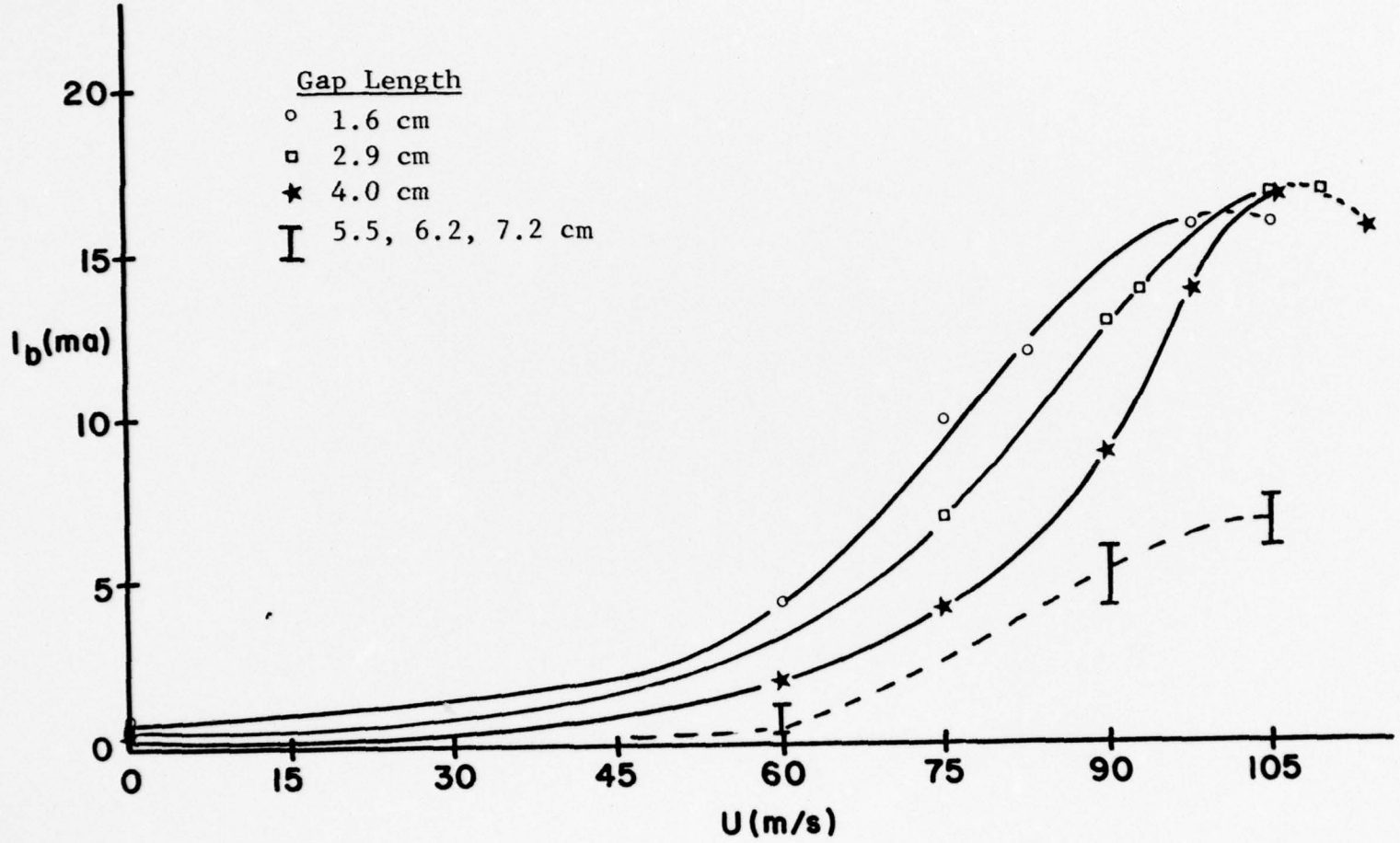


Figure B-6. Breakdown Current vs. Velocity for Multi-Pin Configuration with Turbulence Screen #9

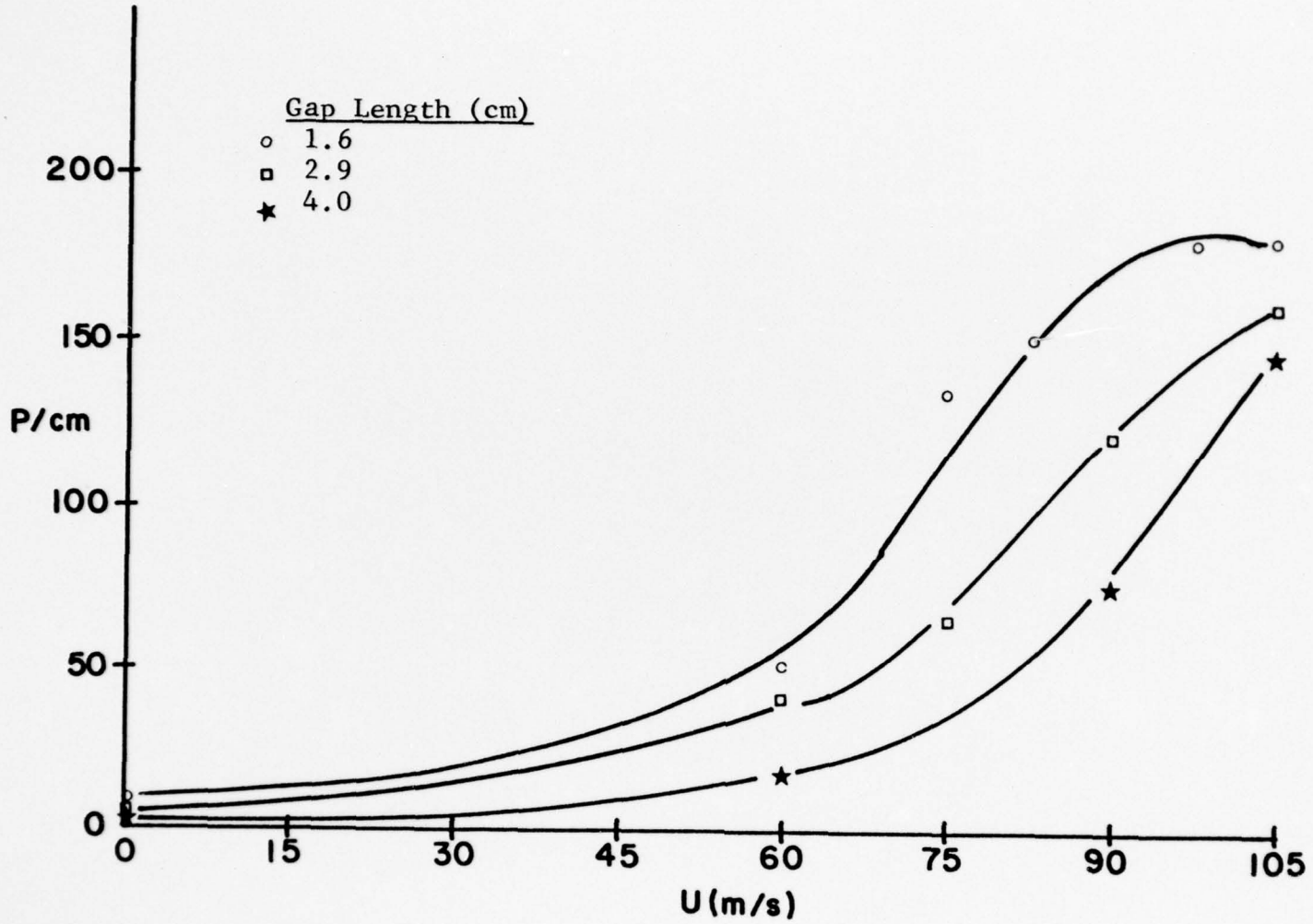


Figure B-7. Breakdown Power/cm vs. Velocity for Multi-Pin Configuration with Turbulence Screen #9

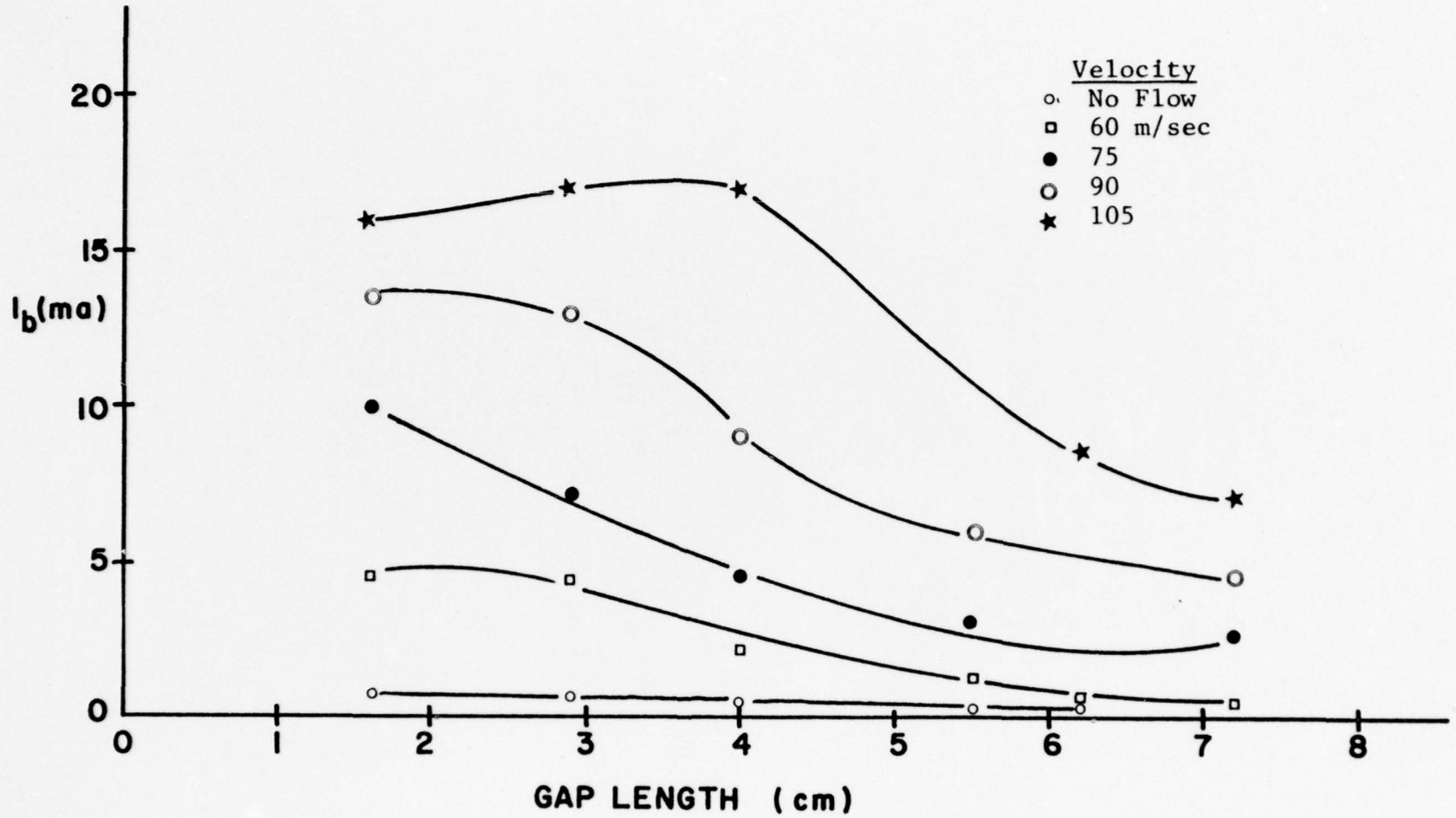


Figure B-8. Breakdown Current vs. Gap Length for Multi-Pin Configuration with Turbulence Screen #9

BIBLIOGRAPHY

1. Reilly, James P., "High Power Electric Discharge Lasers (EDL's)," American Institute of Aeronautics and Astronautics, p. 50-60, March 1975.

2. Nelson, Robert E., Electric Discharge Stabilization by a Highly Turbulent Flow, MS Thesis, U.S. Naval Postgraduate School, June 1973.

3. Post, Howard A., Sub-Ambient Controlled Turbulence Effects on Discharge Stabilization for Laser Applications, MS Thesis, U.S. Naval Postgraduate School, September 1976.

4. Nasser, Essam, Fundamentals of Gaseous Ionization and Plasma Electronics, p. 309, Wiley, 1971.

5. Shwartz, Josef and Wasserstrom E., The Role of Gas Flow and Turbulence in Electric Discharge Lasers, Israel Journal of Technology, v. 13, p. 122-133, 21-22 May 1975.

6. Aunchman, L. J., Controlled Turbulence as a Design Criterion for Electric Discharge Convection Lasers, MS Thesis, U.S. Naval Postgraduate School, March 1974.

7. von Engle, A., Ionized Gases, Second Edition, pp. 16-21, 202, Oxford, 1965.

8. Cobine, J. D., Gaseous Conductors, Theory and Engineering Applications, p. 190, McGraw-Hill, 1941.

9. Pollock, H. C. and Cooper, F. S., "The Effect of Pressure on the Positive Point-to-Plane Discharge in N_2, O_2, CO_2, SO_2, SF_6, CCl_2F_2, A, HE, and H2," Physical Review, v. 56, p. 170-175, 15 July 1939.

10. Meek, J. M. and Craggs, J. D., Electrical Breakdown of Gases, p. 149-150, Oxford, 1953.

11. Werner, F. D., "The Corona Anemometer and its Application to Study of the Effect of Stilling Chamber Turbulence on Test Section Turbulence in a Wind Tunnel at Mach Number Three," Ph.D. Thesis, University of Minnesota, 1955.

12. Rees, J. A., Electrical Breakdown in Gases, p. 18-26, Wiley, 1973.

13. Brown, Sanborn C., Introduction to Electrical Discharges in Gases, p. 136-148, Wiley, 1966.

14. Nygaard, Kaare J., "'Electric Wind' Gas Discharge Anemometer," The Review of Scientific Instruments, v. 36, no. 9, p. 1323, September 1965.

15. Werner, F. D., "An Investigation of the Possible Use of the Glow Discharge as a Means for Measuring Air Flow Characteristics," The Review of Scientific Instruments, v. 21, no. 1, p. 67, January 1950.

16. Biblarz, O. and Nelson, R. E., "Turbulence Effects on an Ambient Pressure Discharge," Journal of Applied Physics, v. 45, no. 2, p. 636, February 1974.

17. Townsend, J. S., Electricity in Gases, p. 389, Oxford, 1915.

18. Loeb, L. B., Electrical Coronas, p. 110, University of California Press, 1965.

19. Haas, Rober A., "Plasma Stability of Electric Discharges in Molecular Gases," Physical Review A, v. 8, no. 2, p. 1017-1043, August 1973.

20. Jacob, J. H. and Mani, S. A., "Thermal Instability in High-Power Laser Discharges," Applied Physics Letters, v. 26, no. 2, p. 53-55, 15 January 1975.

21. Schlicting, Hermann, Boundary-Layer Theory, p. 525-530, McGraw-Hill, 1968.

22. Zauderer, B. and Tate, E., "Investigation of High Power MHD Gas Lasers," Final Report AD-A013583, August 1975.

INITIAL DISTRIBUTION LIST

		No. Copies
1.	Defense Documentation Center Cameron Station Alexandria, Virginia 22314	2
2.	Library, Code 0212 Naval Postgraduate School Monterey, California 93940	2
3.	Department Chairman, Code 67 Department of Aeronautics Naval Postgraduate School Monterey, California 93940	1
4.	Asso. Professor Oscar Biblarz, Code 67Bi Department of Aeronautics Naval Postgraduate School Monterey, California 93940	2
5.	LCDR Jon L. Barto, USN 960 C Avenue Coronado, CA 92118	1
6.	Dr. D. G. Samaras Air Force Office of Scientific Research (AFSC) Bolling AFB Washington, D. C. 20332	1
7.	Dr. J. Shwartz, RI-1016 TRW One Space Park Redondo Beach, CA 90278	1
8.	Professor G. C. Shih Department of Mechanical Engineering The University of Alabama at Huntsville P. O. Box 1247 Huntsville, Alabama 35807	1

9. Dr. H. H. Legner — 1
AVCO-Everett Res. Lab
2385 Revere Beach Pkwy
Everett, MA 02149

10. Dr. Alan Garscadden — 1
Plasma Physics Research Lab
ARL(LU) Blg 450
Wright-Patterson AFB, OH 45433

11. LT Howard A. Post, USN — 1
Navy Space Systems Activity
Air Force Unit Post Office
Los Angeles, CA 90045